

UNCLASSIFIED

| |
|--|
| |
| |
| |
| AD NUMBER |
| AD908907 |
| NEW LIMITATION CHANGE |
| TO Approved for public release, distribution unlimited |
| FROM Distribution authorized to U.S. Gov't. agencies only; Test and Evaluation; JAN 1973. Other requests shall be referred to Air Force Armament Laboratory, DLDL, Eglin AFB, FL 32542. |
| AUTHORITY |
| AFATL ltr, 10 Oct 1975 |

THIS PAGE IS UNCLASSIFIED

THIS REPORT HAS BEEN DELIMITED
AND CLEARED FOR PUBLIC RELEASE
UNDER DOD DIRECTIVE 5200.20 AND
NO RESTRICTIONS ARE IMPOSED UPON
ITS USE AND DISCLOSURE.

DISTRIBUTION STATEMENT A

APPROVED FOR PUBLIC RELEASE;
DISTRIBUTION UNLIMITED.

L

AFATL-TR-73-15

AD908907

MONTE CARLO ANALYSIS OF S-CURVE
AND ROLL-THROUGH-ZERO BOMBLET
DISPERSION CHARACTERISTICS

ALPHA RESEARCH, INC.

Copy available to DDC does not
permit fully legible reproduction

TECHNICAL REPORT AFATL-TR-73-15

JANUARY 1973

DDC
RECEIVED
APR 6 1973
B

Distribution limited to U. S. Government agencies only;
this report documents test and evaluation; distribution
limitation applied January 1973 . Other requests for
this document must be referred to the Air Force Armament
Laboratory (DLDL) , Eglin Air Force Base, Florida 32542.

AIR FORCE ARMAMENT LABORATORY

AIR FORCE SYSTEMS COMMAND • UNITED STATES AIR FORCE

EGLIN AIR FORCE BASE, FLORIDA

**Best
Available
Copy**

Monte Carlo Analysis Of S-Curve And Roll-Through-Zero Bomblet Dispersion Characteristics

James E. Brunk

Distribution limited to U. S. Government agencies only;
this report documents test and evaluation; distribution
limitation applied January 1975. Other requests for
this document must be referred to the Air Force Armament
Laboratory (PL06), Eglin Air Force Base, Florida 32542.

Copy available to DDC does not
permit fully legible reproduction

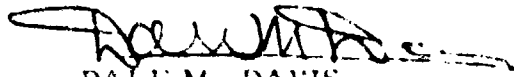
FOREWORD

This final report documents work accomplished during the period 4 February 1971 through 15 November 1972 by Alpha Research, Inc., Santa Barbara, California, under Contract No. F08635-71-C-0089 with the Air Force Armament Laboratory, Eglin Air Force Base, Florida. Monitoring the program for the Armament Laboratory were Messrs. M. Bouffard and 2nd Lt. Paul Mayer (DLDL). The principal investigator for the contractor was Mr. James E. Brunk.

Digital computer service, flight-test support service, and model design and fabrication service in support of this effort were provided by the Air Force Armament Laboratory and Armament Development and Test Center, Eglin Air Force Base, Florida.

Additional wind tunnel test support was provided by the 4T Projects Branch, PWT, Arnold Engineering Development Center, Arnold Air Force Station, Tennessee.

This technical report has been reviewed and is approved.



DALE M. DAVIS
Director, Guns & Rockets Division

ABSTRACT

The flight dynamics and dispersion characteristics of candidate S-Curve and roll-through-zero bomblets are evaluated by use of the Monte Carlo method. Detailed analyses of bomblet-cluster breakup and bomblet configurational and aerodynamic asymmetries are used to establish the statistical input data required for the Monte Carlo analyses. Improved aerodynamic data packages for both the S-Curve and roll-through-zero bomblets are provided, and results of additional wind tunnel tests are discussed. Monte Carlo simulations show that for realistic flight environments, both the S-Curve and roll-through-zero bomblets can achieve large and uniform impact patterns. For a representative dispenser HOB of 2000 feet, opening velocity of 900 feet/second, and 45 degrees flight path angle, impact pattern widths of 800 and 600 feet are computed for the S-Curve and roll-through-zero type bomblets, respectively. The effects of transonic and supersonic delivery, large static mass unbalance, nose-roughness asymmetry, and intentional fin cant on the S-Curve bomblet flight characteristics and dispersion are investigated in detail. Flight test dispersion data for the S-Curve bomblet, as obtained from air-gun launched models, is compared with results from analytical simulations. A dynamic wind tunnel model support system, designed for testing the S-Curve bomblet, is described.

Distribution limited to U. S. Government agencies only; this report documents test and evaluation; distribution limitation applied January 1973. Other requests for this document must be referred to the Air Force Armament Laboratory (DLDL), Eglin Air Force Base, Florida 32542.

TABLE OF CONTENTS

| Section | Title | Page |
|--------------|--|------|
| I | INTRODUCTION | 1 |
| II | S-CURVE BOMBLET INVESTIGATIONS | 3 |
| | A. Configurations | 3 |
| | B. Aerodynamic Characteristics - Basic S-Curve Configurations | 3 |
| | C. Predicted Flight Dynamics of Basic Configurations | 17 |
| | D. Dispersion Prediction - General Considerations | 24 |
| | E. Monte Carlo Impact Patterns | 26 |
| | F. Special Studies - High Drag and Dual Mode Bomblets | 38 |
| | G. Analysis of Alternate S-Curve Configurations | 41 |
| | H. Air-Gun Launched Model Free-Flight Tests | 43 |
| III | ROLL-THROUGH-ZERO BOMBLET INVESTIGATIONS | 50 |
| | A. Configurations | 50 |
| | B. Aerodynamic Characteristics | 51 |
| | C. Predicted Flight Dynamics | 55 |
| | D. Dispersion Prediction | 59 |
| IV | DEVELOPMENT OF MONTE CARLO METHOD FOR DISPERSION PREDICTION | 63 |
| | A. General | 63 |
| | B. Monte Carlo Trajectory Program | 63 |
| | C. Statistical Analysis of Cluster Break-Up | 67 |
| | D. Statistical Analysis of Configurational Asymmetries | 71 |
| V. | DEVELOPMENT OF DYNAMIC WIND TUNNEL MODEL SUPPORT SYSTEM | 76 |
| | A. System Description | 76 |
| | B. System Operation | 76 |
| | C. System Utilization | 80 |
| Appendix I. | THEORETICAL CONING MOTION ANALYSIS WITH ROLL DEPENDENT SIDE MOMENT | 85 |
| Appendix II. | THEORETICAL PREDICTION OF CLUSTER SPREAD VELOCITY | 88 |
| References | | 93 |

LIST OF FIGURES

| Figure | Title | Page |
|--------|---|------|
| 1 | Basic S-Curve Bomblet Configurations | 4 |
| 2 | Design Concept for S-Curve Bomblet with Large-Span Fins | 5 |
| 3 | Design Concept for S-Curve Bomblet with Extensible Fin Assembly | 6 |
| 4 | Low-Fineness Ratio S-Curve Bomblet Configurations | 7 |
| 5 | Trim Characteristics of Basic S-Curve Bomblet Configurations | 9 |
| 6 | Magnus Force and Moment Characteristics of Basic S-Curve Bomblet with Cylindrical Afterbody | 10 |
| 7 | Spin Characteristics of Basic S-Curve Configuration - Roll Torque Due to Cant | 12 |
| 8 | Induced Aerodynamic Moment Characteristics of Basic S-Curve Bomblet Configuration | 14 |
| 9 | Effect of Nose-Roughness on the Induced Aerodynamic Side Moment | 15 |
| 10 | Effect of S-Curve Bomblet Configuration on Normal Force Center of Pressure | 16 |
| 11 | Effect of Side Moment on Roll Lock-In | 21 |
| 12 | Definition of Angles of Axes Used in Describing Bomblet Roll Dynamics | 22 |
| 13 | Effect of CG Lateral Offset on Radial Dispersion | 23 |
| 14 | Effect of Intentional Fin Cant on the Motion of an S-Curve Bomblet with Lateral CG Offset | 25 |
| 15 | Monte Carlo Impact Pattern Prediction for S-Curve Bomblet - High-Subsonic Event Condition | 28 |
| 16 | Probability Distributions for S-Curve Bomblet Impact Dispersion Pattern | 29 |
| 17 | Monte Carlo Impact Pattern Prediction for S-Curve Bomblet - Transonic Event Condition | 31 |
| 18 | Monte Carlo Impact Pattern Prediction for S-Curve Bomblet - Supersonic Event Condition | 32 |
| 19 | Variation of Impact Dispersion with CG Lateral Offset | 34 |

LIST OF FIGURES (Continued)

| Figure | Title | Page |
|--------|--|------|
| 20 | Effect of S-Curve Bomblet Trim Angle of Attack on Monte Carlo Impact Pattern for Standard Subsonic Event Condition | 37 |
| 21 | Trajectory Comparisons - Basic and High Drag S-Curve Bomblet Configurations - Standard Subsonic Event Condition | 39 |
| 22 | Trajectory Comparison - Basic and Dual Mode S-Curve Bomblet Configurations - Standard Subsonic Event Condition | 40 |
| 23 | Normal Force Characteristics of Candidate S-Curve Bomblet Configurations | 42 |
| 24 | Flight Test and Simulated Impact Patterns for Air-Gun Launched 3-Inch Diameter Ballistic Models | 45 |
| 25 | Flight Test and Simulated Impact Patterns for Air-Gun Launched 3-Inch Diameter Standard S-Curve Bomblet Models (Cylindrical Afterbody) | 46 |
| 26 | Flight Test Impact Patterns for Air-Gun Launched 1.5-Inch Diameter S-Curve Bomblet Models | 48 |
| 27 | Basic Roll-Through-Zero Bomblet | 52 |
| 28 | Roll Reversing Tab | 53 |
| 29 | Aerodynamic Characteristics of Roll-Through-Zero Bomblet as Function of the Aerodynamic Roll Angle | 54 |
| 30 | Harmonic Fit to Aerodynamic Induced Roll Moment - Basic Roll-Through-Zero Bomblet | 56 |
| 31 | Motion Histories for Basic Roll-Through-Zero Bomblet | 58 |
| 32 | Monte Carlo Impact Pattern Prediction for Basic Roll-Through-Zero Bomblet - High-Subsonic Event Condition | 61 |
| 33 | Schematic of Bomblet Cluster Break-Up and Definition of Initial Motion Perturbations | 65 |
| 34 | Experimental Cumulative Frequency Distribution for Cluster Break-Out Time | 68 |
| 35 | Experimental Data for Bomblet-Cluster Deceleration | 69 |
| 36 | Experimental Data for Bomblet-Cluster Spread Velocity | 72 |
| 37 | Dynamic-Wind-Tunnel-Model Support System - Design of Rotating Sting | 77 |

LIST OF FIGURES (Concluded)

| Figure | Title | Page |
|--------|--|------|
| 38 | Dynamic-Wind-Tunnel-Model Support System - Design of Model-Sting Attachment | 78 |
| 39 | Dynamic Wind Tunnel Model Support System | 79 |
| 40 | Schematic of Dynamic-Wind-Tunnel-Model Support System - Axes and Angular Rate Definitions | 82 |
| I-1 | Variation of Side Moment Coefficient with ϕ for Basic S-Curve Bomblet Configurations | 86 |
| II-1 | Lateral Force Parameter for Bomblet Separating from Cluster | 91 |

LIST OF TABLES

| Table | Page | |
|-------|--|----|
| I | Aerodynamic Coefficient Summary for Basic S-Curve Configuration $B_S N_{S2} A_{S1} F_{S2}$ | 18 |
| II | Aerodynamic Coefficient Summary for Basic S-Curve Configuration $B_S N_{S1} A_{S2} F_{S3}$ | 19 |
| III | Physical Characteristics Data for Standard Size S-Curve Bomblet | 26 |
| IV | Comparison of Impact Dispersion Data for Subsonic, Transonic, and Supersonic Event Conditions | 33 |
| V | Physical Characteristics Data for S-Curve Free-Flight Test Models | 44 |
| VI | Summary of Impact Dispersion Data for Air-Gun- Launched Free-Flight Models | 49 |
| VII | Aerodynamic Coefficient Summary for Basic Roll- Through-Zero Bomblet Configuration | 57 |
| VIII | Comparison of Impact Dispersion Data for Roll-Through- Zero and S-Curve Bomblets - Subsonic Event Condition | 60 |
| IX | Comparison of Theoretical and Monte Carlo Dispersion Predictions for Roll-Through-Zero Bomblet | 62 |

NOMENCLATURE

| | |
|---------------------------|---|
| C_D | Drag coefficient |
| C_L | Lift coefficient |
| C_{ℓ} | Roll torque Coefficient |
| C_{ℓ_0} | Roll torque at zero roll rate |
| C_{ℓ_p} | Roll damping coefficient |
| C_{ℓ_δ} | Roll torque coefficient due to cant |
| C_{ℓ_ϕ} | Roll moment coefficient due to aerodynamic roll angle |
| $C_{\ell_{\phi_1, 2, 3}}$ | Roll moment coefficient due to aerodynamic roll angle - first, second, and third harmonics: $C_{\ell}(\phi) = C_{\ell_{\phi_1}} \sin \eta_1 \phi + C_{\ell_{\phi_2}} \sin \eta_2 \phi + C_{\ell_{\phi_3}} \sin \eta_3 \phi$ |
| C_M | Overturning moment coefficient |
| C_{m_q} | Damping derivative (for angle of attack plane); $\partial C_M / \partial (\frac{\dot{q}d}{2V})$ |
| C_{m_0} | Body-fixed pitching moment coefficient due to aerodynamic asymmetry |
| C_{M_δ} | Pitching moment coefficient due to fin deflection and/or lateral misalignment |
| C_{M_ϕ} | Overturning moment coefficient due to aerodynamic roll angle - first harmonic $C_M(\phi) = C_{M_1} \sin \eta_1 \phi$ |
| C_{M_p} | Magnus moment coefficient |
| C_N | Normal force coefficient |
| C_{N_δ} | Normal force coefficient due to fin deflection and/or lateral misalignment |
| C_{n_0} | Body-fixed yawing moment coefficient due to aerodynamic asymmetry |
| C_{n_r} | Damping derivative (Magnus plane); $-C_{SM} / \alpha (\frac{\dot{r}d}{2V})$ |
| C_{N_1} | Normal force coefficient due to aerodynamic roll angle - first harmonic $C_N(\phi) = C_{N_1} \sin \eta_1 \phi$ |
| C_{N_p} | Magnus force coefficient |
| C_{SF_1} | Side force coefficient due to aerodynamic roll angle - first harmonic $C_{SF}(\phi) = C_{SF_1} \sin \eta_1 \phi$ |
| C_{SM} | Side moment coefficient |

NOMENCLATURE (Continued)

| | |
|------------------|---|
| $C_{SM_{1,2,3}}$ | Side moment coefficient due aerodynamic roll angle - first, second, and third harmonics: $C_{SM}(\phi) = C_{SM_1} \sin \eta_1 \phi + C_{SM_2} \sin \eta_2 \phi + C_{SM_3} \sin \eta_3 \phi$ |
| d | Aerodynamic reference length, bomblet diameter |
| F | Force |
| g | Acceleration due to gravity |
| h | Event altitude |
| I | Transverse moment of inertia |
| I_x | Axial moment of inertia |
| I_x' | Nondimensional inertia, $I_x / \rho S d^3$ |
| I_{xy} | Product of inertia |
| m | Mass |
| m' | Nondimensional mass, $m / \rho S d$ |
| m | Number of fin planar pairs |
| n | Number of fins |
| p | Roll rate |
| q | Body-fixed angular rate about y axis |
| \dot{q} | Pitch rate in angle of attack plane |
| r | Body-fixed angular rate about z axis |
| \tilde{r} | Angular rate component for Magnus plane |
| r | Radial displacement of bomblet from dispenser axis of rotation |
| r | Cross-range dispersion at impact |
| R | Range dispersion at impact |
| S | Aerodynamic reference area, $\pi d^2 / 4$ |
| t | Time |
| t_{b_0} | Time at cluster break-out |
| U_∞ | Free-stream velocity |
| V | Velocity |
| V_E | Event velocity |
| V_R | Radial velocity at cluster break-out or cluster spread velocity |
| W | Weight |

NOMENCLATURE (Concluded)

| | |
|----------------------|--|
| Δx | Displacement of c_g along body axis of symmetry |
| Δy | Lateral displacement of c_g (along y axis) |
| x, y, z | Body-fixed axes |
| X, Y, Z | Inertial reference axes |
| $\bar{\alpha}$ | Total angle of attack |
| α_T | Trim angle of attack |
| γ | Flight path angle |
| $\Delta\gamma$ | Angular deflection of flight path |
| γ_E | Flight path angle at dispenser event |
| δ | Fin deflection |
| δ_{CANT} | Cant angle of all fins uniformly deflected |
| δ_{LAT} | Effective deflection of a planar pair of fins |
| ϵ | Lateral misalignment of body and fin assembly |
| ζ, ζ_1 | Roll orientation of aerodynamic surfaces (see Figure 12) |
| $\bar{\zeta}$ | Roll orientation of lateral misalignment (see Figure 12) |
| ω | Frequency parameter for aerodynamic roll angle dependence |
| ξ | Orientation of cross velocity (see Figure 12) |
| ρ | Air density |
| σ | Standard deviation values |
| τ | Roll orientation of body axes (see Figure 12) |
| $\bar{\tau}_R$ | Orientation of radial velocity at cluster break-out |
| θ | Orientation of angle of attack plane at cluster break-out |
| $\bar{\theta}$ | Orientation of angle of attack plane with respect to vertical plane (for theoretical coning motion analysis) |
| $\delta\bar{\theta}$ | Perturbation of $\bar{\theta}$ |
| ϕ | Aerodynamic roll angle (see Figure 12) |
| $\dot{\phi}$ | Orientation of angle of attack plane (see Figure 12) |
| ω | Dispenser roll rate |
| Ω | Rotation rate of model support sting |

SECTION I

INTRODUCTION

One of the most effective means of dispersing a cluster bomb unit is through the use of aerodynamic self-dispersing bomblet munitions. With this approach the energy requirements for dispersal are not only derived from the kinetic and potential energy of the aircraft and dispenser, but more significantly, the dispersal force is applied over the entire bomblet flight period. The advantage of aerodynamic dispersion increases with increasing delivery Mach number.

While self-dispersing magnus-rotor-type bomblets have received considerable attention and utilization in recent years, other types of aerodynamic self-dispersing bomblets have yet to be introduced in quantity. Two new types of self-dispersing bomblets appear particularly promising, namely, the S-Curve type bomblet and the roll-through-zero type bomblet.

The S-Curve bomblet is comprised of an axially symmetric body or body-fin configuration which is designed to provide an unstable restoring moment at small angle of attack and a stable pitching moment slope at a large trim angle of attack. The S-Curve name is derived from the shape of the nonlinear pitching moment curve.

The roll-through-zero bomblet is comprised of a lifting-body configuration equipped with a roll producing device which will cause the bomblet to roll in a direction opposite to its initial direction of roll. The dispersion of this type bomblet is inversely proportional to the magnitude of the roll torque used to reverse the roll.

Both the S-Curve and roll-through-zero bomblets have quasi-ballistic flight characteristics, relatively low drag, and nose-first impact.

Preliminary analytical studies of the flight dynamics and dispersion characteristics of these bomblets were accomplished under Air Force Contract No. F08635-70-C-0012 and the results presented in References 1 and 2. These investigations revealed the general feasibility of both the S-Curve and roll-through-zero type bomblets and provided preliminary estimates of the area coverage.

The remaining problems were (1) to determine if these bomblets could properly function under representative cluster break-up conditions, (2) to determine the performance degradation due to realistic configurational and aerodynamic asymmetries, (3) to determine the actual impact pattern distribution; and (4) to evolve bomblet shapes and candidate configurations adaptable to a wide range of possible warhead and weapon system concepts.

The present effort has encompassed both a wide range of analytical and experimental programs directed toward the answers to these problems. The analytical effort has entailed the development of a comprehensive Monte Carlo trajectory and impact pattern simulation program, based on modifications to the six-degrees-of-freedom (6-DOF) trajectory program (References 3 and 4). Concurrent with the previous and present analytical efforts, several series of wind tunnel tests of S-Curve and roll-through-zero bomblet models were accomplished by the Air Force, using the Arnold Engineering Development Center (AEDC) facilities. These data have been integrated into all of the analytical simulations and are discussed in detail in the body of this report.

To provide additional verification of the S-Curve bomblet performance, a flight test program, using gun-launched models, was initiated and completed during the contractual period. The test plan and model designs were provided by the contractor, while the tests and data acquisition were accomplished by the Air Force Armament Laboratory. A summary of the test results and analyses of these data are provided in this document.

Because the aerodynamic characteristics of bomblet configurations undergoing combined rolling and coning motions at large trim angles of attack are still not well understood, the development of a special dynamic wind tunnel test system was undertaken. The test system was designed by the contractor, fabricated by the Air Force Armament Laboratory, and installed in the Armament Laboratory subsonic wind tunnel. A description of the test system and its operation is provided.

SECTION II.

S-CURVE BOMBLET INVESTIGATIONS

A. CONFIGURATIONS

The present effort has been concerned primarily with two basic S-Curve bomblet configurations as depicted in Figure 1. These two configurations were selected from the results of the original analytical study (Reference 1) as having the best performance characteristics of those models originally evaluated in the transonic wind tunnel tests (Reference 5).

During the course of the present contractual effort some additional configurational modifications to the basic 4-caliber body were investigated in the wind tunnel facilities of AEDC, including two different blunt-nose shapes and fins with increased span. The larger fins (0.14 caliber exposed semi-span) were incorporated as a means of improving the allowable axial cg range.

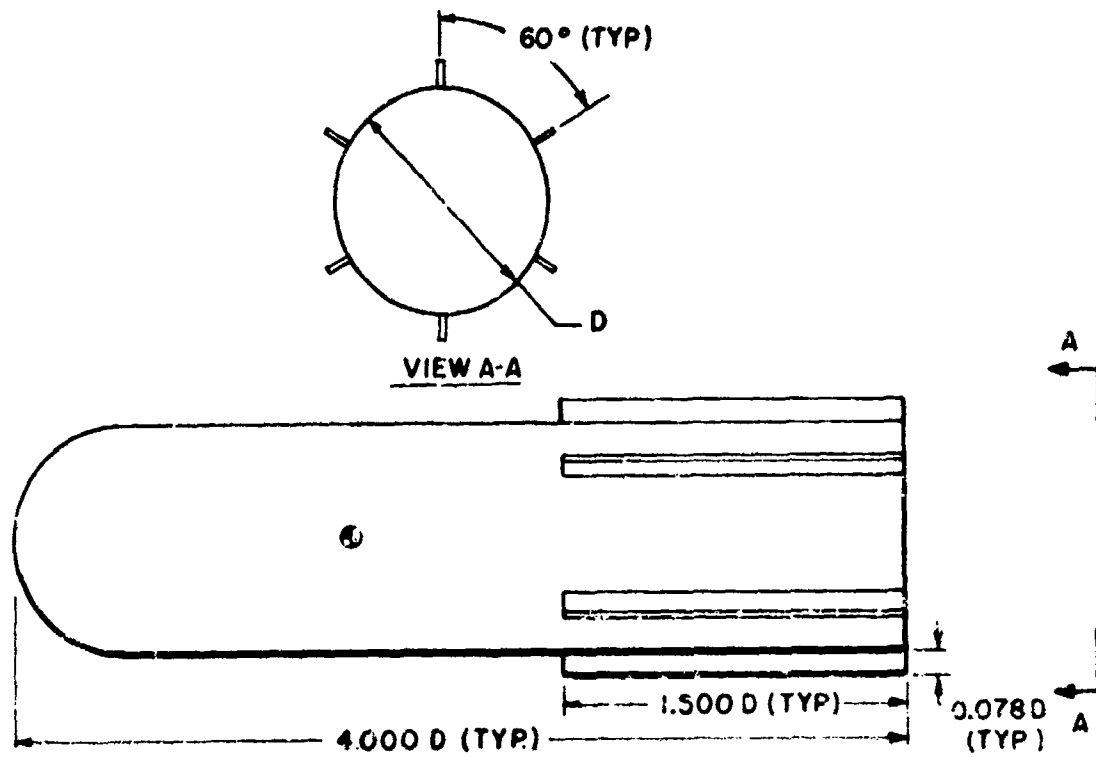
Because increased span fins complicate the bomblet-dispenser packaging, design studies were accomplished to determine a more optimum shape. Figure 2 illustrates a modified afterbody which allows the exposed fin semi-span to be as large as 0.20 body-diameter without loss of packaging efficiency. Design concepts were also devised for rearward extension of the fin assembly as a means of improving the packaging and allowable axial cg range. An extensible fin design is depicted in Figure 3. The configurations shown in Figures 2 and 3 were not wind tunnel tested, but tests of a similar extensible fin concept for an S-Curve version of the BLU-87/B are described in Reference 6.

Low fineness ratio S-Curve configurations were also briefly examined. Figure 4 illustrates two low fineness ratio shapes with S-Curve moment characteristics based on the data of References 7 and 8. The lift, damping, and trim stability gradients of these configurations are poor compared with the basic 4-caliber designs.

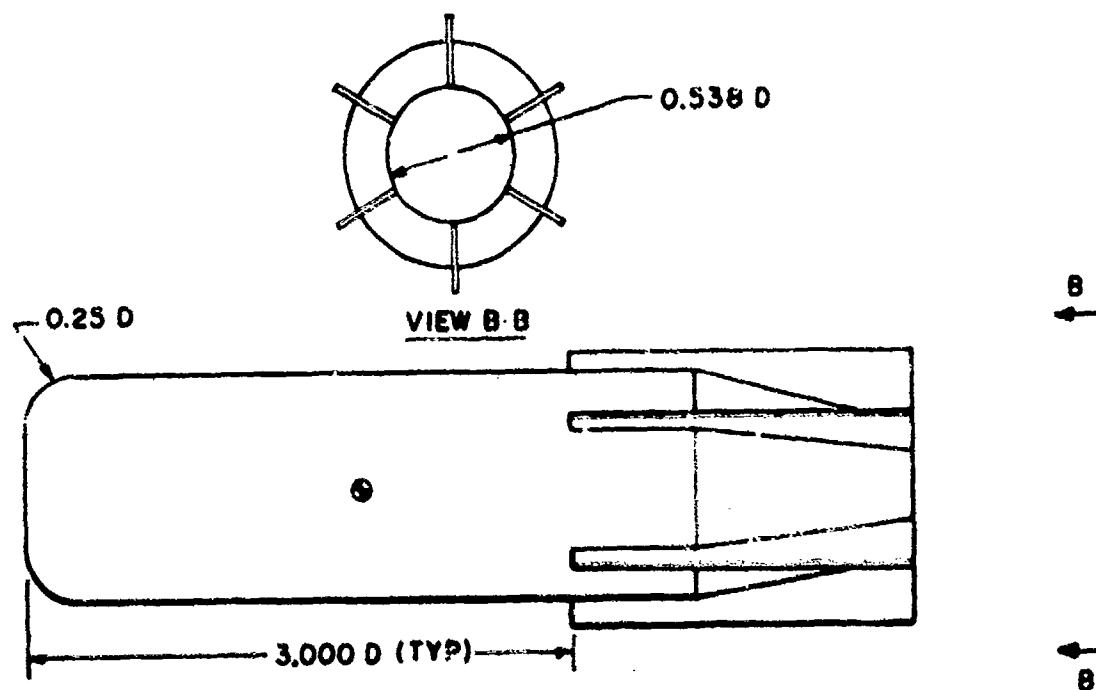
B. AERODYNAMIC CHARACTERISTICS - BASIC S-CURVE CONFIGURATIONS

The original aerodynamic data packages for the basic S-Curve bomblet configurations (Reference 1) have been improved and extended in Mach number as a result of further wind tunnel tests and analyses. This work is reviewed in the following paragraphs.

Wind Tunnel Tests The static and dynamic stability characteristics of the two basic S-Curve bomblet configurations, at Mach numbers from 0.2



a) S-Curve Bomblet: Cylindrical Afterbody



b) S-Curve Bomblet: Boattail Afterbody

Figure 1. Basic S-Curve Bomblet Configurations

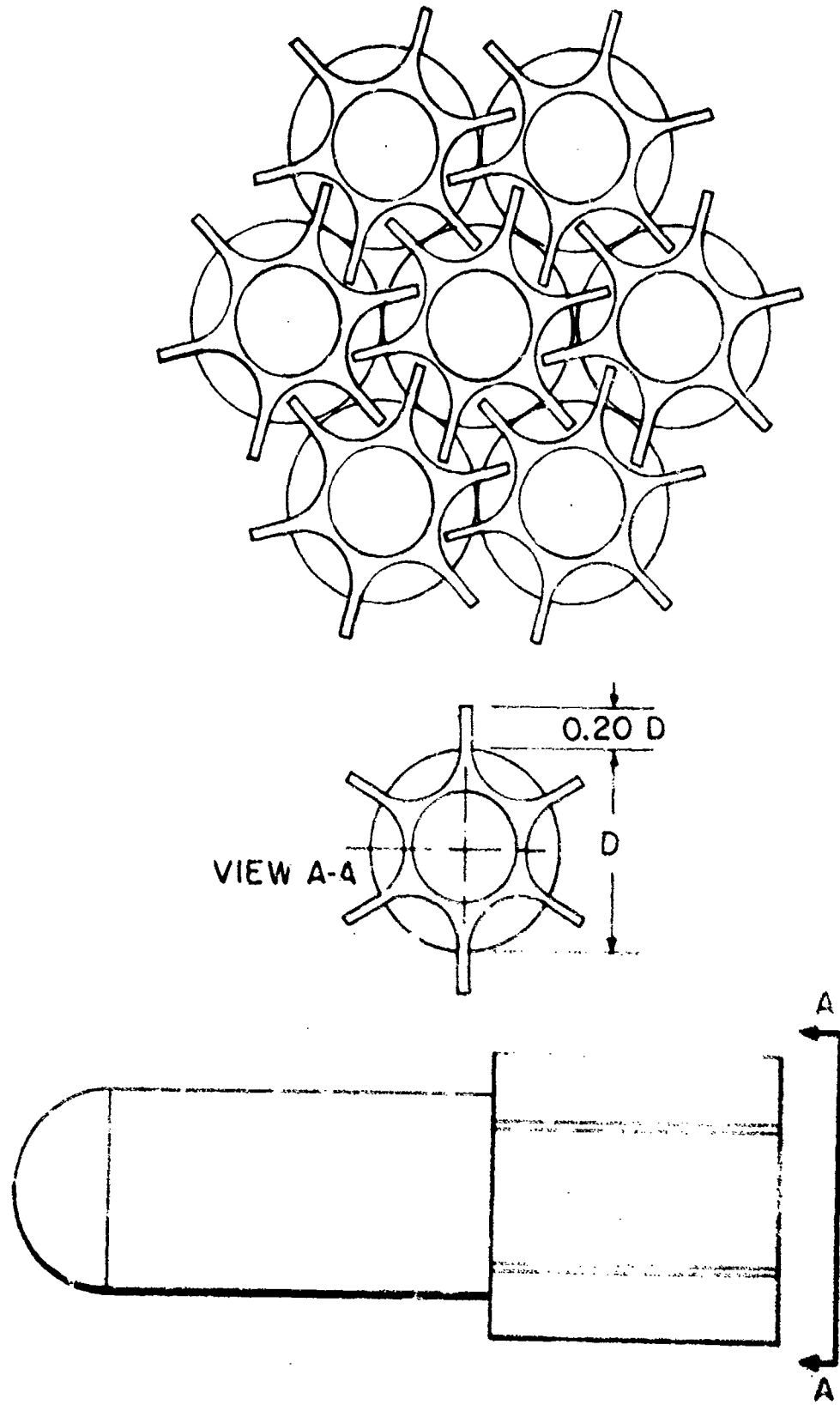
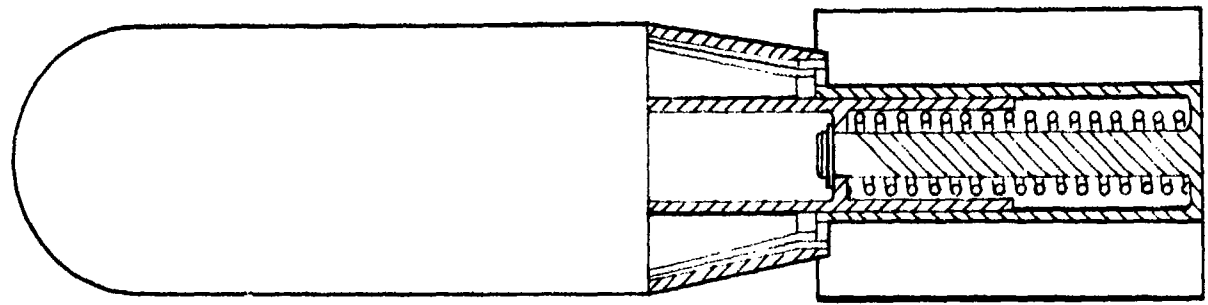
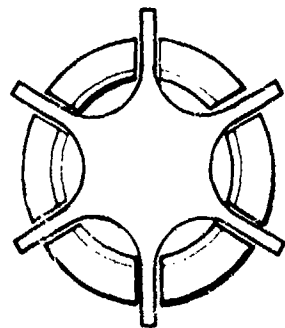


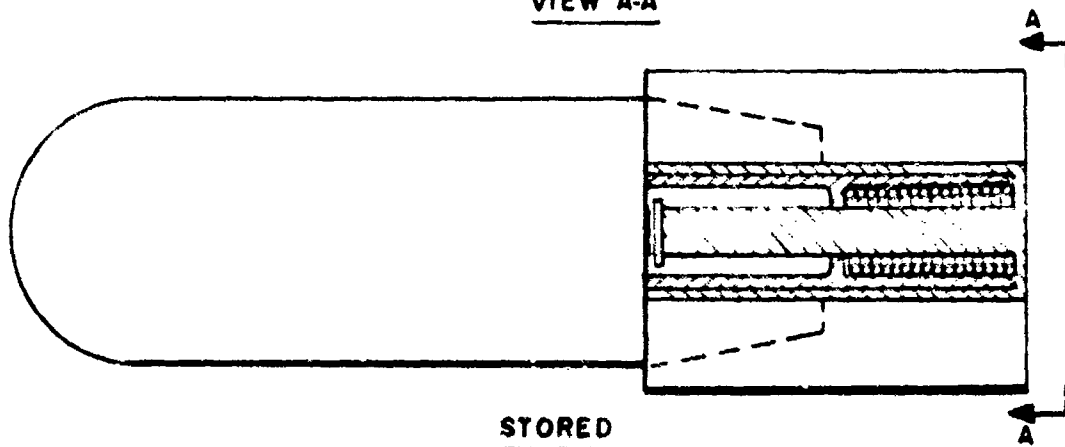
Figure 2. Design Concept for S-Curve Bomblet with Large-Span Fine



DEPLOYED

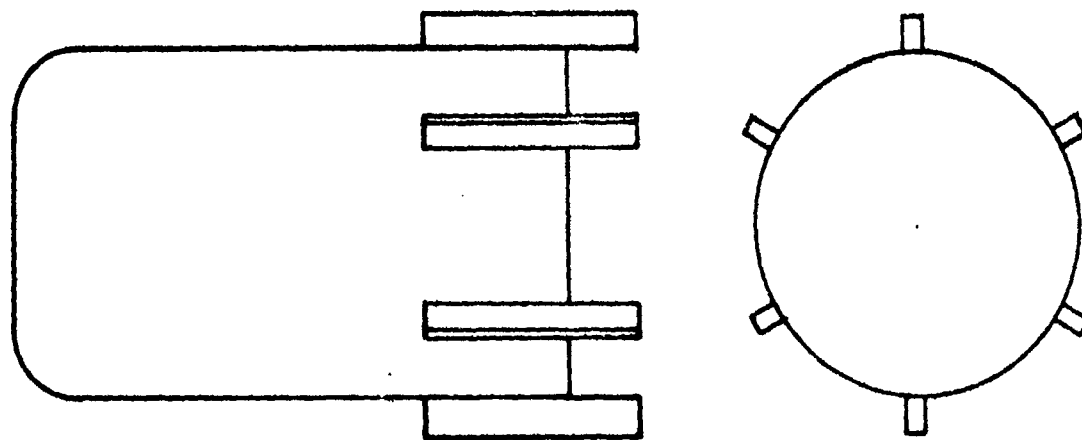


VIEW A-A

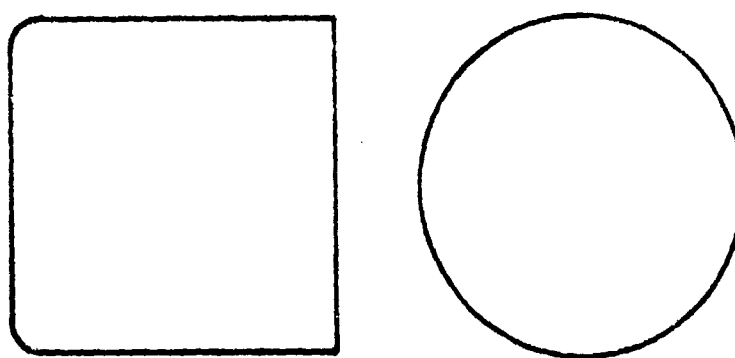


STORED

Figure 3. Design Concept for S-Curve Bomblet with Extensible Fin Assembly



a) Mini-Bomblet



b) Blunt-Nose Cylinder

Figure 4. Low-Fineness Ratio S-Curve Bomblet Configurations

to 1.2, were previously described in References 1, 5, and 9. In this report, only the results of more recent testing will be described. All wind tunnel tests have been accomplished at the Air Force Arnold Engineering Development Center (AEDC) test facilities.

During the period of the present contractual effort, additional static and dynamic stability data for the basic S-Curve configurations were obtained at Mach numbers 1.5, 2.0, and 2.5. Also, magnus data and fin cant effectiveness were obtained at subsonic and transonic conditions and roll damping data were measured at subsonic, transonic, and supersonic Mach numbers. These additional series of tests are described in References 10 and 11.

Subsequently, two new blunt-nose shapes and increased-span fins were evaluated in conjunction with both the cylindrical and boattail afterbody models (References 12 and 13). Static and dynamic stability characteristics of the modified configurations were determined at subsonic and transonic conditions.

Static Aerodynamic Characteristics The supersonic wind tunnel data for the two basic S-Curve configurations show that the static stability increases at supersonic Mach numbers. The S-Curve moment characteristics are retained at supersonic Mach numbers, but the trim angles are less than those at subsonic Mach numbers. The trim characteristics of the two basic bomblet configurations are shown in Figure 5. Note that the trim data for the boattail bomblet are based on a cg position 0.228 calibers aft of that for the cylindrical afterbody bomblet. It is significant that the trim angle of the boattail bomblet varies only slightly as a function of Mach number, whereas the cylindrical afterbody configuration experiences large trim changes through the transonic range.

Dynamic Stability The pitch damping, $C_{m_q} + C_{m_{\dot{\alpha}}}$, increases at supersonic Mach numbers, for both basic configurations. There is only a slight effect of angle of attack on the damping at supersonic Mach numbers.

Magnus Characteristics The magnus tests of the basic cylindrical-afterbody configuration show that the magnus force and moment are considerably less than previous estimates based on the data of Reference 14. Magnus force and moment data at Mach numbers 0.5 and 0.8 are shown in Figure 6. The data were obtained for a test Reynolds number of 550,000 based on body diameter, which corresponds to a flight velocity of about 500 feet/second for a 2-inch diameter bomblet under sea level conditions. Tests at various Reynolds numbers show that the magnus data are sensitive to Reynolds number, particularly for angles of attack greater than about 16 degrees.

The magnus force data for angles of attack less than 20 degrees are positive (negative C_{N_p}) and thus are in agreement with body-alone cross

| <u>CG</u> <u>(CAL)</u> | <u>AFTERBODY</u> |
|---------------------------|------------------|
| —— 1.5 | CYLINDRICAL |
| - - - 1.728 | BOAT TAIL |

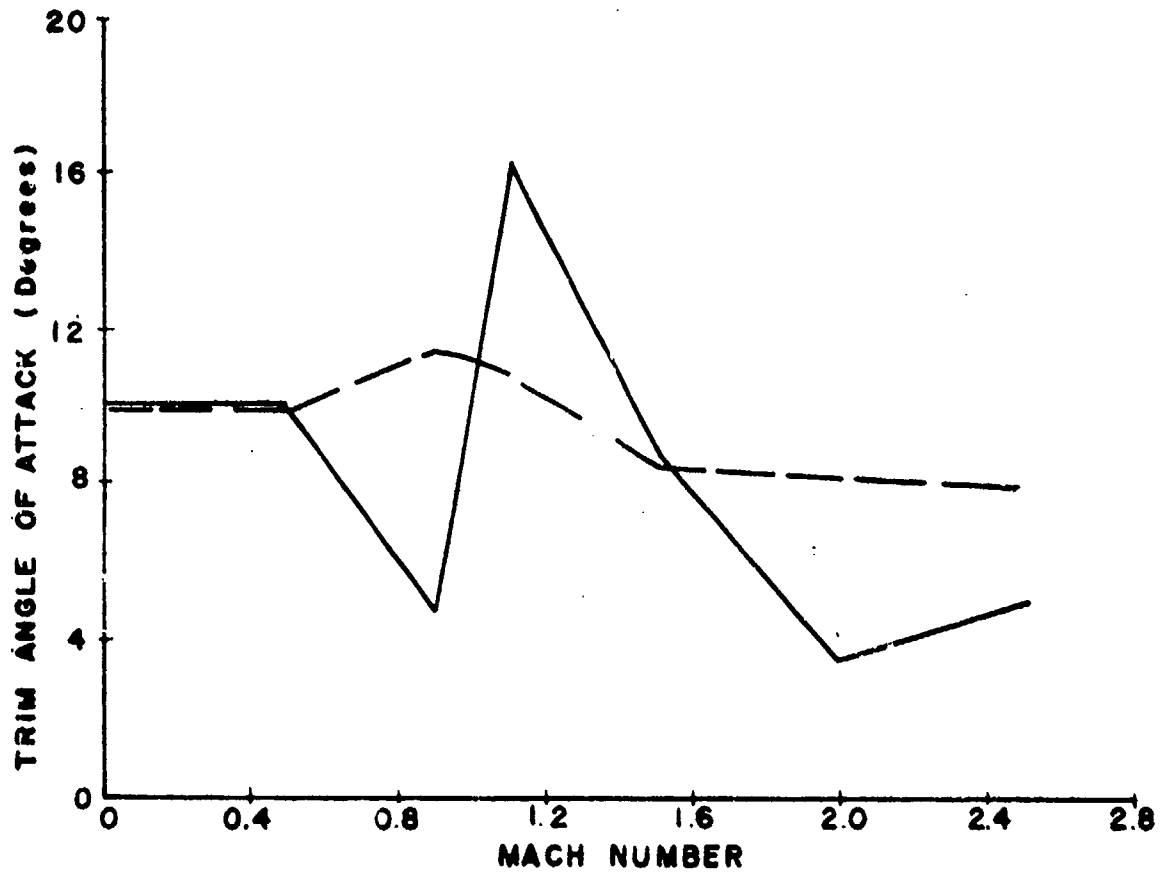


Figure 5. Trim Characteristics of Basic S-Curve Bomblet Configurations

NOSE SHAPE

— NS₂
 - - - NS₁

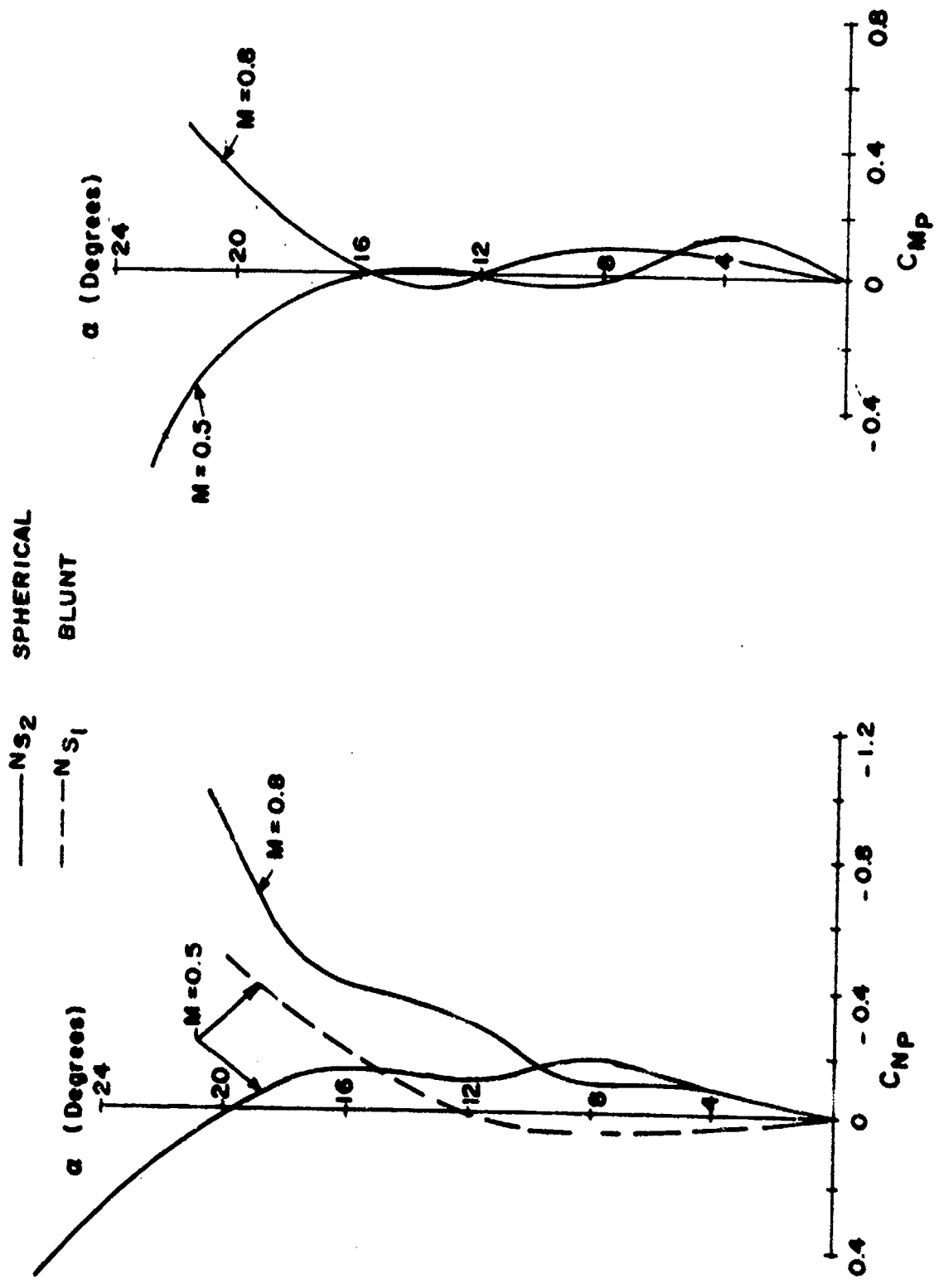


Figure 6. Magnus Force and Moment Characteristics of Basic S-Curve Bomblet with Cylindrical Afterbody

flow predictions based on the applicable cross flow Reynolds number. For angles of attack greater than eight degrees there appears to be some magnus effect due to fin-wake interference, since the magnus force is different for increasing and decreasing spin rates, which has the effect of reversing the magnus force due to fin-wake interference. The effect of nose shape on the magnus characteristics is very pronounced at 0.5 Mach number, and at very large angles of attack the spherical nose bomblet experiences negative magnus forces at $R_{Nd} = 550,000$. However, the magnus force becomes positive if the Reynolds number is decreased. These effects are believed to be due to the fins, since the body-alone magnus characteristics should not be influenced by Reynolds number for these conditions.

It is noteworthy that the magnus force and moment are quite small at the nominal trim angles of attack and, hence, the tendency for coning motion is greatly reduced for the basic S-Curve configurations.

The reason for the large difference between the present results and the Australian Weapons Research Establishment data on a similar shape (Reference 14) is not understood.

The magnus characteristics of the basic S-Curve configurations at supersonic Mach numbers were estimated from data correlations on similar shapes and from consideration of both body-fin interference and cross-flow effects. The resulting coefficients were found to be highly nonlinear with angle of attack.

Spin Characteristics The spin damping coefficient, C_{lp} , was measured for the basic S-Curve configuration (Reference 11) and found to be less than the original estimates presented in Reference 1, although the increase in damping with angle of attack was similar. New estimates for the spin damping at supersonic velocities were required, since spin damping tests were not accomplished for Mach numbers greater than 0.9. The supersonic damping was estimated from the subsonic data, using proportionality factors based on the fin normal force derivative.

The fin effectiveness coefficient, C_{le} , was measured late in the program for the model with large span fins (Reference 13). These data are shown in Figure 7. These coefficients, when corrected for the smaller size basic fins, are still somewhat larger than the estimated curve, which was used for most of the motion simulations.

Effect of Aerodynamic Roll Angle During the present effort, the effect of aerodynamic roll angle on configuration $B_5N_{S2}A_{S1}F_{S2}$ was investigated in the wind tunnel at supersonic Mach numbers (Reference 10). The first harmonic coefficients, C_{SF1} , C_{SM1} , and $C_{L\phi1}$, were evaluated at $\phi = 15$ degrees. For angles of attack less than 10 degrees there is no

ALL DATA FOR
CYLINDRICAL AFTERBODY

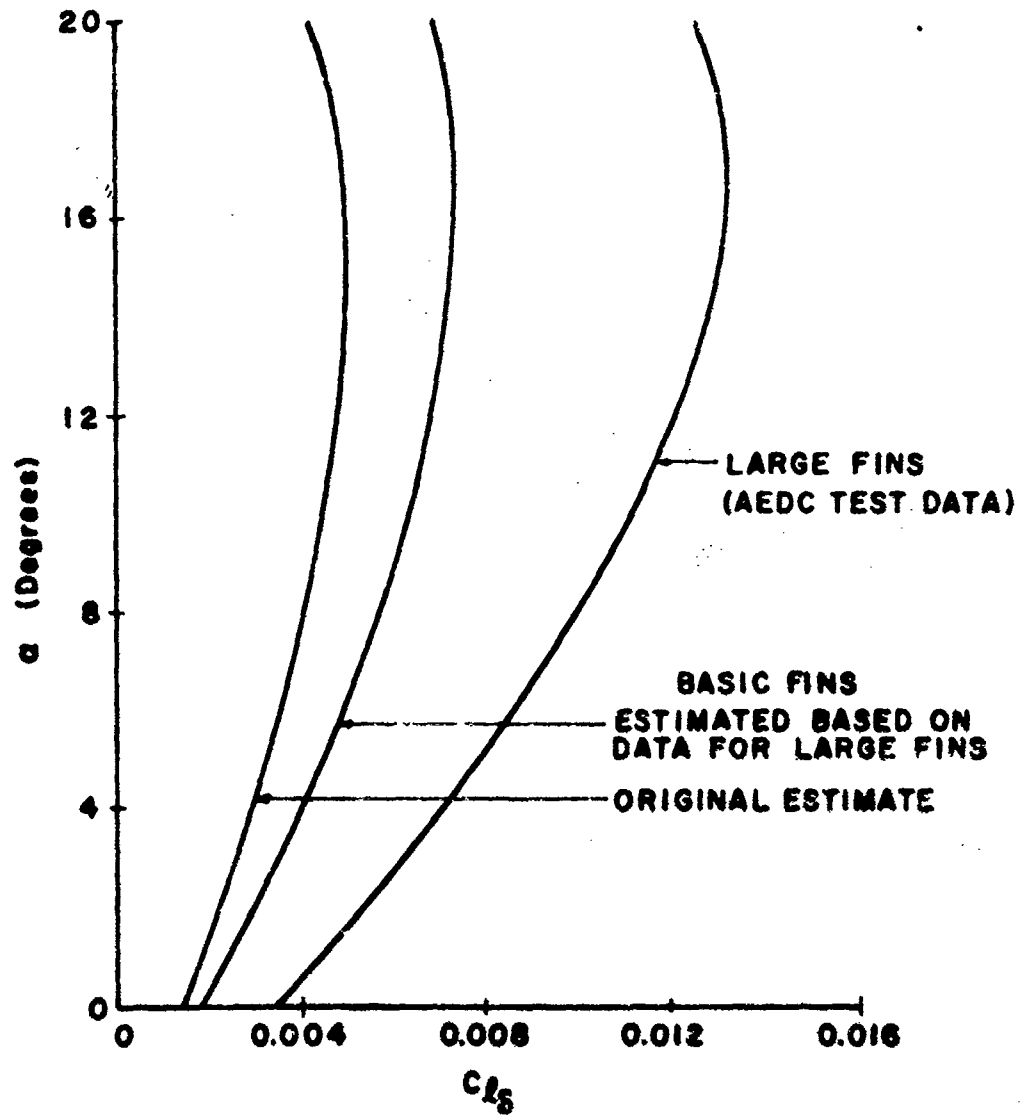


Figure 7. Spin Characteristics of Basic S-Curve Configuration - Roll Torque Due to Cant

significant effect due to aerodynamic roll angle, but at larger angles of attack these coefficients increase rapidly and become very nonlinear with angle of attack. The induced roll and side moment coefficients, C_{SM} and $C_{L\phi}$, are plotted in Figure 8 and compared with the subsonic results.

Effect of Asymmetrical Nose-Roughness It has been reported that asymmetrical nose roughness can have a significant effect on the side force, side moment, and roll moment (Reference 15). If nose roughness is confined to a single meridional orientation, the above coefficients can experience an abrupt change in magnitude and sign when the body-fixed roughness plane and the angle of attack plane coincide. A typical variation of the side moment coefficient variation as a function of the aerodynamic roll angle is depicted in Figure 9.

To model such affects in the 6-DOF computer program, a special aerodynamic step function was provided, which together with first and second order roll dependent harmonics, permitted a close approximation of the test data. Figure 9 also shows a typical fit obtained with the step function and harmonics. Provision was also made for the step function to have a different phase for the side moment and the roll moment.

The asymmetrical nose-roughness effect was not incorporated for all of the 6-DOF motion simulations, but was investigated as a separate and distinct aerodynamic asymmetry.

Effect of Increased Span Fins The effect of increasing the exposed semi-span of the basic S-Curve bomblet fins from 0.078 caliber to 0.14 caliber was investigated as a means of improving the bomblet allowable cg range. The effect of the larger fins on the normal force center of pressure is depicted in Figure 10. The increased fin span allows a 0.3 caliber aft cg shift for the cylindrical afterbody configuration and a 0.15 caliber aft cg shift for the boattail afterbody configuration at subsonic conditions. The larger fins allow the cg to be at or near the body midpoint. Data are also shown for a configuration with increased nose curvature. Although the center-of-pressure is moved rearward, the S-Curve moment characteristic is lost, since the center of pressure moves forward with increasing angle of attack.

The increase in fin span was found to have negligible effect on the induced aerodynamic forces and moment coefficients, C_{SF} , C_{SM} , and $C_{L\phi}$ for angles of attack less than 12 degrees. For angles of attack larger than 20 degrees there is some difference in the induced aerodynamic coefficients for the two different fin sizes, particularly the roll moment, $C_{L\phi}$.

The magnus force coefficients for configuration B₅N₅₂A₅₁F₅₅, with the increased span fins, are about equal or less than those for the smaller fins at angles of attack less than eight degrees. The Magnus data for

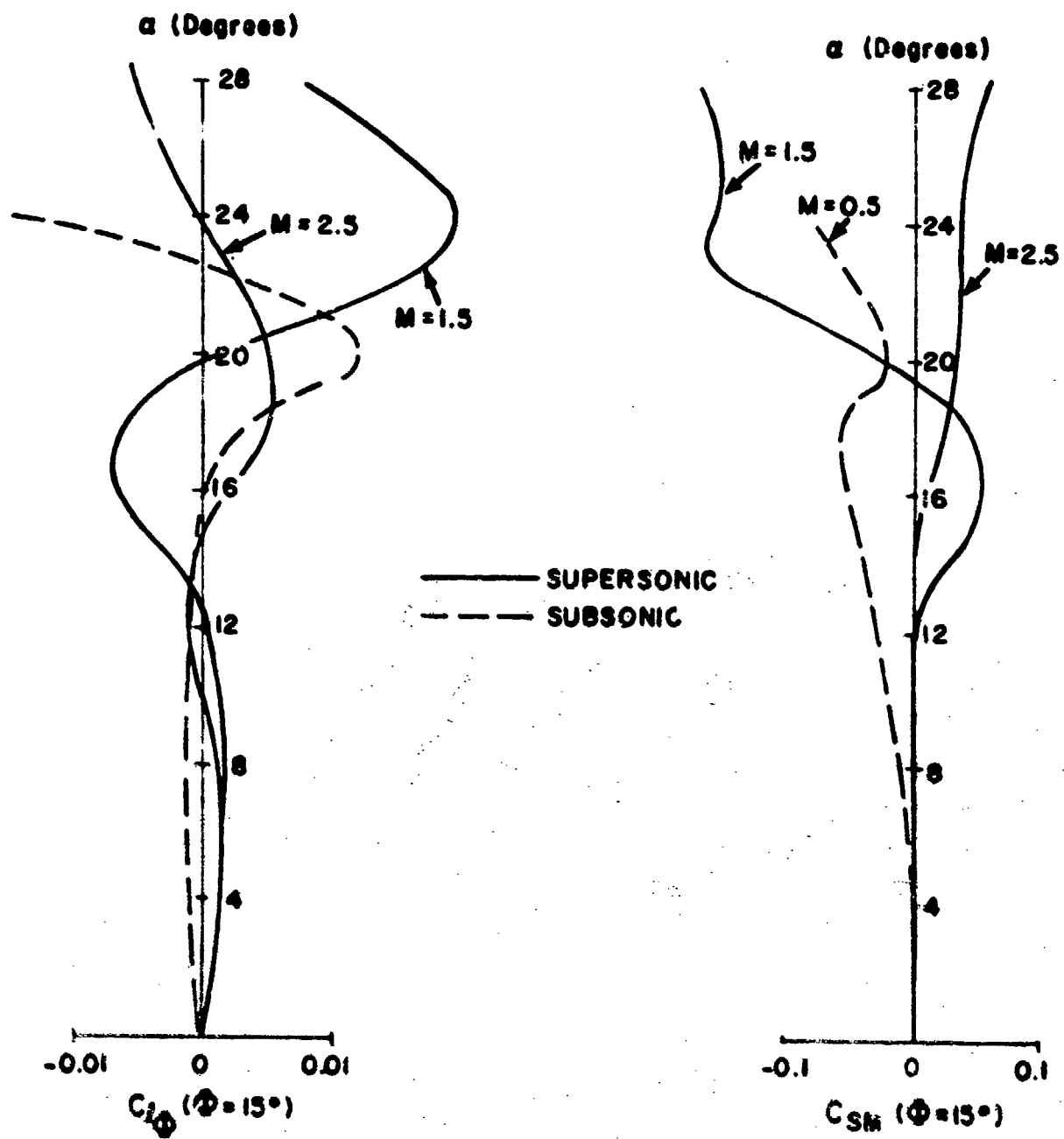


Figure 8. Induced Aerodynamic Moment Characteristics of Basic S-Curve Bomblet Configuration

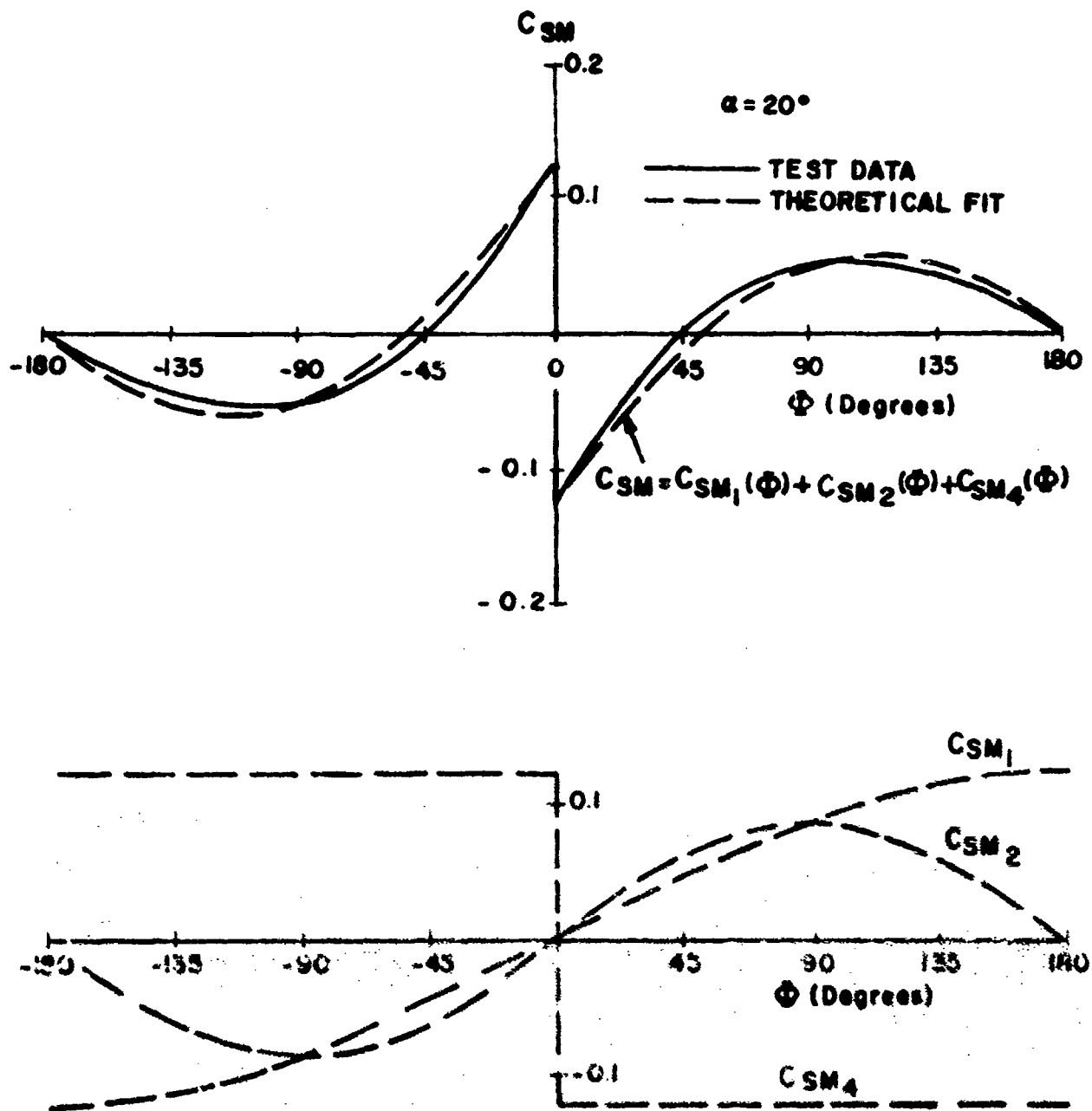


Figure 9. Effect of Nose-Roughness on the Induced Aerodynamic Side Moment

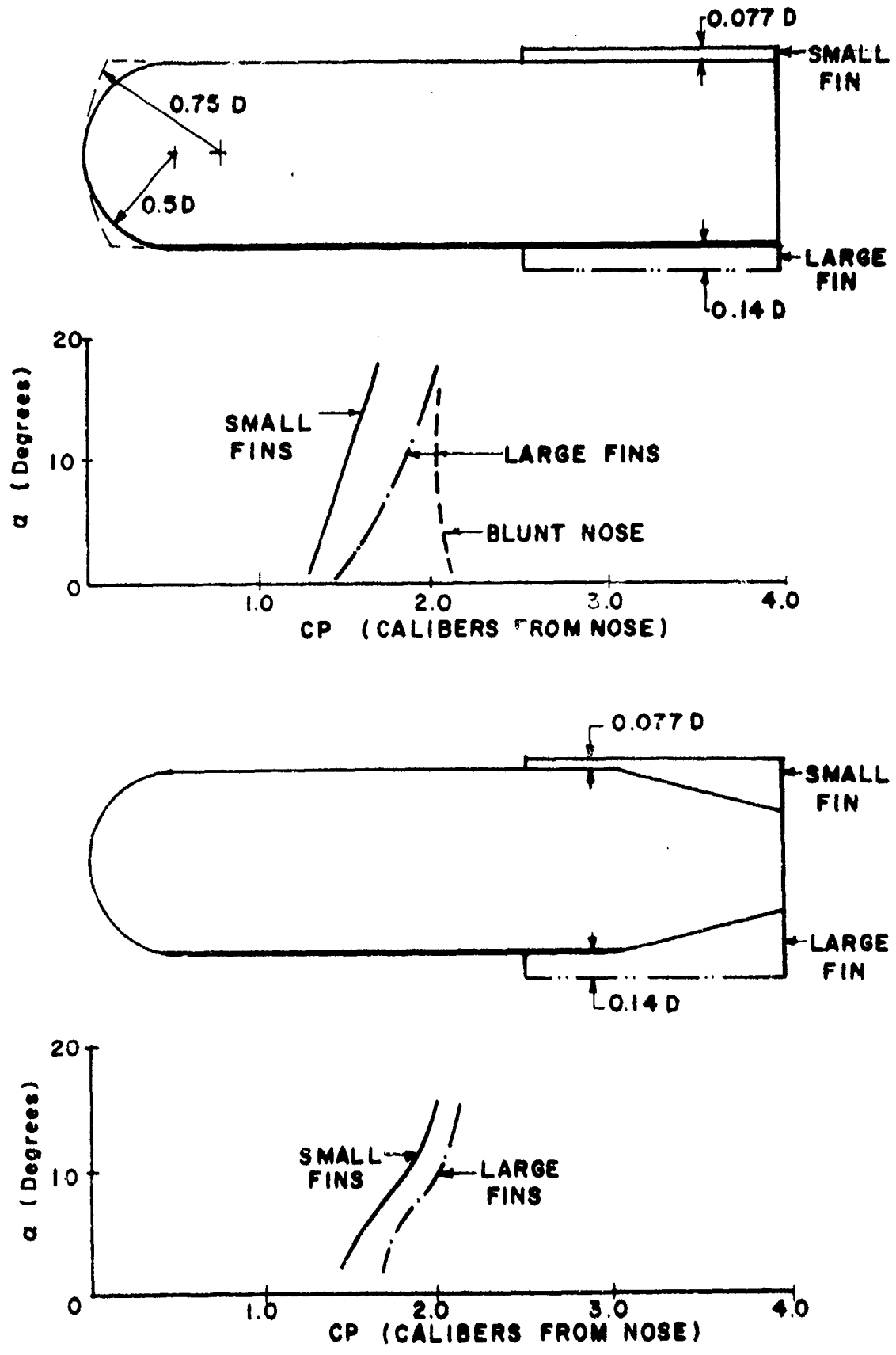


Figure 10. Effect of S-Curve Bomblet Configuration on Normal Force Center of Pressure

configuration $B_5N_5A_5F_5$ are described in Reference 13. At angles of attack greater than twenty degrees the magnus force becomes increasingly positive ($C_{N_p} < 0$) for the large fins. The magnus moment, in contrast, is significantly increased for the larger fins at all angles of attack less than about twenty degrees, and C_{M_p} is positive throughout this angle of attack range for Mach numbers of 0.9 and less. The magnus moment coefficients for the configuration with large fins are highly nonlinear with angle of attack, and C_{M_p} becomes negative for angles of attack greater than twenty degrees. Interestingly, positive fin cant reduces the magnus moment, and for 3 degrees cant the magnus moment is near zero for subsonic Mach numbers and angles of attack less than about 10 degrees.

Aerodynamic Coefficients - 6-DOF Simulations A tabulation of the aerodynamic coefficients used for the 6-DOF motion simulations are presented in Tables I and II for the basic cylindrical afterbody and boattail afterbody configurations, respectively. The aerodynamic coefficients are tabulated both as a function of Mach number and angle of attack. Coefficients are shown for only five Mach numbers because of the limitation of the 6-DOF trajectory program. A detailed description of the coefficient definitions can be found in References 3 and 16. The coefficients are divided into two groups; the first group of coefficients represents the aerobalistic coefficients which are independent of the y-z body-axis roll orientation. The second group of coefficients is applicable only to a specific set of y-z body-fixed axes, which are aligned with a plane of rotational symmetry. This second group of coefficients defines the induced aerodynamic forces and moments, which are harmonic functions of the aerodynamic roll angle, as well as the coefficients which describe the configurational and aerodynamic asymmetries.

C. PREDICTED FLIGHT DYNAMICS OF BASIC CONFIGURATIONS

Effect of Roll Dependent Aerodynamic Coefficients The addition of roll dependent aerodynamic coefficients, C_{S_p} , C_{SM} , and $C_{\lambda\phi_1}$, to the previous 6-DOF motion simulations (Reference 1) produced some interesting results.¹ For small configurational asymmetries and small cant angles, it was found that roll lock-in was occurring for nearly all of the computed motion histories. It was also noted that the lock-in was not a direct result of the roll torques. It was discovered that the lock-in is critically affected by the roll dependent side moment. A re-examination of the equation for zero coning motion (Appendix I) has shown that for zero roll rate the roll dependent side moment must have a positive gradient with respect to the

¹ The induced aerodynamic coefficients were not included in the original S-Curve bomblet simulations, Reference 1.

TABLE I. AERODYNAMIC COEFFICIENT SUMMARY FOR BASIC S-CURVE CONFIGURATION B_SN_{S2}A_{S1}F_{S2}

| | | AERODYNAMIC COEFFICIENTS | | | | | | | | | | | | |
|--|-------------|---------------------------|------|------|------|------|------|------|------|------|------|------|------|------|
| Coefficient | Mach Number | Angle of Attack - Degrees | | | | | | | | | | | | |
| | | 0 | 2 | 4 | 6 | 8 | 10 | 12 | 16 | 20 | 24 | 30 | 60 | 90 |
| C _A | 0.5 | .18 | .18 | .19 | .20 | .22 | .23 | .24 | .26 | .26 | .22 | .15 | .075 | 0 |
| | 0.9 | .36 | .37 | .39 | .42 | .44 | .47 | .49 | .52 | .54 | .56 | .50 | .25 | 0 |
| | 1.1 | .70 | .71 | .72 | .75 | .78 | .80 | .82 | .84 | .88 | .90 | .85 | .42 | 0 |
| | 1.5 | .97 | .99 | .99 | .99 | .99 | 1.00 | 1.00 | 1.00 | 1.04 | 1.00 | .97 | .48 | 0 |
| 2.5 | .97 | .99 | .99 | .99 | .99 | 1.00 | 1.00 | 1.01 | 1.01 | .99 | .96 | .91 | .45 | 0 |
| C _N | 0.5 | 0 | .12 | .24 | .34 | .46 | .58 | .72 | 1.0 | 1.34 | 1.70 | 2.19 | 6.5 | 5.44 |
| | 0.9 | 0 | .13 | .26 | .38 | .52 | .64 | .87 | 1.20 | 1.62 | 2.14 | 2.63 | 6.1 | 6.10 |
| | 1.1 | 0 | .10 | .22 | .34 | .54 | .66 | .84 | 1.30 | 1.84 | 2.50 | 3.00 | 6.8 | 7.31 |
| | 1.5 | 0 | .12 | .24 | .40 | .66 | .76 | .96 | 1.46 | 2.02 | 2.77 | 3.45 | 6.3 | 7.31 |
| 2.5 | 0 | .11 | .22 | .34 | .48 | .64 | .81 | 1.19 | 1.71 | 2.08 | 2.75 | 5.8 | 7.15 | |
| C _M | 0.5 | 0 | .020 | .035 | .035 | .023 | .002 | .028 | .140 | .33 | .56 | 1.15 | 6.17 | 6.65 |
| | 0.9 | 0 | .045 | .055 | .077 | .102 | .125 | .180 | .320 | .56 | .66 | .76 | 4.27 | 6.72 |
| | 1.1 | 0 | .058 | .105 | .142 | .163 | .175 | .175 | .205 | .40 | .48 | 1.60 | 6.17 | 7.46 |
| | 1.5 | 0 | .045 | .067 | .063 | .045 | .010 | .110 | .173 | .4 | 1.17 | 1.80 | 5.94 | 7.18 |
| 2.5 | 0 | .013 | .012 | .010 | .055 | .110 | .240 | .490 | .77 | 1.04 | 1.34 | 5.22 | 7.22 | |
| C _{NP} (Body Fixed) | 0.5 | 0 | .965 | .13 | .16 | .19 | .17 | .17 | .1 | .01 | .30 | .2 | 1.55 | 1.29 |
| | 0.9 | 0 | 0 | 0 | .11 | .20 | .27 | .37 | .40 | 1.00 | 1.50 | 1.7 | 0 | 0 |
| | 1.1 | 0 | 0 | 0 | .11 | .20 | .27 | .37 | .40 | 1.00 | 1.50 | 1.7 | 0 | 0 |
| | 1.5 | 0 | .16 | .35 | .44 | .37 | .28 | .15 | .48 | .3 | .27 | .3 | 0 | 0 |
| 2.5 | 0 | .18 | .32 | .27 | .27 | .27 | .21 | .09 | .3 | .3 | .3 | 0 | 0 | |
| C _{MP} | 0.5 | 0 | .05 | .10 | .07 | .02 | .51 | 0 | .02 | .7 | .8 | 1.33 | 6.1 | 7.3 |
| | 0.9 | 0 | .01 | .02 | .03 | .04 | .09 | .12 | .08 | .8 | 1.1 | 1.18 | 0 | 0 |
| | 1.1 | 0 | .01 | .02 | .03 | .04 | .09 | .12 | .08 | .8 | 1.1 | 1.18 | 0 | 0 |
| | 1.5 | 0 | .41 | .82 | .93 | .88 | .73 | .44 | .26 | .8 | .85 | .85 | 0 | 0 |
| 2.5 | 0 | .36 | .48 | .3 | .49 | .48 | .31 | .23 | .8 | .85 | .85 | 0 | 0 | |
| C _{MQ} | 0.5 | 15 | 17 | 19 | 21 | 23 | 25 | 26 | 25 | 22 | 17 | 14 | 24 | 24 |
| | 0.9 | 23 | 31 | 38 | 45 | 57 | 7 | 17 | 29 | 37 | 37 | 34 | 33 | 34 |
| | 1.1 | 32 | 33 | 34 | 35 | 36 | 3 | 14 | 40 | 40 | 38 | 38 | 33 | 33 |
| | 1.5 | 37 | 38 | 39 | 40 | 40 | 40 | 40 | 40 | 40 | 40 | 40 | 33 | 25 |
| 2.5 | 24 | 24 | 4 | 24 | 24 | 24 | 24 | 24 | 24 | 24 | 24 | 24 | 24 | |
| C _{NP} | 0.5 | 1 | 1 | 1 | 1 | 1 | 1 | 1 | 1 | 1 | 1 | 1 | 1 | 1 |
| | 0.9 | 23 | 31 | 38 | 45 | 57 | 7 | 17 | 29 | 37 | 37 | 34 | 33 | 34 |
| | 1.1 | 32 | 33 | 34 | 35 | 36 | 3 | 14 | 40 | 40 | 38 | 38 | 33 | 33 |
| | 1.5 | 37 | 38 | 39 | 40 | 40 | 40 | 40 | 40 | 40 | 40 | 40 | 33 | 25 |
| 2.5 | 24 | 24 | 4 | 24 | 24 | 24 | 24 | 24 | 24 | 24 | 24 | 24 | 24 | |
| C _{NPR} (A _{S1}) | 0.5 | 0 | 0 | 0 | 0 | 0 | 0 | 0 | 0 | 0 | 0 | 0 | 0 | 0 |
| | 0.9 | 0 | 0 | 0 | 0 | 0 | 0 | 0 | 0 | 0 | 0 | 0 | 0 | 0 |
| | 1.1 | 0 | 0 | 0 | 0 | 0 | 0 | 0 | 0 | 0 | 0 | 0 | 0 | 0 |
| | 1.5 | 0 | 0 | 0 | 0 | 0 | 0 | 0 | 0 | 0 | 0 | 0 | 0 | 0 |
| C _{NPR} (A _{S2}) | 0.5 | 0 | 0 | 0 | 0 | 0 | 0 | 0 | 0 | 0 | 0 | 0 | 0 | 0 |
| | 0.9 | 0 | 0 | 0 | 0 | 0 | 0 | 0 | 0 | 0 | 0 | 0 | 0 | 0 |
| | 1.1 | 0 | 0 | 0 | 0 | 0 | 0 | 0 | 0 | 0 | 0 | 0 | 0 | 0 |
| | 1.5 | 0 | 0 | 0 | 0 | 0 | 0 | 0 | 0 | 0 | 0 | 0 | 0 | 0 |
| C _{NPR} (A _{S2}) | 0.5 | 0 | 0 | 0 | 0 | 0 | 0 | 0 | 0 | 0 | 0 | 0 | 0 | 0 |
| | 0.9 | 0 | 0 | 0 | 0 | 0 | 0 | 0 | 0 | 0 | 0 | 0 | 0 | 0 |
| | 1.1 | 0 | 0 | 0 | 0 | 0 | 0 | 0 | 0 | 0 | 0 | 0 | 0 | 0 |
| | 1.5 | 0 | 0 | 0 | 0 | 0 | 0 | 0 | 0 | 0 | 0 | 0 | 0 | 0 |
| C _{NPR} (A _{S2}) | 0.5 | 0 | 0 | 0 | 0 | 0 | 0 | 0 | 0 | 0 | 0 | 0 | 0 | 0 |
| | 0.9 | 0 | 0 | 0 | 0 | 0 | 0 | 0 | 0 | 0 | 0 | 0 | 0 | 0 |
| | 1.1 | 0 | 0 | 0 | 0 | 0 | 0 | 0 | 0 | 0 | 0 | 0 | 0 | 0 |
| | 1.5 | 0 | 0 | 0 | 0 | 0 | 0 | 0 | 0 | 0 | 0 | 0 | 0 | 0 |

TABLE II. AERODYNAMIC COEFFICIENT SUMMARY FOR BASIC S-CURVE CONFIGURATION B_SN_{S1}A_{S2}F_{S3}

| AEROBALLISTIC COEFFICIENTS | | | | | | | | | | | | | | |
|--|-------------|-------------------------|------|------|------|------|------|------|------|------|------|------|------|------|
| Coefficient | Mach Number | Angle of Attack Degrees | | | | | | | | | | | | |
| | | 0 | 2 | 4 | 6 | 8 | 10 | 12 | 14 | 16 | 20 | 24 | 30 | 40 |
| C _X | 0.5 | .100 | .103 | .128 | .154 | .169 | .174 | .181 | .218 | .245 | .281 | .291 | .15 | 0 |
| | 0.9 | .188 | .199 | .418 | .414 | .461 | .478 | .495 | .525 | .565 | .624 | .682 | .15 | 0 |
| | 1.1 | .798 | .802 | .809 | .818 | .830 | .842 | .842 | .924 | .936 | .959 | .959 | .48 | 0 |
| | 1.5 | 1.11 | 1.10 | 1.08 | 1.07 | 1.08 | 1.08 | 1.08 | 1.09 | 1.06 | 1.01 | .96 | .48 | 0 |
| | 2.5 | 1.17 | 1.17 | 1.17 | 1.16 | 1.16 | 1.16 | 1.16 | 1.14 | 1.12 | 1.08 | .99 | .76 | 0 |
| C _N | 0.5 | 0 | .12 | .22 | .34 | .50 | .68 | .86 | 1.24 | 1.67 | 2.15 | 2.96 | 6.50 | 5.65 |
| | 0.9 | 0 | .06 | .14 | .27 | .44 | .67 | .82 | 1.22 | 1.66 | 2.15 | 2.96 | 6.10 | 6.10 |
| | 1.1 | 0 | .14 | .27 | .41 | .61 | .83 | 1.08 | 1.62 | 2.20 | 2.75 | 1.82 | 6.81 | 7.31 |
| | 1.5 | 0 | .14 | .28 | .44 | .63 | .84 | 1.07 | 1.59 | 2.11 | 2.74 | 3.50 | 6.10 | 7.31 |
| | 2.5 | 0 | .10 | .21 | .33 | .47 | .64 | .76 | 1.12 | 1.51 | 1.76 | 2.63 | 5.80 | 7.15 |
| C _M | 0.5 | 0 | .051 | .092 | .099 | .059 | 0 | .078 | .254 | .411 | .644 | 1.21 | 4.69 | 5.16 |
| | 0.9 | 0 | .040 | .067 | .090 | .090 | .038 | .011 | .080 | .150 | .160 | .17 | 2.88 | 4.83 |
| | 1.1 | 0 | .086 | .116 | .123 | .079 | .044 | .054 | .241 | .428 | .550 | .71 | 4.57 | 5.79 |
| | 1.5 | 0 | .021 | .030 | .023 | .010 | .018 | .069 | .140 | .190 | .195 | .87 | 3.69 | 5.79 |
| | 2.5 | 0 | .011 | .017 | .016 | 0 | .025 | .057 | .111 | .241 | .307 | .63 | 3.90 | 5.66 |
| C _{NP} (Body Fixed) | 0.5 | 0 | .07 | .17 | .12 | .10 | .16 | .12 | 0 | .10 | .10 | .60 | 1.55 | 1.20 |
| | 0.9 | 0 | .10 | .20 | .11 | .11 | .14 | .12 | 1.28 | 2.00 | 1.50 | 1.25 | 0 | 0 |
| | 1.1 | 0 | 0 | 0 | .11 | .20 | .27 | .17 | .60 | 1.10 | 1.50 | 1.25 | 0 | 0 |
| | 1.5 | 0 | .16 | .15 | .44 | .37 | .08 | .35 | .46 | .14 | .22 | 0 | 0 | 0 |
| | 2.5 | 0 | .16 | .12 | .07 | .27 | .21 | .09 | 0 | 0 | 0 | 0 | 0 | 0 |
| C _{MP} | 0.5 | 0 | .07 | .10 | .09 | .07 | .01 | .08 | .40 | .75 | .85 | .40 | 2.60 | 2.0 |
| | 0.9 | 0 | .02 | .04 | .00 | .47 | .43 | .17 | .54 | .85 | 1.42 | 1.48 | 0 | 0 |
| | 1.1 | 0 | .01 | .07 | .01 | .04 | .06 | .17 | .06 | .80 | 1.42 | 1.48 | 0 | 0 |
| | 1.5 | 0 | .41 | .42 | .93 | .85 | .20 | .44 | .86 | .78 | .60 | 0 | 0 | 0 |
| | 2.5 | 0 | .36 | .34 | .11 | .41 | .48 | .41 | .21 | 0 | 0 | 0 | 0 | 0 |
| C _{MU} | 0.5 | 20.5 | 22.5 | 23.0 | 23.0 | 23.0 | 23.0 | 23.0 | 23.0 | 23.0 | 23.0 | 23.0 | 23.0 | 23.0 |
| | 0.9 | 22.5 | 22.5 | 22.5 | 22.5 | 22.5 | 22.5 | 22.5 | 22.5 | 22.5 | 22.5 | 22.5 | 22.5 | 22.5 |
| | 1.1 | 22.5 | 22.5 | 22.5 | 22.5 | 22.5 | 22.5 | 22.5 | 22.5 | 22.5 | 22.5 | 22.5 | 22.5 | 22.5 |
| | 1.5 | 24.0 | 24.0 | 24.0 | 24.0 | 24.0 | 24.0 | 24.0 | 24.0 | 24.0 | 24.0 | 24.0 | 24.0 | 24.0 |
| | 2.5 | 24.0 | 24.0 | 24.0 | 24.0 | 24.0 | 24.0 | 24.0 | 24.0 | 24.0 | 24.0 | 24.0 | 24.0 | 24.0 |
| C _{NU} | 0.5 | 20.5 | 22.5 | 23.0 | 23.0 | 23.0 | 23.0 | 23.0 | 23.0 | 23.0 | 23.0 | 23.0 | 23.0 | 23.0 |
| | 0.9 | 22.5 | 22.5 | 22.5 | 22.5 | 22.5 | 22.5 | 22.5 | 22.5 | 22.5 | 22.5 | 22.5 | 22.5 | 22.5 |
| | 1.1 | 22.5 | 22.5 | 22.5 | 22.5 | 22.5 | 22.5 | 22.5 | 22.5 | 22.5 | 22.5 | 22.5 | 22.5 | 22.5 |
| | 1.5 | 24.0 | 24.0 | 24.0 | 24.0 | 24.0 | 24.0 | 24.0 | 24.0 | 24.0 | 24.0 | 24.0 | 24.0 | 24.0 |
| | 2.5 | 24.0 | 24.0 | 24.0 | 24.0 | 24.0 | 24.0 | 24.0 | 24.0 | 24.0 | 24.0 | 24.0 | 24.0 | 24.0 |
| C _{MP1} C _{MP2} | 0.5 | 0 | 0 | 0 | 0 | 0 | 0 | 0 | 0 | 0 | 0 | 0 | 0 | 0 |
| | 0.9 | 0 | 0 | 0 | 0 | 0 | 0 | 0 | 0 | 0 | 0 | 0 | 0 | 0 |
| | 1.1 | 0 | 0 | 0 | 0 | 0 | 0 | 0 | 0 | 0 | 0 | 0 | 0 | 0 |
| | 1.5 | 0 | 0 | 0 | 0 | 0 | 0 | 0 | 0 | 0 | 0 | 0 | 0 | 0 |
| | 2.5 | 0 | 0 | 0 | 0 | 0 | 0 | 0 | 0 | 0 | 0 | 0 | 0 | 0 |
| C _Y C _{Y1} C _{Y2} | 0.5 | 0 | 0 | 0 | 0 | 0 | 0 | 0 | 0 | 0 | 0 | 0 | 0 | 0 |
| | 0.9 | 0 | 0 | 0 | 0 | 0 | 0 | 0 | 0 | 0 | 0 | 0 | 0 | 0 |
| | 1.1 | 0 | 0 | 0 | 0 | 0 | 0 | 0 | 0 | 0 | 0 | 0 | 0 | 0 |
| | 1.5 | 0 | 0 | 0 | 0 | 0 | 0 | 0 | 0 | 0 | 0 | 0 | 0 | 0 |
| | 2.5 | 0 | 0 | 0 | 0 | 0 | 0 | 0 | 0 | 0 | 0 | 0 | 0 | 0 |
| C _Z C _{Z1} C _{Z2} | 0.5 | 0 | 0 | 0 | 0 | 0 | 0 | 0 | 0 | 0 | 0 | 0 | 0 | 0 |
| | 0.9 | 0 | 0 | 0 | 0 | 0 | 0 | 0 | 0 | 0 | 0 | 0 | 0 | 0 |
| | 1.1 | 0 | 0 | 0 | 0 | 0 | 0 | 0 | 0 | 0 | 0 | 0 | 0 | 0 |
| | 1.5 | 0 | 0 | 0 | 0 | 0 | 0 | 0 | 0 | 0 | 0 | 0 | 0 | 0 |
| | 2.5 | 0 | 0 | 0 | 0 | 0 | 0 | 0 | 0 | 0 | 0 | 0 | 0 | 0 |

Reference: 1978, Body Number
 Ref length: 4
 Ref location: 1/3rd from nose

aerodynamic roll angle for the zero coning solutions to be stable, i. e.,

$$\frac{d C_{SM}}{d \phi} > 0 \quad : \text{ stable zero coning}$$

Figure 11 illustrates the side moment coefficient variation with ϕ for configuration $B_S N_{S2} A_{S1} F_{S2}$ and the values of ϕ at lock-in for a series of ten trajectories which included both roll dependent moments and cg lateral offset. In all cases lock-in occurs in regions where the inequality is satisfied.

The lock-in condition implies that the roll rate and coning rates are identical, so that zero coning is possible only for the singular case of zero roll rate. Although the side moment controls the region of lock-in, the specific lock-in conditions are determined by the roll torques. The effect of the roll torques will be discussed next.

Effect of CG Lateral Offset Since for small cant angles lock-in can be expected from the side moment, as described above, it is important to see how the lock-in may influence the roll dynamics, since the roll rate and coning rate will be identical. The roll dynamics can be greatly influenced by cg lateral offset, as well as by the fin cant and fin-induced aerodynamic moments. From the diagram of Figure 12, it is seen that the roll moment due to cg offset is²

$$C_r = C_N \frac{\Delta Y}{d} \sin \xi \quad (1)$$

where

$$\xi = \pi/2 - \phi + \zeta$$

Thus, the roll moment due to cg offset depends both upon the aerodynamic roll angle, ϕ , and the orientation of the fin symmetry planes with respect to the orientation of the cg offset, which is given by the angle ζ . For a particular bomblet ζ is a constant, while the aerodynamic roll angle, ϕ , is influenced strongly by the fact that the motion tends toward a condition where $d C_{SM}/d \phi$ has a positive gradient. This implies that the angle ξ , which controls the roll moment due to cg lateral offset, will have discontinuous ranges of values, and consequently, the induced roll moment itself will change incrementally, depending upon the lock-in angle. The induced roll moment due to cg offset reaches a maximum when ξ has values of $\pi/2, 3\pi/2, \text{ etc.}$

² Equation (1) assumes that all other transverse aerodynamic forces are zero.

C_{SM} SHOWN FOR
 α TRIM = 16 Degrees

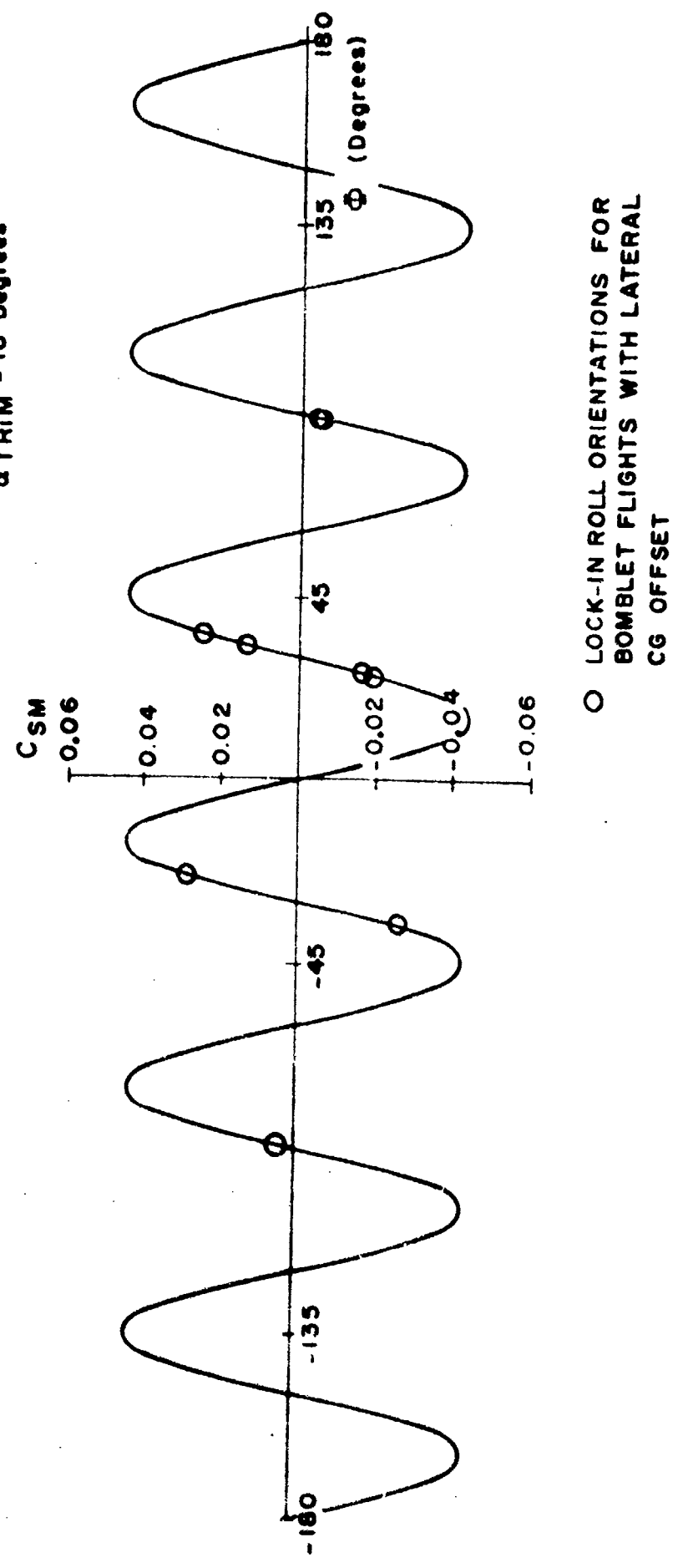


Figure 11. Effect of Side Moment on Roll Lock-In

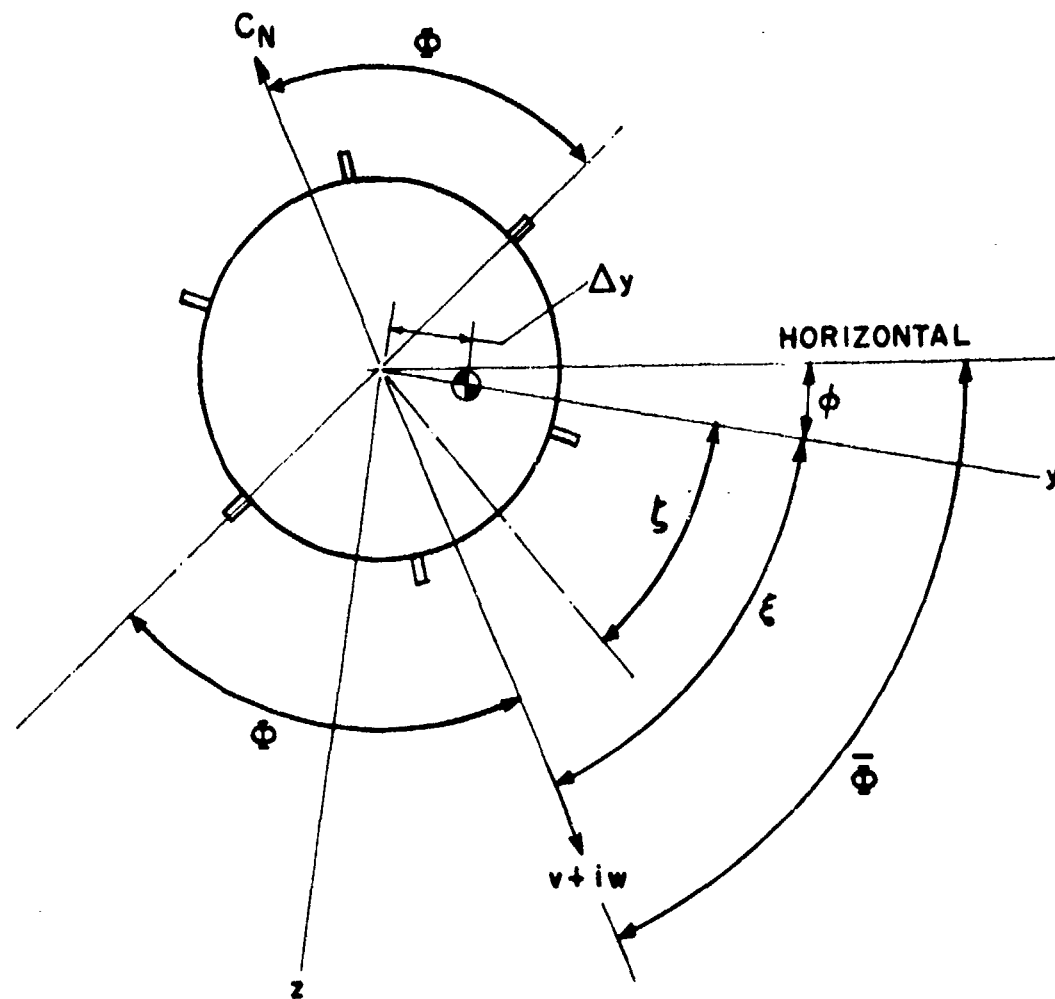


Figure 12. Definition of Angles and Axes Used in Describing Bomblet Roll Dynamics

The roll rate (and also the coning rate) will obviously depend upon both the roll driving torques and roll damping, although the direction of roll will in many instances be determined by the roll torque due to cg offset, because it will often be larger than the fin cant and fin induced aerodynamic roll moments.

Detailed examination of 6-DOF motion histories for a series of runs where the standard deviation of Δy was 0.008 inch, showed that for all the runs where lock-in occurred, the terminal spin rate was of the same sign and approximately proportional to the induced roll moment resulting from the cg lateral offset.

The effect of cg lateral offset on the dispersion is shown in Figure 13. The data were obtained from 6-DOF trajectory calculations with and without cg offset, and show the increase or decrease in radial dispersion

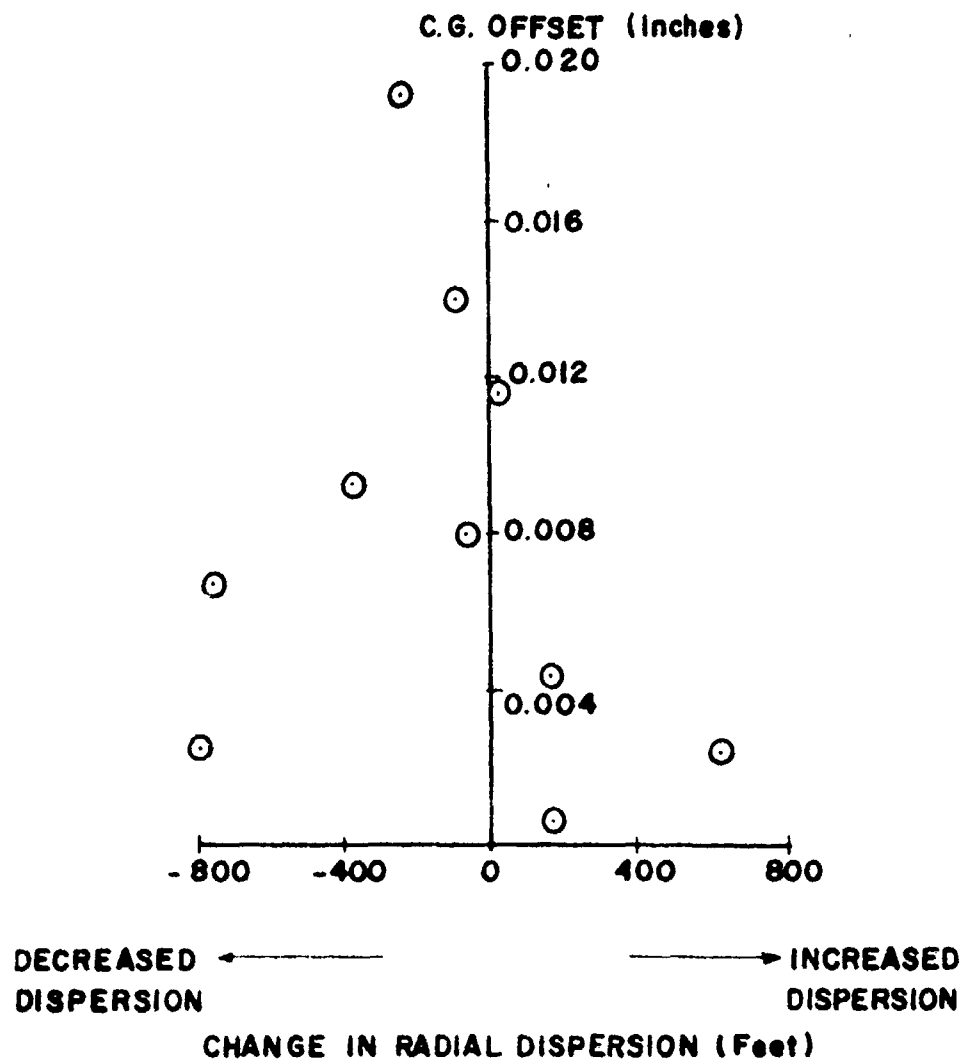


Figure 13. Effect of CG Lateral Offset on Radial Dispersion

as a function of cg lateral offset. As can be seen, the dispersion data tend to be erratic because of the incremental changes in the roll lock-in angle and roll rate. It is also noteworthy that a cg offset of only 0.002 inch has a large effect on the dispersion.

Effect of Fin Cant For large cg offsets, the preceding indicates that large roll and coning rates can be anticipated, as long as lock-in occurs. An obvious approach to the prevention of lock-in is the use of large intentional fin cant, such that the effects of cg offset and the side moment are overcome.

A preliminary evaluation was made using a cant angle of 0.5 degree and a standard deviation of cg lateral offset of 0.008 inch. For a trim angle of attack of 10 degrees and a cg offset of 0.008 inch, the maximum roll torque due to cg offset is approximately the same as that due to cant.

Out of 10 flight simulations only one lock-in condition was noted. Figure 14 compares the roll rates and angle of attack plane histories for two bomblet flights differing only in the cant angle and cg offset. The angle of attack plane rotation (coning) is significantly reduced with the intentional fin cant, even though the roll rate is greatly increased.

The effectiveness of intentional fin cant has also been proven from large Monte Carlo samples where, in addition to cg lateral offset, lateral misalignment and nose-roughness asymmetry were also present.

It should be mentioned that the effectiveness of intentional fin cant is due in part to the relatively small spin dependent magnus moment. This allows the roll rate to be increased to moderate values without adverse magnus effect on the coning motion.

The maximum cant angle is established either by magnus considerations or by the possibility of the configuration becoming gyroscopically stable. The cant angle required for gyroscopic stability decreases very rapidly as the bomblet fineness ratio is decreased, due both to the decrease in the ratio of the transverse to axial moment of inertia and the reduction in unstable pitching moment derivative at zero angle of attack.

D. DISPERSION PREDICTION - GENERAL CONSIDERATIONS

It is difficult to assess the impact dispersion characteristics of the S-Curve type bomblet without consideration of the exact bomblet motion. This is due to the fact that the aerodynamic lift force (which provides the dispersion) is constantly changing in magnitude and direction as a result of the bomblet dynamics. The dynamics of the S-Curve type bomblet, in turn, are highly sensitive to the initial flight conditions and bomblet configurational asymmetries.

For these reasons the trajectory calculations have been formulated so as to provide the closest possible duplication of actual bomblet flight. This has necessitated that the initial flight conditions at dispenser opening and during cluster break-up be realistically simulated, and that bomblet configurational asymmetries be introduced which are representative of actual production ordnance.

In contrast, a simplified treatment of the bomblet dispersion based on constant trim angle of attack and no angular motion, would not only over-predict the dispersion but would not provide an impact pattern distribution. Subsequently, poor agreement between the simulations and flight results would be expected.

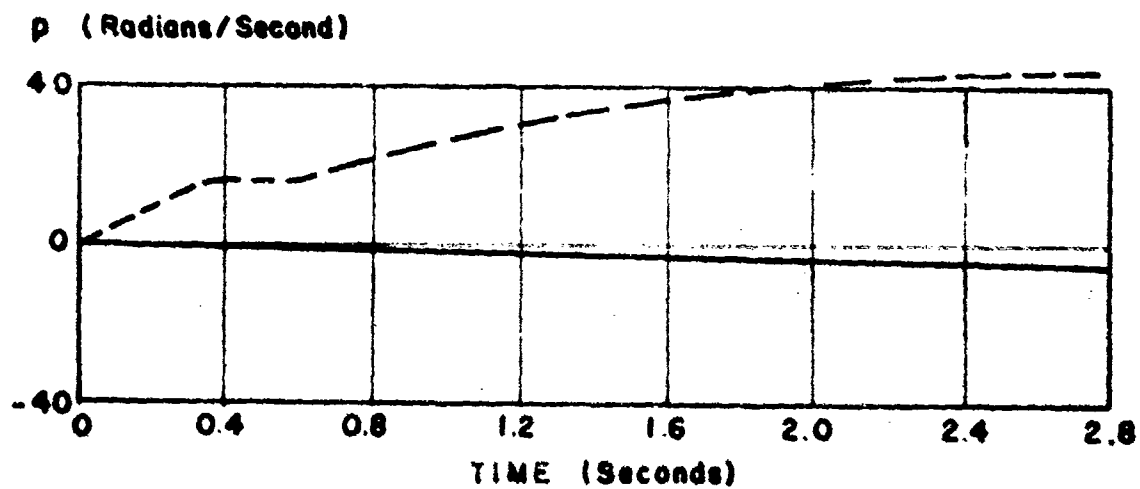
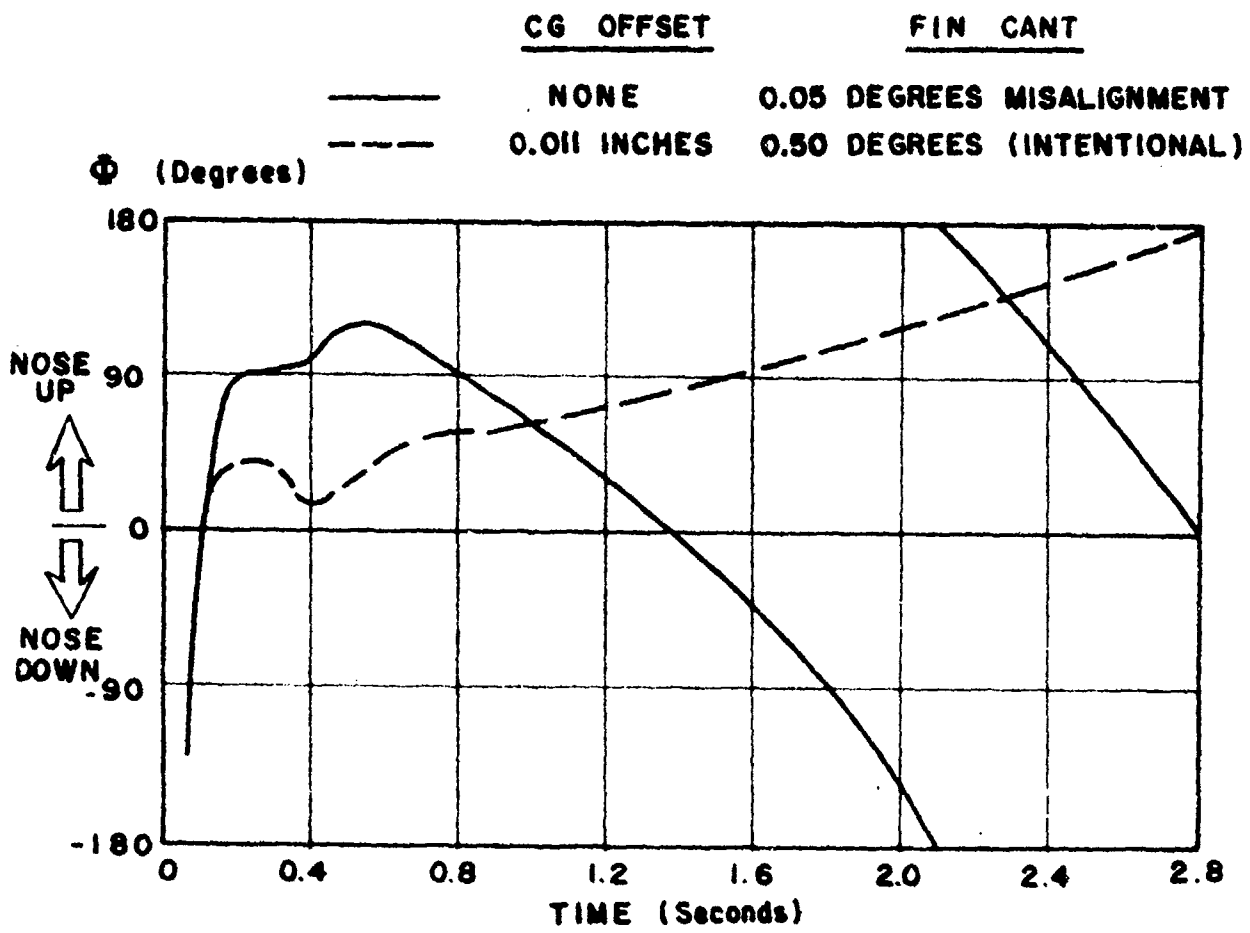


Figure 14. Effect of Intentional Fin Cant on the Motion of an S-Curve Bomblet with Lateral CG Offset

Monte Carlo Method To the maximum practicable extent, the performance of the S-Curve bomblet has been investigated using the Monte Carlo method, taking into account both the randomness of the initial flight conditions and the configurational asymmetries. The Monte Carlo technique and its adaptation to the simulation of bomblet cluster break-up and configurational asymmetries is described in Section IV. Except for center-of-gravity lateral offset, parametric analyses (with one or more fixed values of each parameter) have been avoided, since results obtained in this way can be misleading unless a sufficient range of all variables is investigated. The limitation of the parametric type of analysis is simply a result of the fact that nearly all of the parameter responses are nonlinear. This precludes any generalization of the results or the use of linear superposition as a means of determining the combined effect of a large number of parameters. Although parametric analysis is widely used in the determination of the dispersion of conventional bombs, projectiles, and missiles, it is not appropriate for self-dispersing ordnance.

E. MONTE CARLO IMPACT PATTERNS

Except where noted, dispersion data have been computed for bomb-lets of standardized size, weight, and inertia. The standardized physical characteristics data are summarized in Table III. Also, emphasis has been placed on three dispenser event conditions, corresponding to dispenser or warhead function at high subsonic, transonic, and supersonic Mach numbers, respectively. The high subsonic event condition is defined as the basic event condition, and is identical to that considered for the original S-Curve dispersion studies (Reference 1). The transonic event conditions are representative of those for a prototype guided dispenser, while the supersonic event conditions are based on the flight characteristics of a surface-to-surface tactical missile warhead.

| TABLE III. PHYSICAL CHARACTERISTICS DATA FOR STANDARD SIZE S-CURVE BOMBLET | |
|--|---|
| Length | 8 inches |
| Diameter | 2 inches |
| Aerodynamic Reference Area | 0.0218 ft ² |
| Aerodynamic Reference Length | 0.167 feet |
| Weight | 1.51 pounds |
| Axial Moment of Inertia, I_x | 1.629×10^{-4} slug-ft ² |
| Transverse Moment of Inertia, I | 1.06×10^{-4} slug-ft ² |

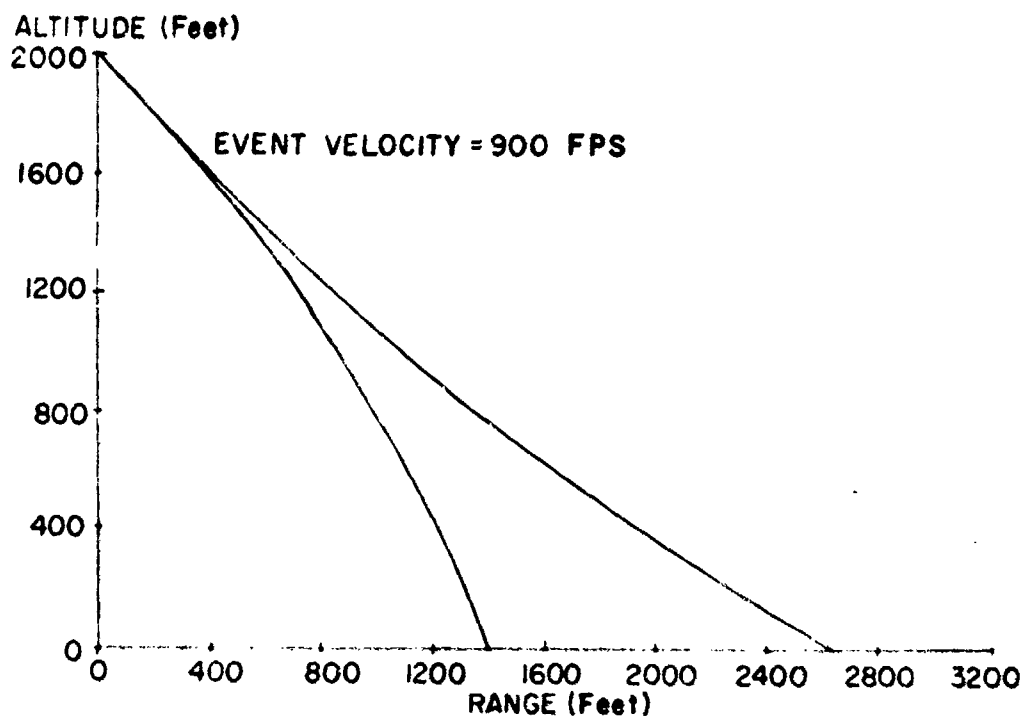
Except where noted, the bomblet initial motion perturbations at cluster break-out and the bomblet configurational asymmetries correspond to the values described in Section IV of this report.

Impact Dispersion Pattern - Basic Event Condition Figure 15 shows the computed Monte Carlo impact pattern data for the basic high-subsonic event condition, with 2000 feet height-of-burst (HOB). The pattern is computed for the cylindrical afterbody bomblet configuration B₅N₅Z₁A₅F₅, with the center-of-gravity positioned for a nominal subsonic trim angle of attack of 10 degrees. The impact pattern is a composite of two separate simulations. The open symbols represent a Monte Carlo simulation of 100 runs in which the cg lateral offset was neglected, but all other configuration asymmetries were included. The solid symbols represent a simulation of 70 runs with a standard deviation of cg lateral offset of 0.0016 inch. In the latter series the fin cant was identically zero. The standard deviation values of cross-range dispersion are within two percent for the two groups, while the standard deviation values of range dispersion are within ten percent for the two groups. Thus, small values of cg lateral offset do not significantly affect the impact pattern, even though the effect on individual trajectories may be large.

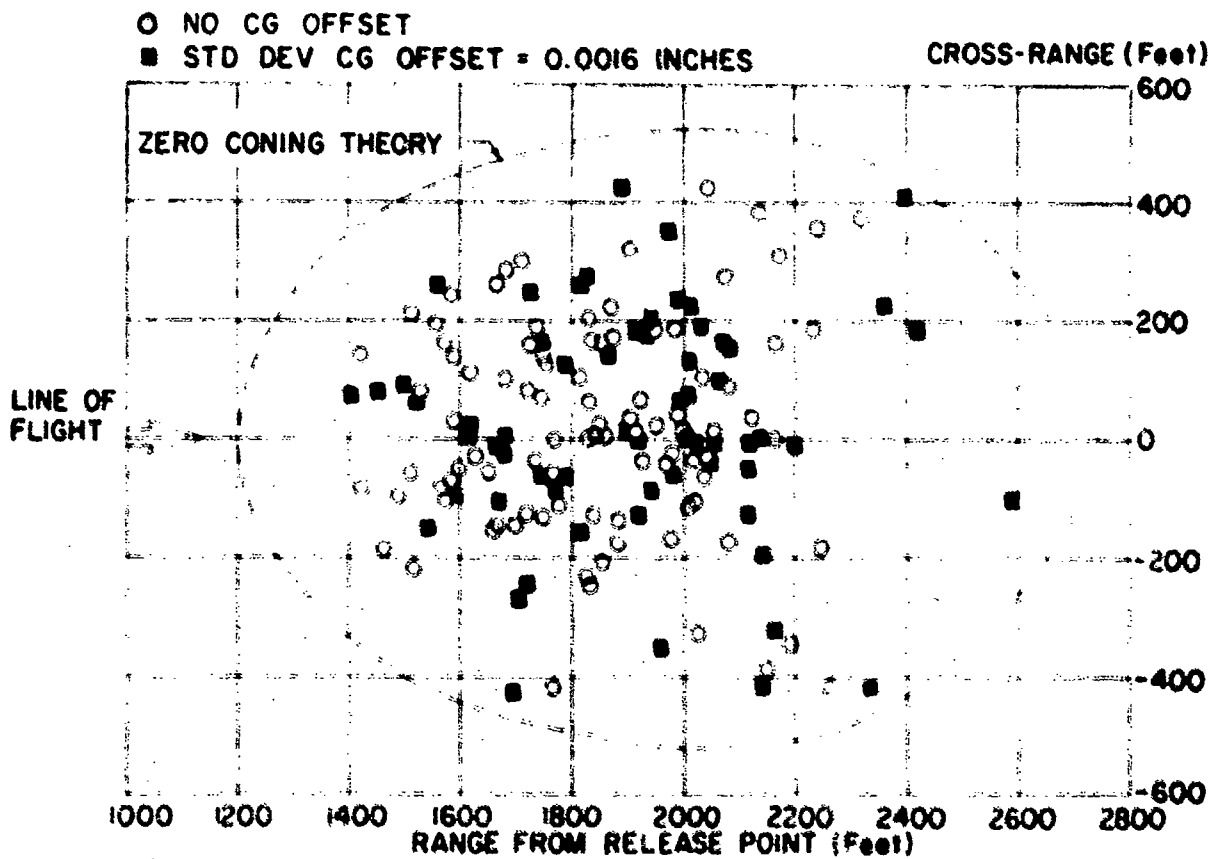
The overall pattern length is seen to be about 1000 feet, while the overall pattern width is about 800 feet. For the combined patterns, the standard deviations of range and cross-range dispersion with respect to the mean center of impact are 231 and 183 feet, respectively. This shows that the impact points tend to have greater concentration toward the center of the pattern. Figure 16 shows the cumulative probability distributions for the first group. The distribution of impact points is piecewise normal,³ emphasizing the fact that the impact dispersion characteristics are the result of nonlinear interactions between the dispersion parameters.

Comparison with Zero Coning Solutions It is of interest to compare the Monte Carlo results with a pattern prediction based on zero coning. For the basic event condition, a series of zero coning trajectories were computed with the initial orientation of the angle of attack plane as a parameter. The initial angle of attack was in all cases assumed to be 5 degrees (nose outward from the line of flight) and cluster break-up was assumed to occur instantaneously at an altitude 200 feet below the dispenser HOB. This point represents approximately the lowest cluster break-out point in the Monte Carlo simulations. The locus of impact points computed in this manner is shown superimposed on the Monte Carlo pattern of Figure 16.

³ The normal distribution appears as a straight line on the probability graph.



a) Typical Trajectories



b) Impact Pattern

Figure 15. Monte Carlo Impact Pattern Prediction for S-Curve
Bumblot - High-Subsonic Event Condition

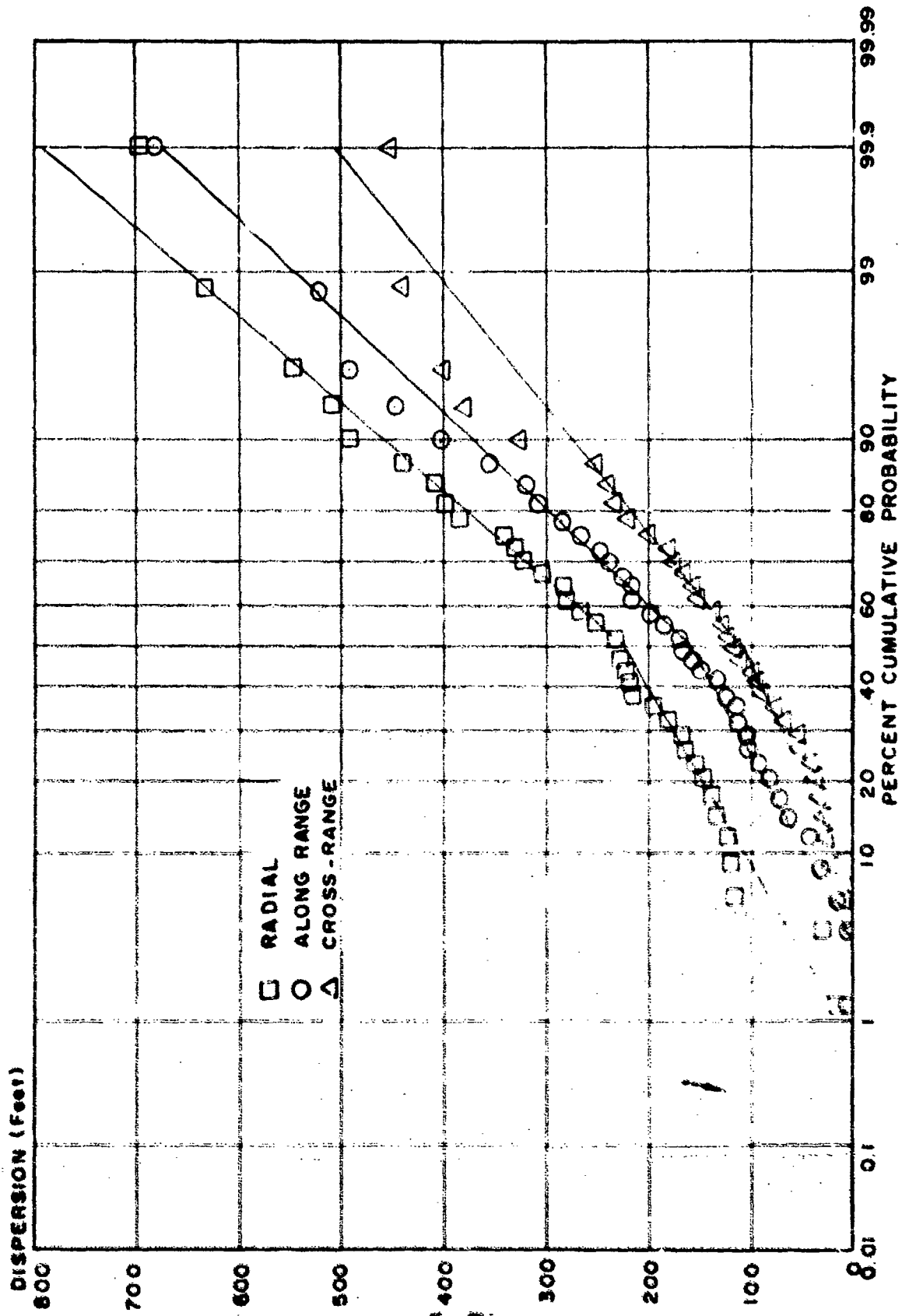


Figure 14. Probability Distribution for 5-Curve Bumble Impact Dispersion Pattern

It is apparent that the simplified theory overpredicts the Monte Carlo dispersion pattern; however, the maximum dispersion values computed in the Monte Carlo simulations closely approach the zero coning boundary.

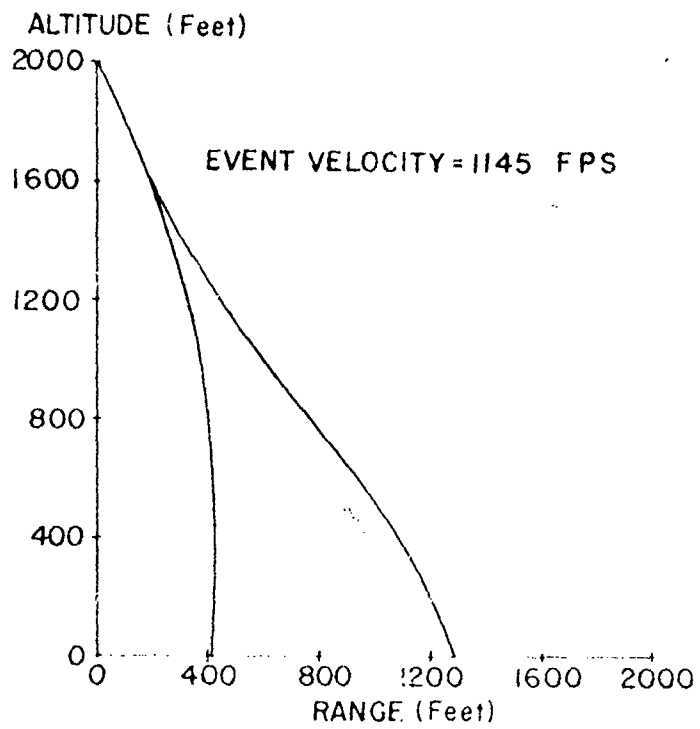
Transonic and Supersonic Delivery Monte Carlo dispersion data for the transonic dispenser event condition were computed for the basic boattail-afterbody bomblet, because this configuration has much better trim characteristics through the transonic range. Preliminary pattern size predictions based on zero coning showed that the boattail bomblet would have about twice the dispersion of the cylindrical afterbody bomblet. The cluster-breakout perturbations and configurational asymmetries correspond to the data of Section IV, except that cg lateral offset is neglected.

Figure 17 shows the computed impact pattern for the transonic dispenser event conditions with HOB of 2000 feet. The standard deviations of cross-range and range dispersion with respect to the mean center of impact are within ten percent of those for the subsonic event condition.

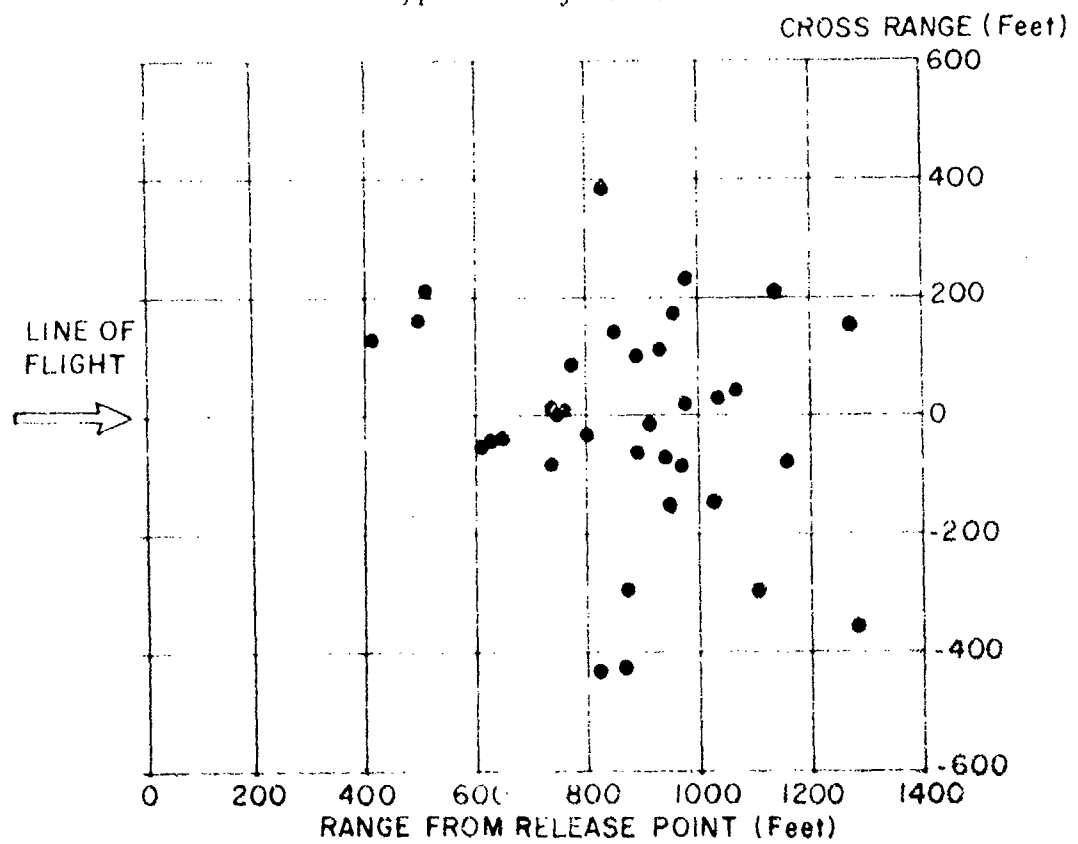
For the supersonic event ($V_E = 2000$ fps) the boattail configuration was again selected. The impact pattern data are shown in Figure 18. The results show a very large increase in the area coverage, with a few bomb-lets impacting several thousand feet forward of the mean center of impact. Thus, it is evident that the large dynamic pressure can be exploited for increased dispersion, notwithstanding the proportionately larger terminal spin rates and tendencies for coning motion.

Table IV summarizes the statistical dispersion data for the subsonic, transonic, and supersonic event conditions which have been evaluated. It will be noted that the standard deviation values of the range and cross-range dispersion for the supersonic event condition are greater than the subsonic and transonic values by factors of about four and two, respectively. Obviously, this larger dispersion can also be exploited by a decrease in the HOB.

Effect of Static Unbalance The static unbalance (lateral center-of-gravity offset) of a bomblet configuration can be expected to vary widely depending upon the method of manufacture and assembly. Using the subsonic event condition, separate Monte Carlo impact pattern simulations were accomplished for the following values of static unbalance: 0, 0.0016, 0.0080, and 0.0400 inch. The initial motion perturbations and lateral misalignment remained identical to those used for the previously described simulations. A minimum of 70 trajectories was computed for each simulation. For these simulations the fin cant was assumed to be identically zero. The results of the simulations are summarized in Figure 19, which is a plot of both the maximum dispersion and the standard deviation of dispersion versus the cg lateral offset parameter. The results show that cg offsets greater than 0.001 inch have a measurable effect on the dispersion

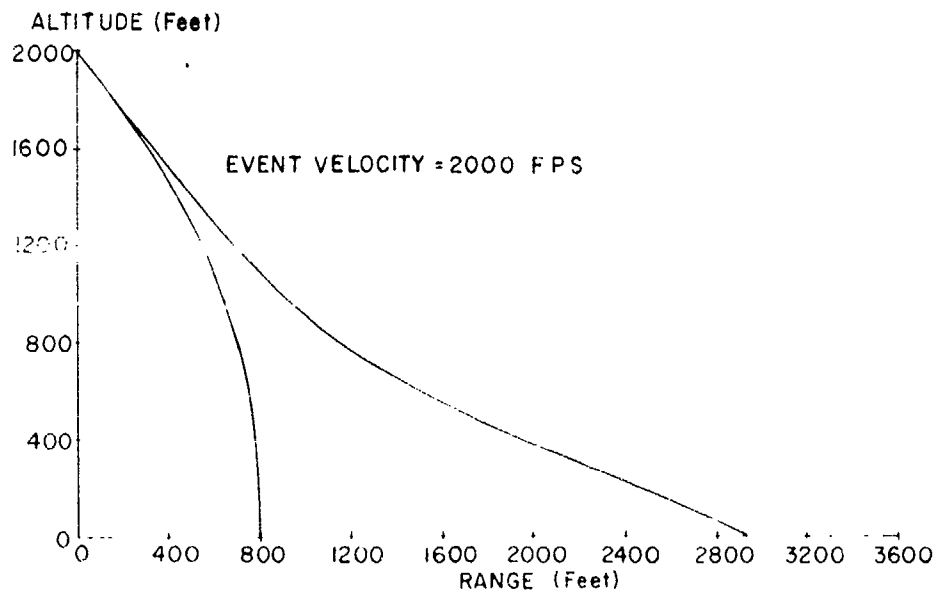


a) Typical Trajectories

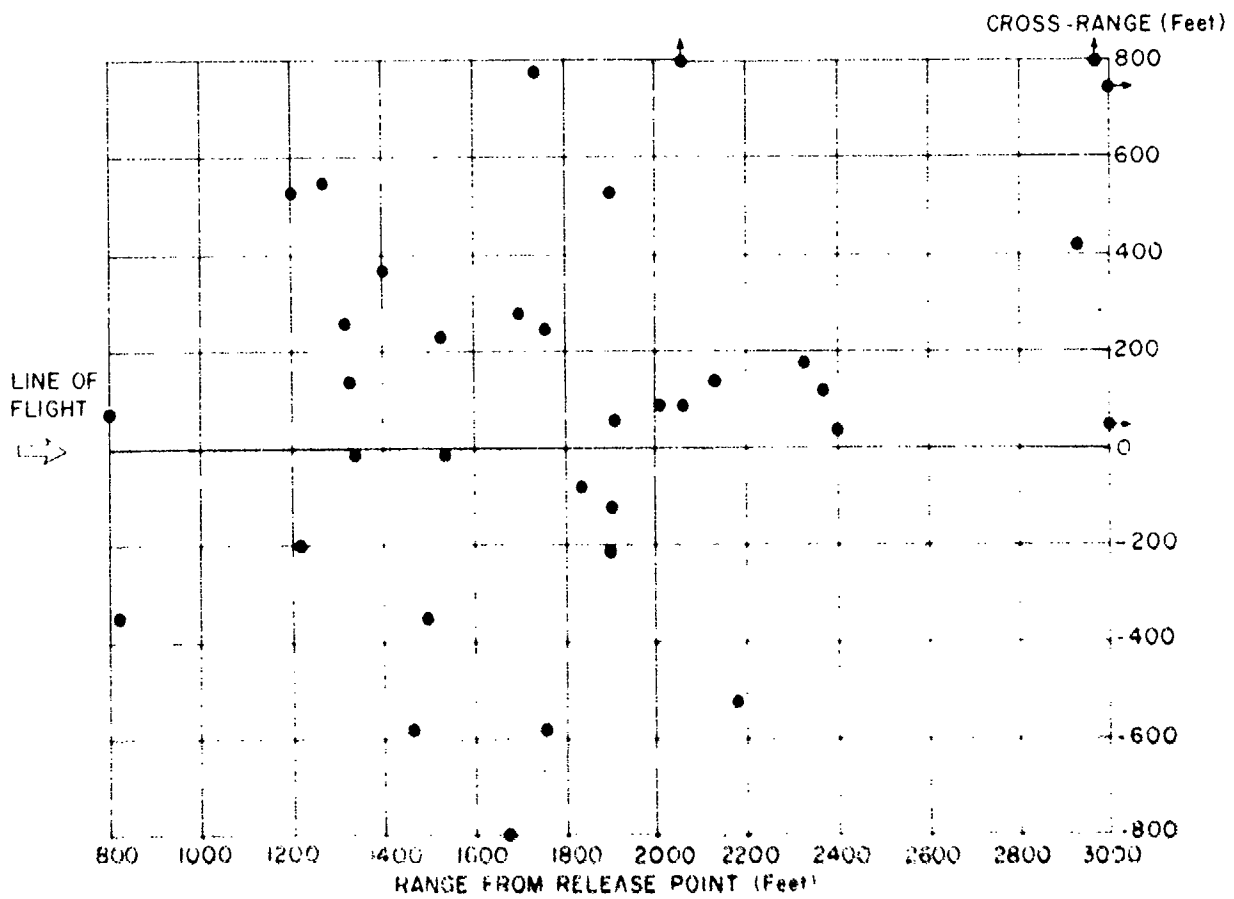


b) Impact Pattern

Figure 17. Monte Carlo Impact Pattern Prediction for S-Curve Bomblet - Transonic Event Condition



a) Typical Trajectories



b) Impact Pattern

Figure 18. Monte Carlo Impact Pattern Prediction for S-Curve Bomblet - Supersonic Event Condition

TABLE IV. COMPARISON OF IMPACT DISPERSION DATA FOR
SUBSONIC, TRANSONIC, AND SUPERSONIC EVENT CONDITIONS

| Event Conditions | Mean Range X (Feet) | Mean Cross-Range Y (Feet) | Standard Deviation Range σ_X (Feet) | Standard Deviation Cross-Range σ_Y (Feet) |
|---|------------------------------|------------------------------------|--|--|
| <u>Subsonic Event</u> $V_E = 900$ fps $\gamma_E = 45^\circ$ | 1853 | -17 | 221 | 181 |
| <u>Transonic Event</u> $V_E = 1145$ fps $\gamma_E = 65.7^\circ$ | 875 | 11 | 202 | 183 |
| <u>Supersonic Event</u> $V_E = 2000$ fps $\gamma_E = 50^\circ$ | 1978 | -139 | 959 | 470 |

Note: 1) HOB = 2000 feet.

2) Configuration $B_S N_{S2} A_{S1} F_{S2}$ for subsonic event.

Configuration $B_S N_{S1} A_{S2} F_{S3}$ for transonic and supersonic events.

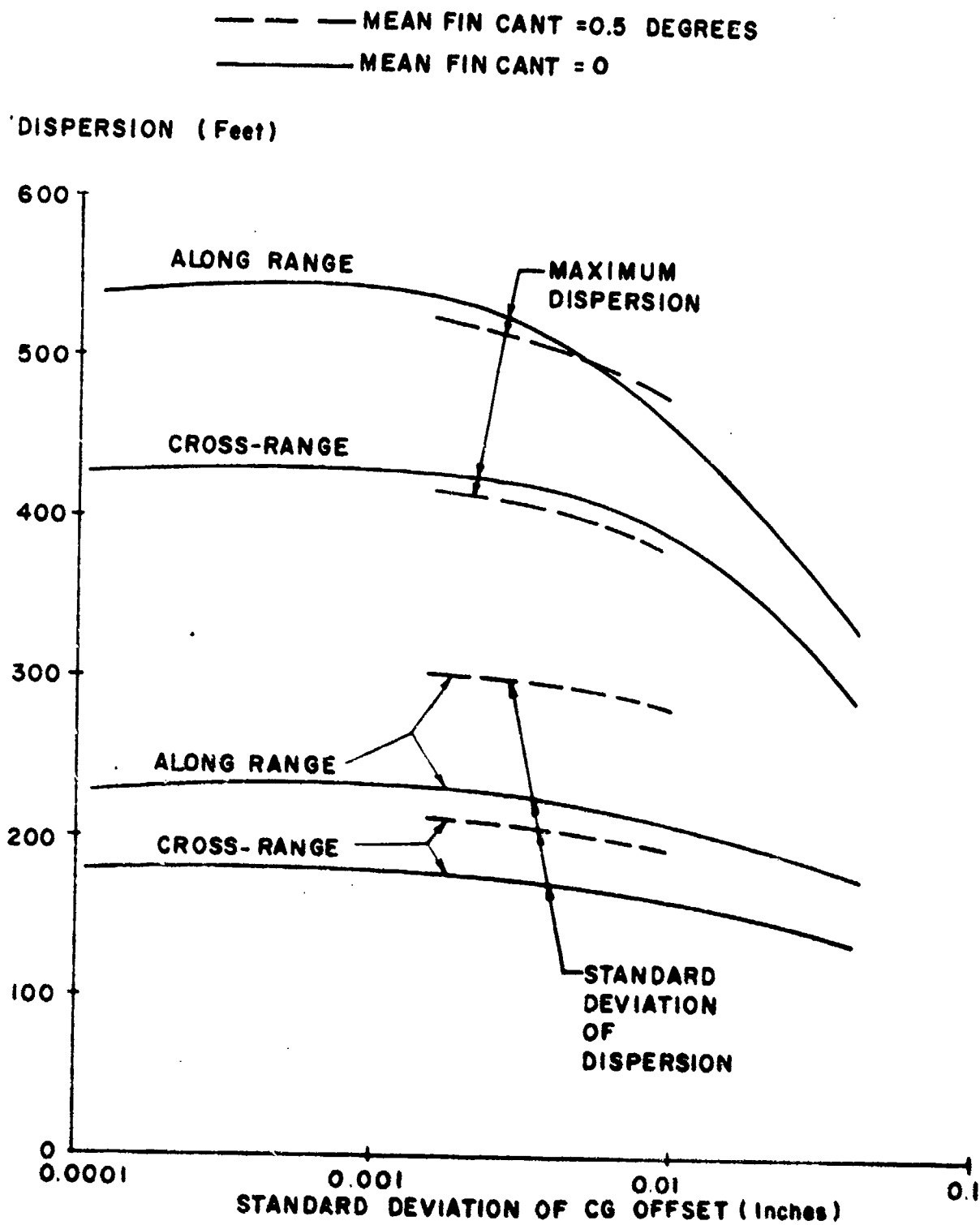


Figure 19. Variation of Impact Dispersion with C.G. Lateral Offset

and that for cg offsets greater than 0.01 inch a very large decrease in both the maximum and standard deviation of dispersion can be expected.

Effect of Fin Cant Some of the preceding simulations were repeated using intentional values of fin cant of 0.1, 0.5, and 2.5 degrees. The 0.5 degree cant angle was found to significantly increase the dispersion for cg lateral offsets of 0.0016 and 0.0080 inch, and the results are superimposed on the zero cant data in Figure 19. The 0.1 degree cant angle was found to be insufficient to prevent roll lock-in even for a cg offset of 0.0016 inch, and out of 35 trajectories, 21 developed a roll lock-in type motion with ϕ constant. The 2.5 degree cant angle, which was investigated in conjunction with the 0.0400 inch cg offset, did not improve the dispersion. This was due both to the increased magnus moment and the tendency toward spin stabilization.

It should be emphasized that a finite trim angle of attack due to the S-shaped moment curve will exist only if the configuration is gyroscopically unstable. The cant angle required for gyroscopic stability at zero angle of attack is only 3.0 degrees at Mach number 0.5. Because of the nonlinearity of the moment curves, the non-rolling trim is reduced by cant angles less than 3.0 degrees.

Effect of Initial Pitch Disturbance For the basic Monte Carlo simulations an initial pitch rate at cluster break-out was introduced such that the magnitude of the first peak in the angle of attack oscillation had a 2 σ value of about 45 degrees. For a 900 fps event velocity, the corresponding standard deviation for the pitch rate was estimated to be about 35 radians/second. Statistical analysis of 30 Monte Carlo simulations computed with a standard deviation of initial pitch rate equal to 35 radians/second showed that the maximum angle of attack was 52 degrees and that the mean value of the first oscillation peak was 30 degrees. A second Monte Carlo simulation was accomplished with twice the pitch rate at cluster break-out. Again, from analysis of 30 trajectories, the maximum angle of attack was found to be 92 degrees, while the mean value of the first oscillation peak was increased to 46 degrees with a standard deviation of 21 degrees.

The effect of the increased pitch rate on the impact dispersion was surprisingly small; the standard deviation of cross-range dispersion was decreased about 20 percent, while the standard deviation of range dispersion was actually increased about 5 percent.

Effect of Increased Trim Angle of Attack The impact patterns shown in Figures 15, 17, and 18 are based on bomblet configurations which have a nominal trim angle of attack of approximately 10 degrees at low subsonic velocities. This trim angle was selected conservatively, so as to avoid possible anomalous bomblet motions due to the highly nonlinear induced aerodynamic moments at large angles of attack. To determine the

significance of these nonlinearities at large angles of attack, the nominal trim angle of attack of the cylindrical-afterbody bomblet was increased to 16 degrees, and a new Monte Carlo simulation accomplished. The impact patterns are compared in Figure 20. For the large trim angle, the standard deviation values of range and cross-range dispersion are increased by factors of 1.67 and 2.20, respectively. These compare to a factor of 1.72 for the bomblet normal force increase at the larger trim angle.

Effect of Bomblet Mass Density While the S-Curve bomblet dispersion is essentially proportional to the lift/weight ratio, the effect of the bomblet mass and inertia is also felt through the pitch and roll dynamics. To determine more exactly the relationship between the dispersion and the bomblet mass density, Monte Carlo simulations were accomplished for two bomblet configurations differing only in mass density. The heavy bomblet was assumed to have twice the mass density of the standard bomblet. For these simulations the boattail bomblet configuration was assumed, with the nominal trim angle of attack adjusted to sixteen degrees. The basic subsonic event condition was selected for the analysis.

The computed impact patterns (based on 30 trajectories each) were statistically analyzed and it was found that the standard deviations of range and cross-range dispersion for the heavy bomblet were 47 percent of those for the reference bomblet; in other words, the dispersion was approximately proportional to the reciprocal of the mass ratio.

The results show that the effects of mass on the flight time and flight velocity tend to be compensatory insofar as the dispersion is concerned. Also, the dispersion is apparently not very sensitive to changes in the roll and pitch dynamics resulting from the increased moments of inertia.

Effect of Nose-Roughness Asymmetry The effect which nose-roughness asymmetry can have on the aerodynamic characteristics of an S-Curve type bomblet is described in Section II-B. To determine the effect of nose-roughness type asymmetry on the dispersion, Monte Carlo simulations were accomplished for the cylindrical-afterbody bomblet configuration using the basic subsonic event conditions. The standard deviation values for cant and lateral misalignment were identical to those derived in Section IV, while the standard deviation of cg lateral offset was assumed to be 0.0016 inch.

For the first Monte Carlo simulation the mean fin cant was set to zero. The impact data, in the case of zero mean cant, showed a 40 percent reduction in the standard deviation values of range and cross-range, when comparison was made with the impact pattern data computed without nose-roughness asymmetry. Detailed examination of the bomblet motion histories showed that periods of roll lock-up and erratic pitching motion were encountered.

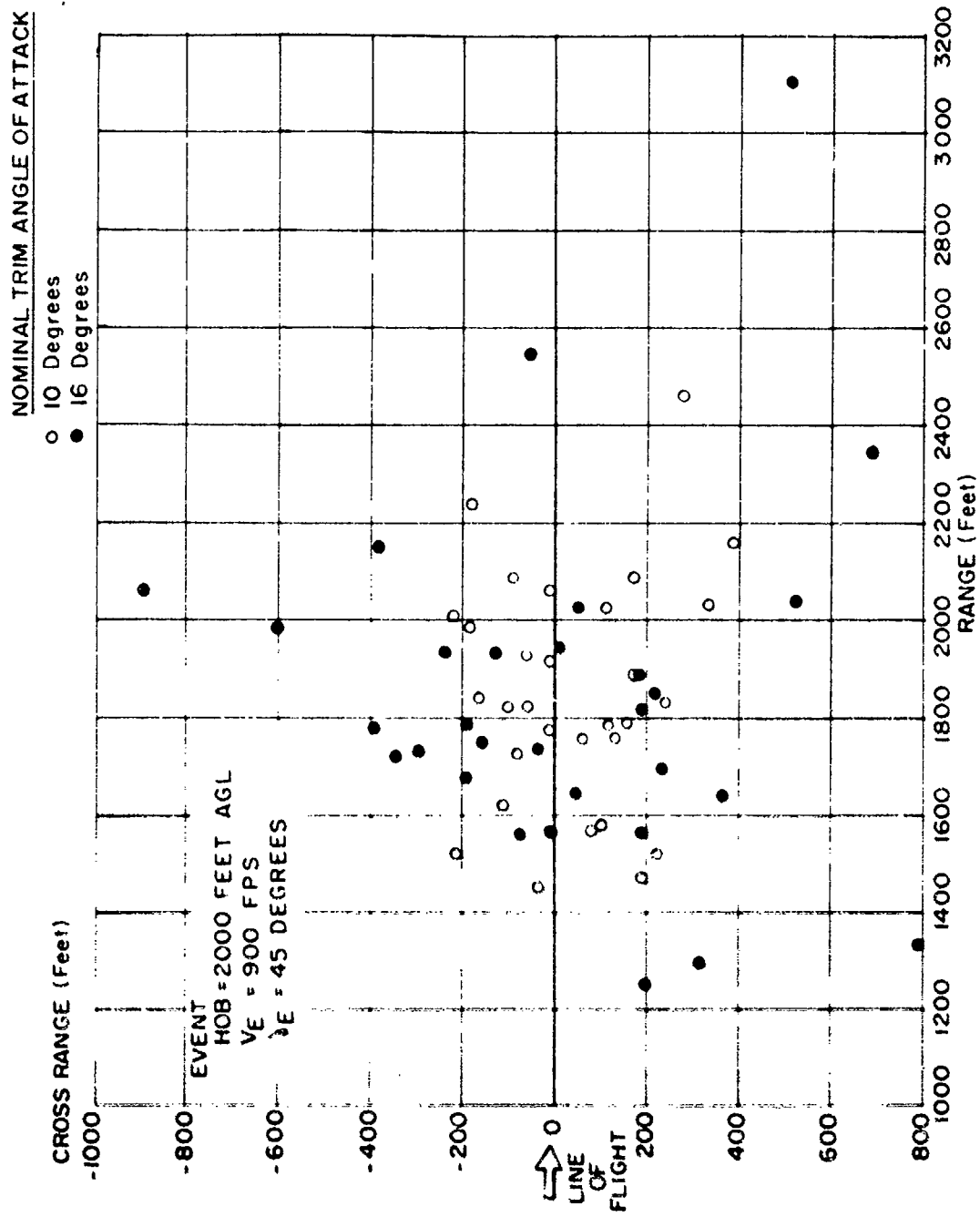


Figure 20. Effect of S-Curve Bomblet Trim Angle of Attack on Monte Carlo Impact Pattern for Standard Subsonic Event Condition

The Monte Carlo simulation was repeated with a mean fin cant angle of 0.5 degree. With intentional fin cant the reduction in the standard deviation of cross-range dispersion was only 3 percent while the reduction in range dispersion was but 15 percent.

Thus, nose-roughness asymmetry should not be of great concern if intentional fin cant is utilized.

F. SPECIAL STUDIES - HIGH DRAG AND DUAL MODE BOMBLETS

For certain bomblet warheads, a near-vertical flight path at impact is desirable as a means of achieving optimum weapon effectiveness.

High-Drag Bomblet A brief investigation was made to determine the effect of drag on the flight characteristics of a typical S-Curve bomblet. The high-drag configuration was assumed to have a two-caliber attached-inflatable-decelerator (AID), which would be configured such that the bomblet would retain an S-curve pitching moment. The modified configuration was assumed to have the same lift and trim characteristics as the basic cylindrical afterbody bomblet, but the subsonic drag coefficient was increased by an order of magnitude.

Figure 21 compares the planar trajectory and range dispersion for the basic and high-drag configurations, based on the representative subsonic dispenser event condition. Bomblet orientation for maximum dispersion is assumed. The trajectory data show that a large amount of dispersion is lost due to the higher drag, even though the flight time is increased.

The increased drag was effective in increasing the maximum flight path angle at impact from 65 to 81 degrees and the minimum flight path angle at impact from 10 degrees to 72 degrees.

Dual-Mode Bomblet The dual-mode S-Curve bomblet incorporates a drag device which can be deployed after a pre-selected time of flight. Dispersion is achieved during the first (lifting) flight phase; while the second (high-drag) flight phase is utilized for increasing the flight path angle at impact.

Trajectory and dispersion data for the dual-mode type S-Curve bomblet are compared with the standard S-Curve bomblet in Figure 22. Results for the dual-mode bomblet are shown for two different values of the drag coefficient for the high-drag phase. The smaller drag coefficient is representative of an AID configuration while the larger drag coefficient is representative of a small parachute.

Deployment of a drag device at about 2.0 seconds after event and at about 1000 feet above ground level significantly increases the impact flight

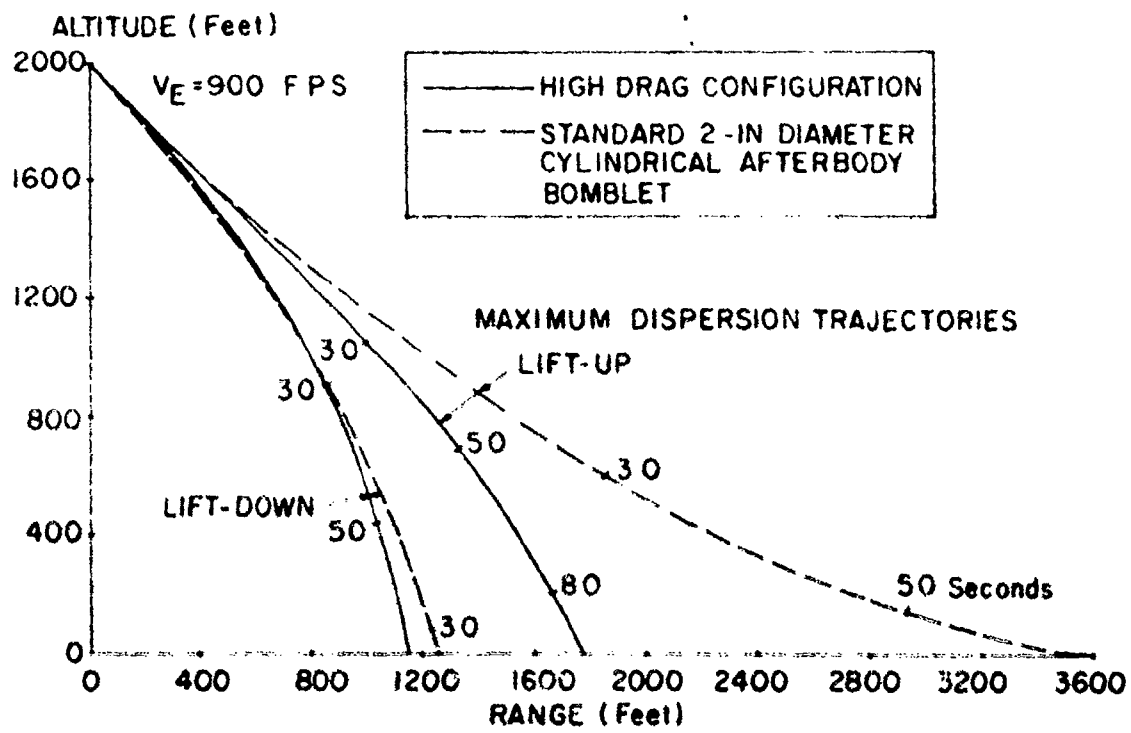
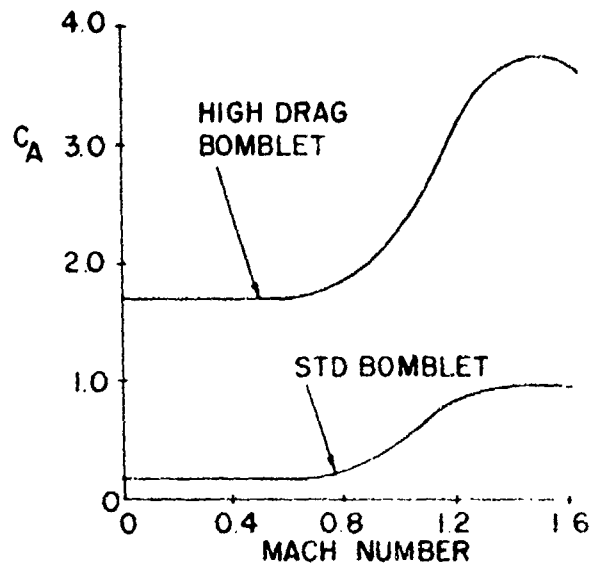


Figure 21. Trajectory Comparisons - Basic and High Drag S-Curve Bomblet Configurations - Standard Subsonic Event Condition

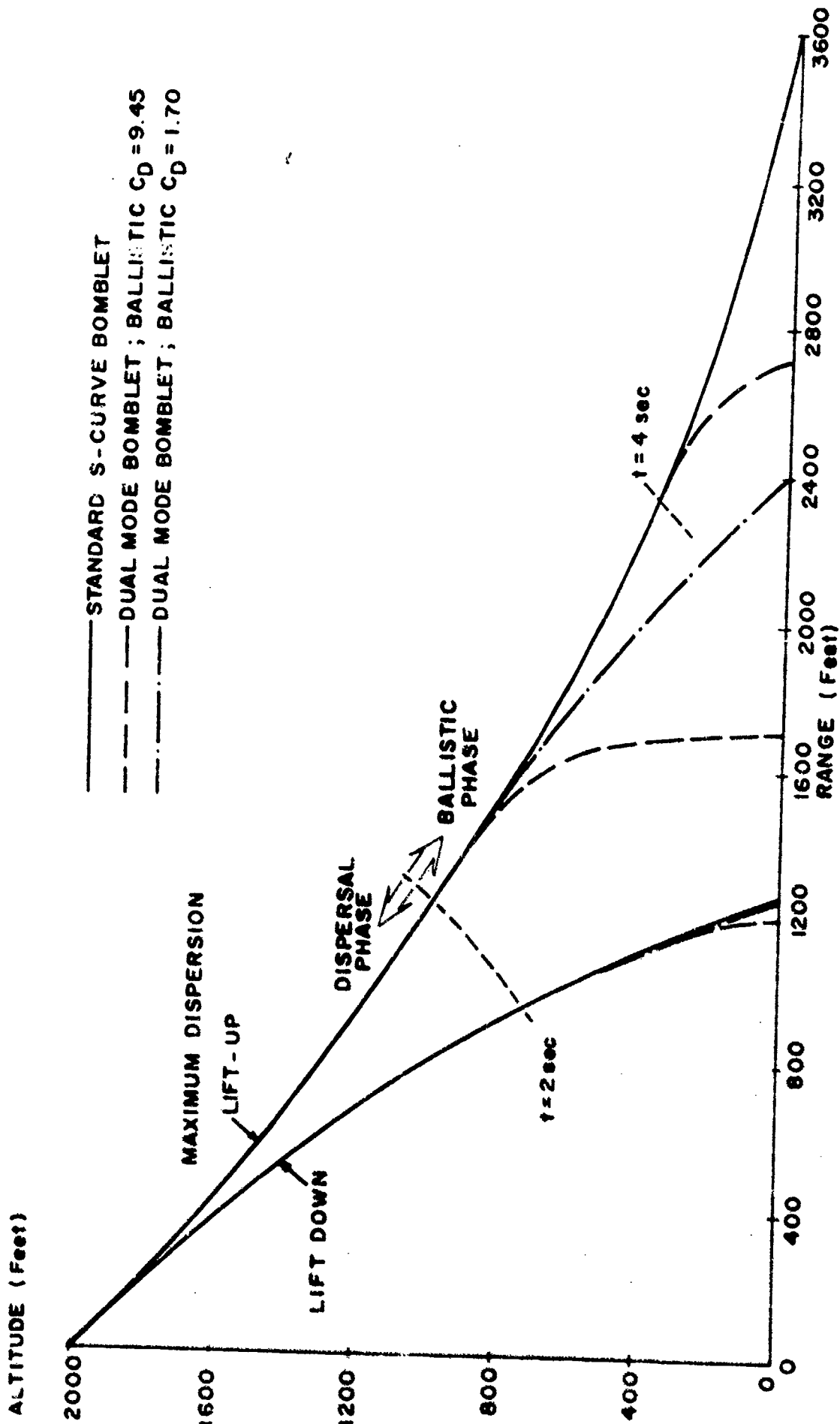


Figure 22. Trajectory Comparison - Basic and Dual Mode S-Curve Bomblet Configurations - Standard Subsonic Event Condition

path angle but, at the same time, cause a large loss in range dispersion, particularly for the parachute device.

To achieve both large dispersion and large impact flight path angles it is evident that decelerator deployment must be delayed. In fact, for the lift-down trajectories, it is not even necessary for the decelerator to deploy, since the impact flight path angles are large in any case. With the parachute-type decelerator deployed at 4.0 seconds the range dispersion is about 1500 feet while the impact flight path angle is of the order of 70 degrees for both the lift-up and lift-down cases.

G. ANALYSIS OF ALTERNATE S-CURVE CONFIGURATIONS

Many bluff-shaped bodies with low aspect ratio fins or subcaliber stabilizers can be made to have S-Curve moment characteristics with either small or no modifications.

Candidate S-Curve configurations of both low-fineness and high-fineness ratio can be selected with good lift-curve slopes. However, the after-body configuration is quite important and most boattail shapes, while having good moment characteristics, tend to experience a reduction in lift-curve slope.

A number of recent wind tunnel tests of bomb and bomblet models provide data on configurations which differ significantly from the two basic S-Curve bomblets analyzed in the present studies. References 6, 7, 8, 14, 17, and 18 present aerodynamic data on configurations with S-Curve moment characteristics, which may be useful in the development of alternate S-Curve configurations. Normal force slopes for a number of candidate S-Curve configurations are presented in Figure 23.

It is noteworthy that S-Curve versions of the APAM and BLU-87 bomblets, both possess poor lift curve slopes.⁴

Low-Fineness-Ratio Configurations Low fineness ratio bomblets are sometimes of interest because of warhead compatibility and dispenser-packaging considerations. The practicability of a low-fineness-ratio S-Curve bomblet has been reviewed and some 6-DOF motion simulations accomplished. Two aspects of the pitching moment behavior of low-fineness-ratio shapes are detrimental to good flight characteristics: first the low fineness ratio body has a small moment curve slope at zero angle of attack for trim angles less than about 20 degrees; secondly, these configurations

⁴ S-Curve type dispersion has been attempted with both the APAM and BLU-87 (References 6 and 19).

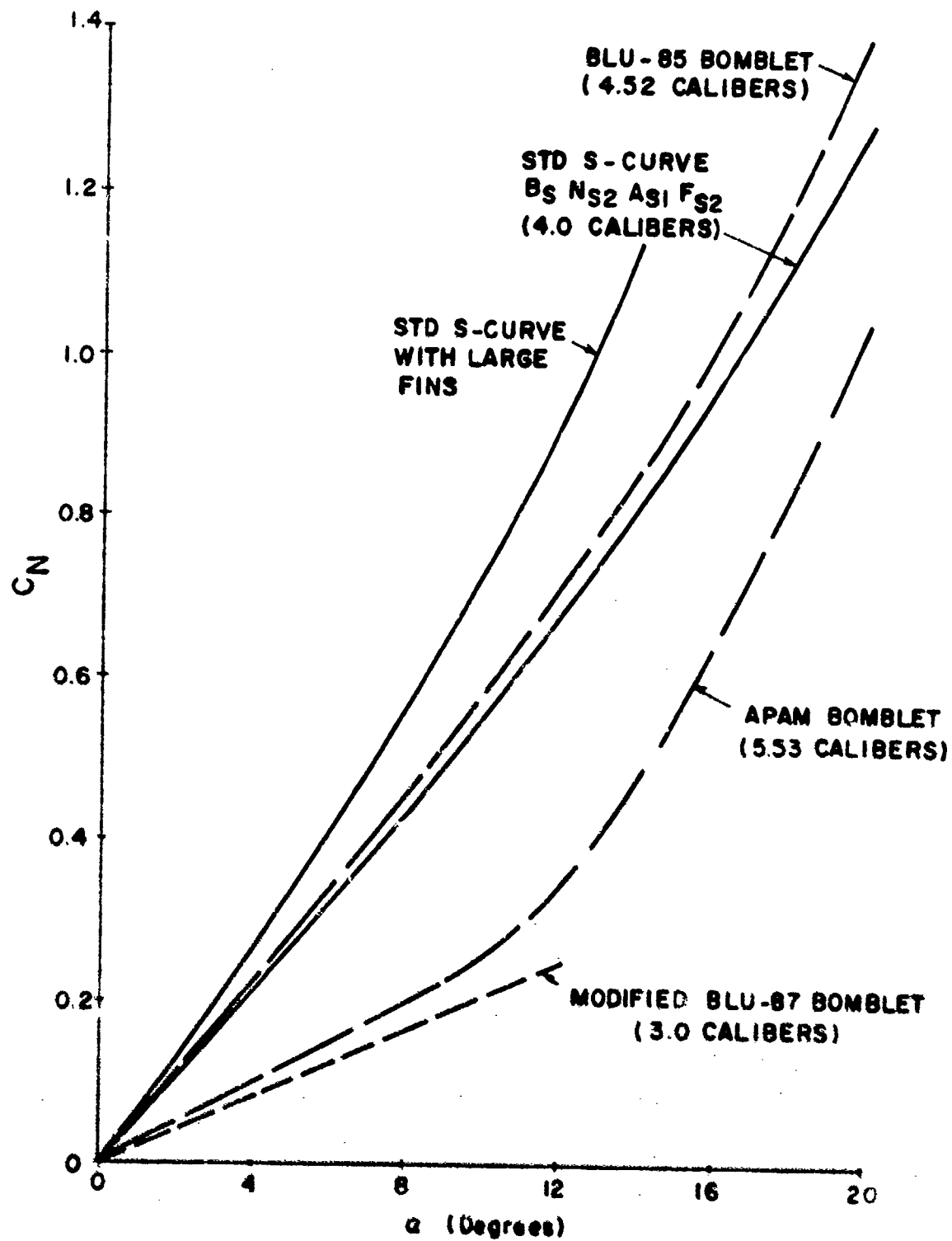


Figure 23. Normal Force Characteristics of Candidate S-Curve Bomblet Configurations

tend to have a rearward center of pressure shift at zero angle of attack with increasing Mach number, which in many instances makes the configuration stable at small angles of attack above the critical Mach number.

Although the dispersion performance of the low-fineness-ratio S-Curve configuration at subcritical Mach numbers appears promising under ideal conditions, the effects of unintentional roll and initial disturbances tend to greatly reduce the dispersion. One of the basic problems is that a low-fineness-ratio configuration becomes gyroscopically stable at small roll rates, as a result of both the reduction in the polar to transverse moments of inertia ratio and the reduction in the pitching moment derivative with decreasing fineness ratio. For a large diameter bomblet, which was investigated in detail, gyroscopic stability was achieved with a roll rate as small as 3 cps. Even at roll rates less than that required for gyroscopic stabilization, the gyroscopic precession resulting from roll and the out-of-trim pitching moment causes spiralling flight.

It is thus concluded that considerable effort would be required to develop a practicable low-fineness-ratio S-Curve bomblet, and, probably, severe restrictions would have to be imposed upon the release environment.

H. AIR-GUN LAUNCHED MODEL FREE-FLIGHT TESTS

Free-flight tests of the S-Curve-type bomblet were accomplished at test area B-82 at Eglin Air Force Base, Florida during October 1972. A 5.5-inch-bore air gun from the BARS test facility was used for launching the models at nominal velocities of 350 to 400 fps and at an initial flight path angle of 30 degrees. The first series of tests was accomplished with 3-inch-diameter S-Curve bomblet models of the cylindrical afterbody configuration B₅N₅₂A₅₁F₅₂. These models were launched singly at zero angle of attack. The 3-inch-diameter models were divided into two groups: the first group of 29 models was ballasted nose heavy for non-lifting ballistic flight, while the second group of 32 models had the center of gravity 1.5 calibers from the nose (corresponding to the basic S-Curve configuration). Five models of the second group incorporated intentional fin misalignment. The second series of tests utilized 1.5-inch-diameter models, which were launched in clusters of seven by the use of a special sabot. The second series of tests utilized 36 cylindrical afterbody bomblet models and 34 boattail afterbody bomblet models. Physical characteristics data for the flight-test models are summarized in Table V.

Velocity and attitude measurements for most of the tests were obtained from high-speed motion picture coverage of an 8-foot segment of the initial trajectory. For the standard 3-inch models, the mean launch velocity was determined to be 369 fps with a standard deviation of 10 fps. For the cluster rounds, the mean velocity was 360 fps with a standard deviation of 25 fps.

TABLE V. PHYSICAL CHARACTERISTICS DATA FOR S-CURVE FREE-FLIGHT-TEST MODELS

| Parameter | Configurations | | | |
|------------------------------------|-----------------------|----------|-------------------|--------------------|
| | Cylindrical Afterbody | | | Boattail Afterbody |
| | 3-Inch Diameter | | 1.5-Inch Diameter | 1.5-Inch Diameter |
| | Ballistic | Standard | Standard | Standard |
| Model length (Inches) | 12.0 | 12.0 | 6.0 | 6.0 |
| Weight (Pounds) | 5.13 | 5.13 | 1.04 | 1.04 |
| CG (Inches from nose) | 3.0 | 4.48 | 2.3 | 2.79 |
| CG (Calibers from nose) | 1.00 | 1.493 | 1.53 | 1.86 |
| Moments of Inertia | | | | |
| Polar (Slug-ft ²) | 0.00136 | 0.00133 | N/A | N/A |
| Transverse (Slug-ft ²) | 0.0105 | 0.00874 | N/A | N/A |

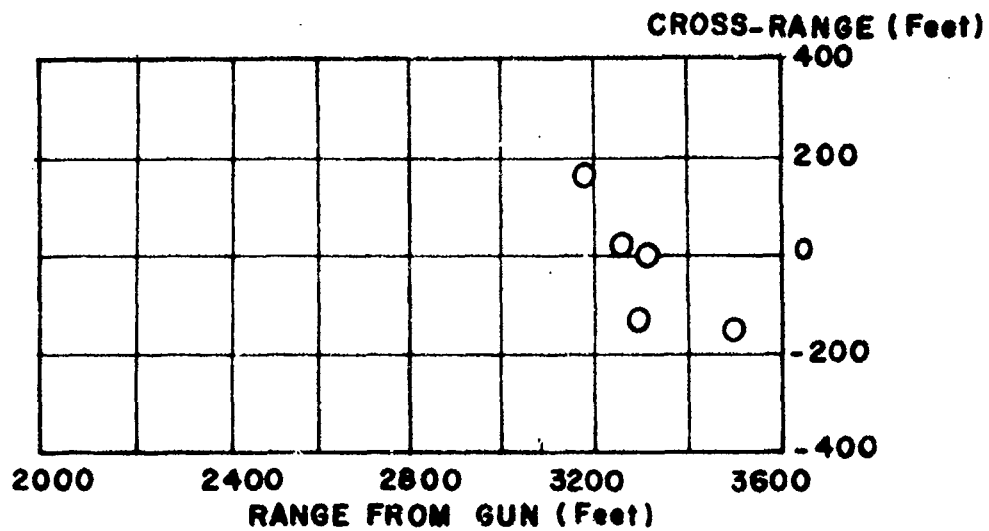
The lateral velocity perturbations for the standard 3-inch S-Curve models were of the order of 9 fps (standard deviation). Wind velocities during the tests were generally less than 5 mph and no wind corrections were applied to the test impact pattern data.

Impact Patterns Flight test impact patterns for the 3-inch diameter models are shown in Figures 24 and 25. Figure 24 depicts the impact pattern of the non-lifting ballistic models, while Figure 25 illustrates the impact pattern of the standard bomblet.

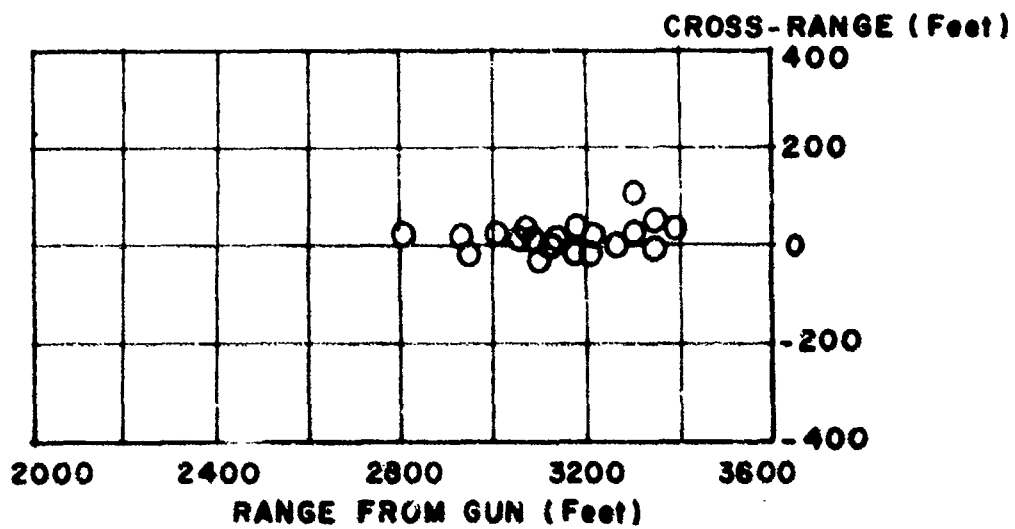
The test results are compared with Monte Carlo simulations using the aerodynamic coefficient data of Table I with appropriate adjustment for longitudinal center of gravity. The Monte Carlo simulations also incorporate the velocity perturbations described above. For the Monte Carlo simulations the configurational asymmetries were assumed to be the same as for the prototype bomblets (paragraph E), including a standard deviation value for cg lateral offset of 0.0016 inch.

The test impact pattern for the ballistic models (Figure 24) shows relatively small cross-range dispersion, as would be expected. The mean center of impact as determined from the test data is 3110 feet from the launch point.

The Monte Carlo simulation for the ballistic models results in a mean center of impact at 3310 feet, or 200 feet greater range than

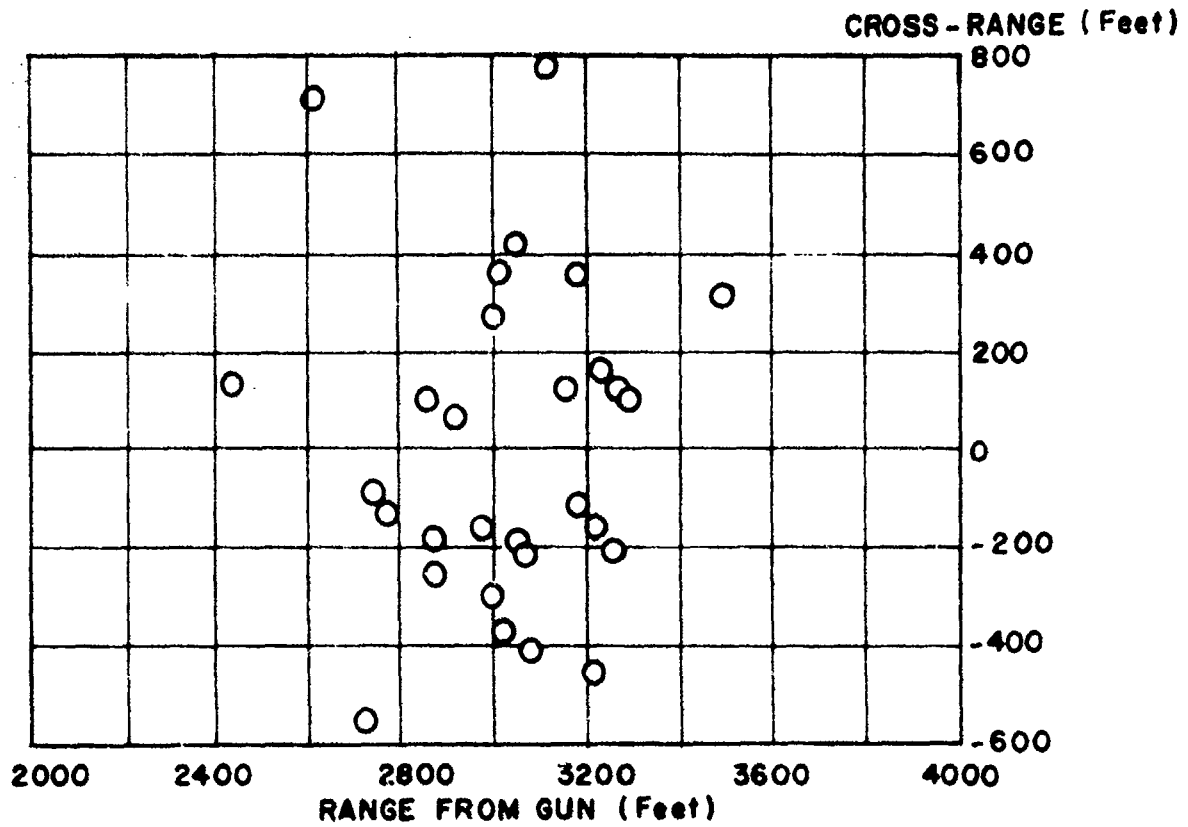


a) Monte Carlo Simulation

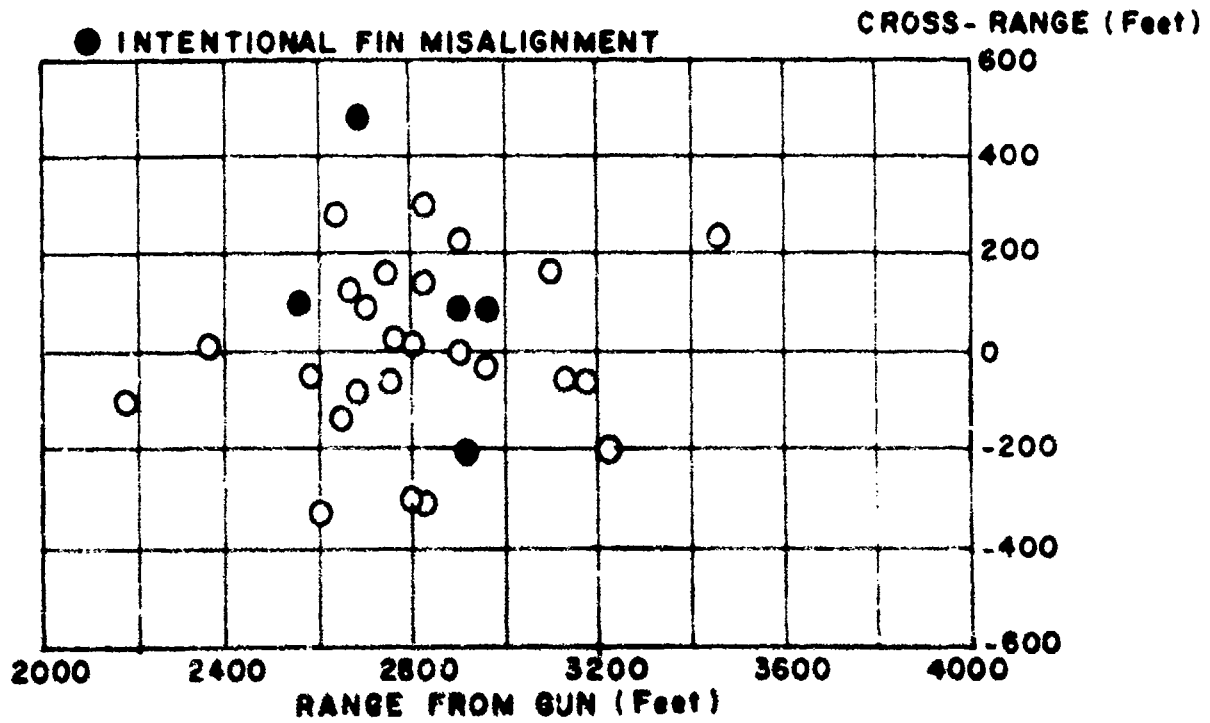


b) Flight Test Data

Figure 24. Flight Test and Simulated Impact Patterns for Air-Gun Launched 3-inch Diameter Ballistic Models



a) Monte Carlo Simulation



b) Flight Test Data

Figure 25. Flight Test and Simulated Impact Patterns for Air-Gun Launched 1-inch Diameter Standard S-Curve Bomblet Models (Cylindrical Afterbody)

the test data. The predicted cross-range dispersion also exceeds the observed cross-range dispersion. Thus, the cross-range velocity perturbations used in the simulations (which were derived from the photo coverage of the test launchings) are probably too large.

The test impact pattern for the standard 3-inch S-Curve models (Figure 25) confirms the effectiveness of the S-Curve dispersion concept. The test impact pattern is approximately 800 feet in width and 1200 feet in length, with the mean center of impact approximately 2800 feet from the launch point.

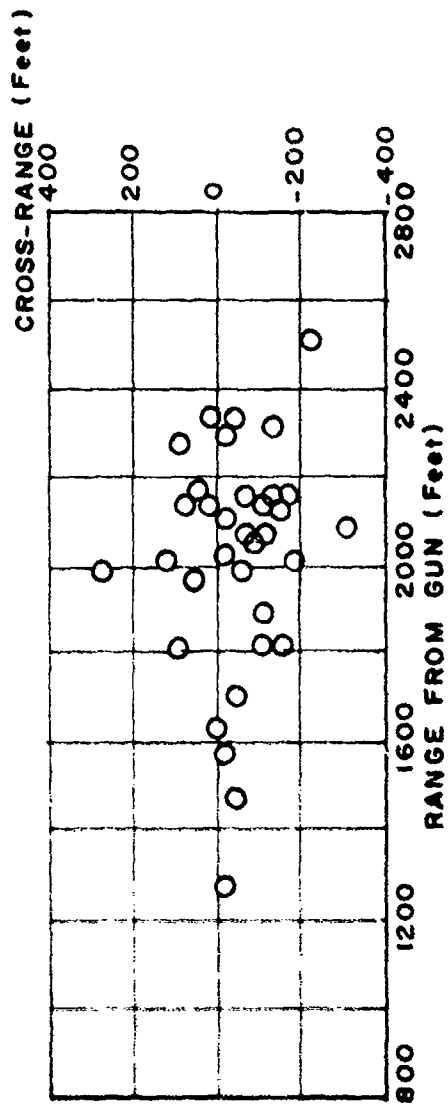
The Monte Carlo simulation for the 3-inch S-Curve models results in an impact pattern similar to the test results, with the mean center of impact about 3000 feet from the launch point. The standard deviations of range and cross range, as determined for both the flight-test and simulated impact patterns, are summarized in Table VI. Comparison of the test data with the Monte Carlo simulation shows that the range dispersion is slightly under-predicted while the cross-range dispersion is over-predicted. The initial cross-range velocity perturbations (which are probably too large) contribute to the over-prediction of the cross-range.

The effect of intentional fin misalignment on the test models is also indicated in Figure 25. Although the sample is small, an improvement in cross-range dispersion is noted with intentional fin cant and roll.

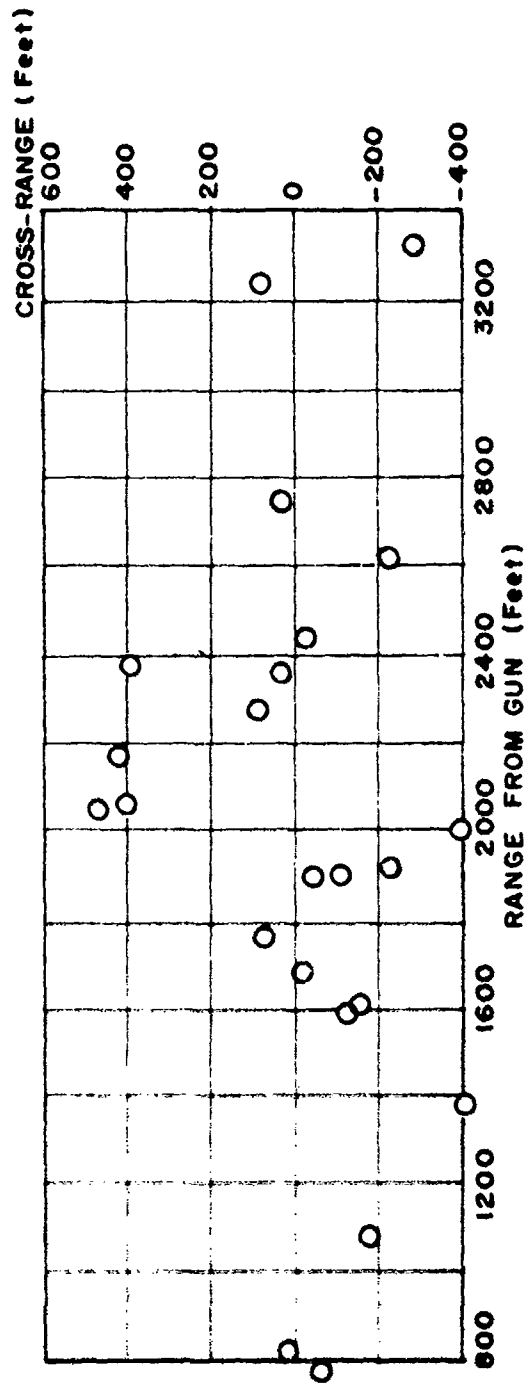
A group of 10 recovered 3-inch-diameter S-Curve models were re-flown to determine the effect of nose scratches and other asymmetries resulting from impact damage. Dispersion data for this test group are summarized in Table VI. As expected, the test data indicate a moderate decrease in both dispersion and range.

Test results for the 1.5-inch-diameter cluster-launched models are shown in Figure 26. An extremely large impact pattern was achieved for the boattail bomblet, while the cylindrical afterbody bomblet displayed an elongated pattern with reduced cross-range dispersion compared with the 3-inch-diameter cylindrical-afterbody bomblet.

Although Monte Carlo simulations were not attempted for the cluster shots (because the initial conditions were poorly known), it was anticipated that the dispersion would increase in proportion to the trimmed lift/weight ratio for the respective model configurations. Thus, the dispersion of the 1.5-inch-diameter cylindrical and boattail-afterbody models was expected to increase compared to the 3-inch-diameter cylindrical-afterbody model by the lift/weight ratios which were 1.23 and 1.44, respectively. The cross-range dispersion of the 1.5-inch-diameter boattail models is in approximate agreement with the lift/weight ratio, but the cross-range dispersion of the 1.5-inch-diameter cylindrical-afterbody models does not agree with the



a) Flight Data - Cylindrical Afterbody Models



b) Flight Data - Boattail Afterbody Models

Figure 26. Flight Test Impact Patterns for Air-Gun Launched 1.5-inch Diameter S-Curve Bomblet Models

lift/weight ratio. No explanation is yet available for the unusual performance of the 1.5-inch-diameter cylindrical-afterbody models.

| TABLE VI. SUMMARY OF IMPACT DISPERSION DATA FOR AIR-GUN-LAUNCHED FREE-FLIGHT MODELS | | | |
|--|------------------------------|--|--|
| | Mean Range (Feet) | Standard Deviation Range (Feet) | Standard Deviation Cross-Range (Feet) |
| 3-Inch-Diameter Ballistic Models | | | |
| Test Results | 3110 | 271 | 27 |
| Monte Carlo Simulation | 3310 | 105 | 119 |
| 3-Inch-Diameter Standard S-Curve Models | | | |
| Test Results ^a | 2783 | 249 | 177 |
| Monte Carlo Simulation | 3033 | 222 | 322 |
| Test Results for Re-Flown Models | 2542 | 227 | 122 |
| 1.5-Inch-Diameter S-Curve Models | | | |
| Test Results--Cylindrical Afterbody | 1981 | 333 | 108 |
| Test Results--Boattail Afterbody | 2033 | 642 | 233 |

^a Includes models with intentional fin misalignment.

SECTION III

ROLL-THROUGH-ZERO BOMBLET INVESTIGATIONS

A. CONFIGURATIONS

During the present contractual effort attention was focused on the development of a practical roll-through-zero bomblet configuration. The principal configurational requirements for this type bomblet are (1) a large trimmed lift coefficient, (2) a means for trimming the bomblet in pitch, and (3) a means for reversing the initial direction of roll.

The roll reversing torque must be small, since the deflection of the bomblet trajectory, and hence the dispersion, has previously been shown (Reference 1) to be related to the static roll torque coefficient by the expression

$$\Delta Y = \frac{C_N}{m'} \left[\frac{\pi I_x'}{C_{l_0}} \right]^{1/2} \quad (2)$$

where ΔY is the total deflection of a roll-through-zero trajectory in relation to a corresponding ballistic trajectory.

In addition, the bomblet must have a relatively large stability margin at trim such that the pitch natural frequency is above the intended range of roll rates. This, in turn, requires that the trim moment be relatively large. At the same time, the induced roll moments due to the trim surfaces must be small in comparison with roll reversing torque coefficient, C_{l_0} . When all of these factors are considered, the design of the roll-through-zero bomblet becomes quite complex.

Investigation has shown that wings and canards, while offering good trimmed lift, tend to have highly unfavorable induced roll and side moments, precluding their use. Likewise, estimates have shown that a drag-type trim device will, in general, provide insufficient trim moment, and may also lead to sizeable induced roll and side moments through interference effects.

The use of intentional fin incidence for trim was proposed as the result of preliminary studies (Reference 1). During the present program the aerodynamics, flight dynamics, and dispersion characteristics of this type configuration were extensively investigated. To allow direct comparison of the performance of the roll-through-zero bomblet with the S-Curve-type bomblet, the body and fin geometry were made identical to the S-Curve configuration B₅N₅₂A₅₁F₅₂. Fin incidence of 10 degrees was then applied to two opposing fins, and an effective fin cant angle of 0.1 degree was

introduced. The resulting basic roll-through-zero configuration is depicted in Figure 27.

The roll-through-zero bomblet configuration discussed in this report is scaled to a diameter of two inches; and the values for the weight and inertia are assumed to be identical to those for the S-Curve-type bomblet, namely,

$$W = 1.51 \text{ lbs}$$

$$I_x = 1.629 \times 10^{-4} \text{ slug-ft}^2$$

$$I = 1.06 \times 10^{-3} \text{ slug-ft}^2$$

In general, it is assumed that the roll-through-zero bomblet will have canted fins and will be released from a spinning dispenser with a known roll rate of the order of 1 to 2 cps. However the requirement for a specific initial roll rate and roll direction is not mandatory since it is possible for the bomblet to provide its own roll rate reversal. Figure 28 shows schematically a roll reversing fin tab, which functions with decreasing dynamic pressure. Other devices, which function on the basis of a delay time, are easily envisioned.

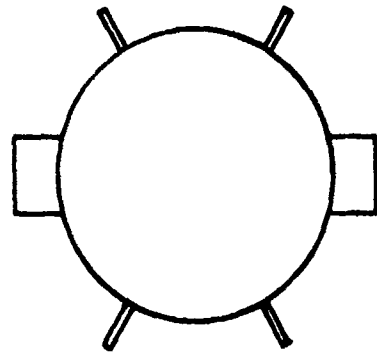
B. AERODYNAMIC CHARACTERISTICS

Static Aerodynamics The static aerodynamic characteristics of the basic roll-through-zero bomblet configuration were evaluated through the transonic range in the 4T wind tunnel at AEDC. For each Mach number and angle of attack six component force and moment data were measured for aerodynamic roll angles from -165 to 180 degrees at intervals of 15 degrees. The trim roll orientation for positive lift corresponds to an aerodynamic roll angle of 180 degrees. Aerodynamic coefficient plots versus aerodynamic roll angle for angles of attack of 10, 15, and 20 degrees and Mach number 0.5 are shown in Figure 29.

The large effect of the aerodynamic roll angle is clearly evident when the coefficients are plotted as a function of ϕ . The first harmonic in roll with period of 2π clearly predominates and is due to the fin incidence. Surprisingly, the second and third harmonic are also evident, with periods of π and $2\pi/3$, respectively, while the usual sixth harmonic (due to the presence of six fins) is not apparent.

The data of Figure 29 also show the loss in normal force due to the trim incidence, and the unstable roll moment variation, $dC_L/d\phi > 0$, at the trim orientation is noteworthy.

For bomblet design purposes, it is important to have a quantitative measure of the fin normal force effectiveness due to incidence. The ratio



VIEW A-A

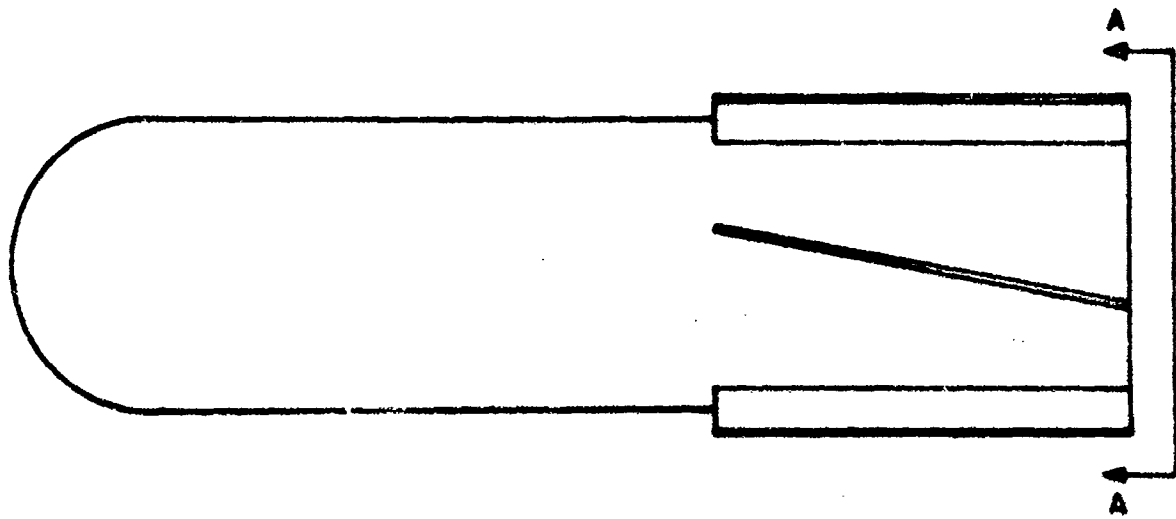
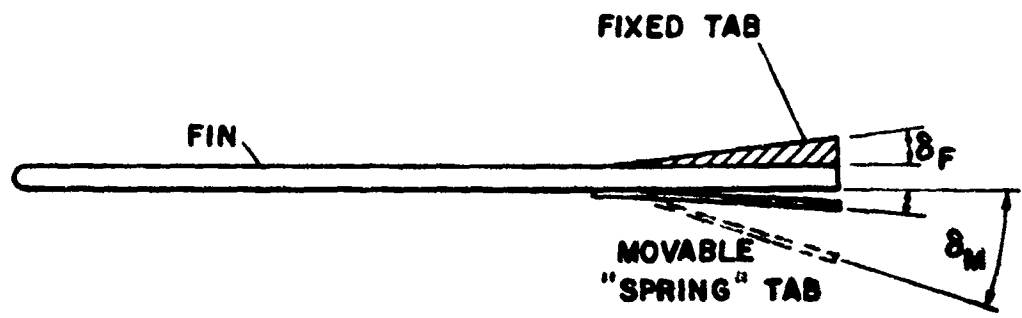


Figure 27. Basic Roll-Through-Zero Bomblet



AT BOMBLETS RELEASE $\delta_M < \delta_F$
 AFTER DECELERATION $\delta_M > \delta_F$

Figure 28. Roll Reversing Tab

ALL DATA FOR 0.5
MACH NUMBER

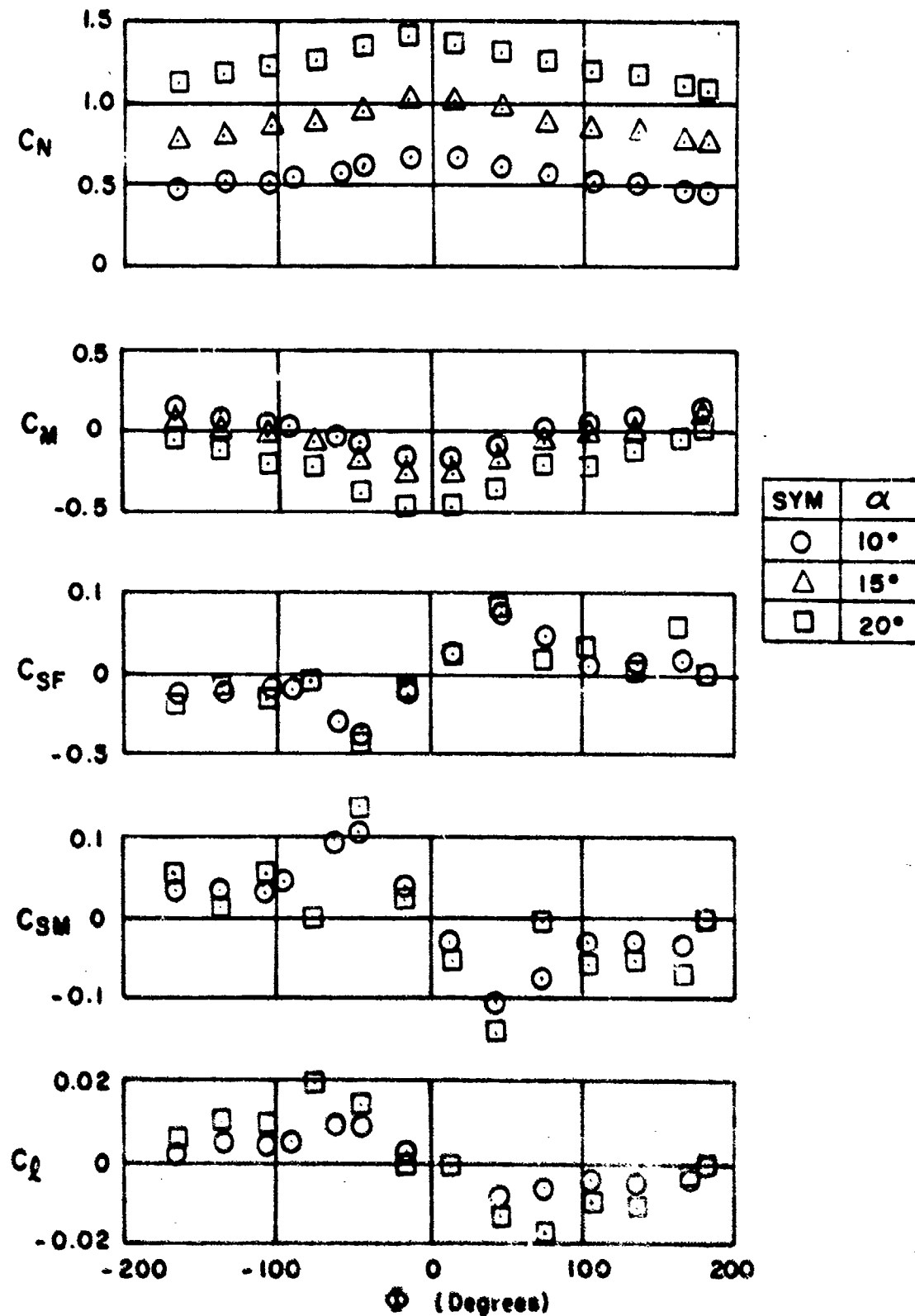


Figure 29. Aerodynamic Characteristics of Roll-Through-Zero Bomblet as Function of the Aerodynamic Roll Angle

$C_{N_\delta} / C_{N_\alpha}$ was determined both from the experimental data and estimated using the method of Reference 20 in conjunction with fin aerodynamic force data from Reference 21. The theory was found to underpredict the $C_{N_\delta} / C_{N_\alpha}$ ratio by a factor of about two at zero angle of attack, but at a 10-degree angle of attack the experimental and theoretical values for $C_{N_\delta} / C_{N_\alpha}$ were 0.58 and 0.53, respectively. The highly nonlinear variation of fin effectiveness with angle of attack complicates the theoretical aerodynamic design, and wind tunnel evaluation of the bomblet trim characteristics are nearly essential.

To obtain a nominal trim angle of attack of 10 degrees at low subsonic velocities, the bomblet longitudinal center-of-gravity was positioned 1.185 calibers from the nose. A more rearward cg would be possible with increased span fins, and the aerodynamic characteristics of such a configuration can be determined from the test data of Reference 13.

Dynamic Stability Parameters Pitch damping, magnus, fin roll effectiveness, and roll damping data for the roll-through-zero bomblet are based on test results for the S-Curve bomblet configuration $B_S N_{S2} A_{S1} F_{S2}$.

Aerodynamic Coefficients for 6-DOF Trajectory Program Adaptation of the wind tunnel aerodynamic coefficients to the 6-DOF trajectory program (Reference 16) was accomplished using first and second harmonics for C_N , C_M , and C_{SF} and first, second and third harmonics for C_{SM} and $C_{l\phi}$. The first harmonics were introduced through the coefficients C_{N_δ} and C_{M_δ} , which are related to C_N , C_{SF} , C_M , and C_{SM} through the aerodynamic roll angle, while higher harmonics in roll were incorporated by the coefficients C_{N_1} , C_{M_1} , C_{SF_1} , C_{SM_2} , C_{SM_3} , $C_{l\phi_1}$, $C_{l\phi_2}$, $C_{l\phi_3}$ as defined in Reference 16. A typical fit to the experimental coefficients using three harmonics is illustrated in Figure 30.

Table VII summarizes the aerodynamic coefficients used in the 6-DOF motion studies and Monte Carlo impact pattern simulations.

C. PREDICTED FLIGHT DYNAMICS

Figure 31 illustrates a typical set of motion histories for the basic roll-through-zero bomblet configuration, based on the standard subsonic event conditions where $HOB = 2000$ feet, $V_E = 900$ fps, and $\gamma_E = 45$ degrees. The data are selected from one of a series of trajectories comprising a Monte Carlo dispersion study. This particular bomblet has an initial negative roll rate of one rps, a mean effectiveness fin cant of 0.115 degree, and a cg lateral offset of 0.001 inch. It is to be noted that for this particular

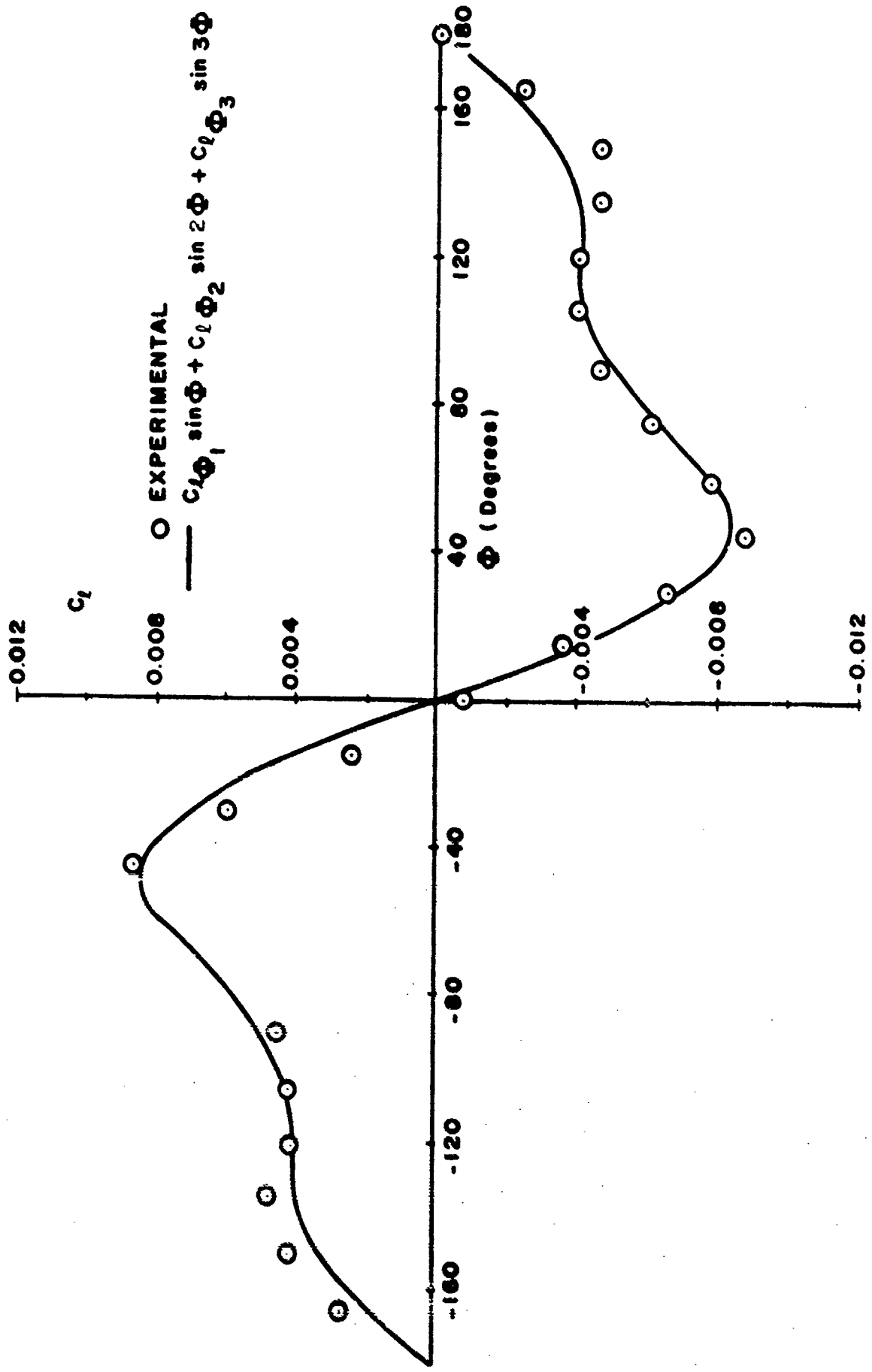


Figure 30. Harmonic Fit to Aerodynamic Induced Roll Moment - Basic Roll-Through-Zero Bomblet

TABLE VII. AERODYNAMIC COEFFICIENT SUMMARY FOR BASIC ROLL-THROUGH-ZERO BOMBLET CONFIGURATION

| AEROBALLISTIC COEFFICIENTS | | | | | | | | | |
|---|-------------|---------------------------|------|------|------|------|------|------|------|
| Coefficient | Mach Number | Angle of Attack - Degrees | | | | | | | |
| | | 0 | 5 | 10 | 15 | 20 | 30 | 40 | 90 |
| C _X | 0.0, 0.8 | .219 | .233 | .253 | .274 | .299 | .315 | .075 | 0 |
| | 0.8 | .020 | 0 | .388 | .405 | .417 | .50 | .25 | 0 |
| C _Y | 0.0, 0.8 | 0 | .2 | .5 | .83 | 1.11 | 2.10 | 6.7 | 5.64 |
| | 0.8 | 0 | .28 | .59 | 1.00 | 1.7 | 2.6 | 6.1 | 6.10 |
| C _M | 0.0, 0.8 | 0 | .075 | .196 | .33 | 0 | 1.24 | 2.61 | 8.75 |
| | 0.8 | 0 | .124 | .205 | .308 | .414 | 1.76 | 6.7 | 8.1 |
| C _M Q | 0.0, 0.8 | 15 | 20 | 26 | 26 | 26 | 25 | 24 | 23 |
| | 0.8 | 19 | 28 | 32 | 31 | 31 | 30 | 27 | 23 |
| C _N R | 0.0, 0.8 | 15 | 20 | 26 | 26 | 24 | 21 | 17 | 13 |
| | 0.8 | 19 | 28 | 32 | 31 | 29 | 26 | 19 | 12 |
| C _N P | 0.0, 0.8 | 0 | 15 | 15 | 1 | .01 | 0 | 1.5 | 1.20 |
| | 0.8 | 0 | 15 | 18 | 1 | .00 | 1.10 | 0 | 0 |
| C _L & 10 ⁻⁴ 10 ⁻⁴ Deg. Cent | 0.0, 0.8 | 15 | 17 | 16 | 10 | 13 | 0 | 0 | 0 |
| | 0.8 | 17 | 16 | 16 | 10 | 13 | 0 | 0 | 0 |
| C _L P | 0.0, 0.8 | 0 | 0 | 0 | 15 | 15 | 15 | 15 | 19 |
| | 0.8 | 0 | 0 | 0 | 12 | 0 | 0 | 10 | 10 |
| C _L Q | 0.0, 0.8 | 0 | 0 | 0 | 14 | 14 | 10 | 10 | 2.0 |
| | 0.8 | 0 | 13 | 13 | 11 | 11 | 10 | 0 | 0 |
| C _D | 0.0, 0.8 | 0.03 | 0.04 | 0.05 | 0.06 | 0.07 | 0.08 | 0.12 | 0.24 |
| | 0.8 | 0.03 | 0.04 | 0.05 | 0.06 | 0.07 | 0.08 | 0.12 | 0.24 |
| C _D Q | 0.0, 0.8 | 0.04 | 0.05 | 0.06 | 0.07 | 0.08 | 0.09 | 0.12 | 0.24 |
| | 0.8 | 0.04 | 0.05 | 0.06 | 0.07 | 0.08 | 0.09 | 0.12 | 0.24 |
| C _D R | 0.0, 0.8 | 0.05 | 0.06 | 0.07 | 0.08 | 0.09 | 0.10 | 0.12 | 0.24 |
| | 0.8 | 0.05 | 0.06 | 0.07 | 0.08 | 0.09 | 0.10 | 0.12 | 0.24 |
| C _D P | 0.0, 0.8 | 0.06 | 0.07 | 0.08 | 0.09 | 0.10 | 0.11 | 0.12 | 0.24 |
| | 0.8 | 0.06 | 0.07 | 0.08 | 0.09 | 0.10 | 0.11 | 0.12 | 0.24 |
| C _D Q | 0.0, 0.8 | 0.07 | 0.08 | 0.09 | 0.10 | 0.11 | 0.12 | 0.13 | 0.24 |
| | 0.8 | 0.07 | 0.08 | 0.09 | 0.10 | 0.11 | 0.12 | 0.13 | 0.24 |
| C _D R | 0.0, 0.8 | 0.08 | 0.09 | 0.10 | 0.11 | 0.12 | 0.13 | 0.14 | 0.24 |
| | 0.8 | 0.08 | 0.09 | 0.10 | 0.11 | 0.12 | 0.13 | 0.14 | 0.24 |
| C _D P | 0.0, 0.8 | 0.09 | 0.10 | 0.11 | 0.12 | 0.13 | 0.14 | 0.15 | 0.24 |
| | 0.8 | 0.09 | 0.10 | 0.11 | 0.12 | 0.13 | 0.14 | 0.15 | 0.24 |
| C _D Q | 0.0, 0.8 | 0.10 | 0.11 | 0.12 | 0.13 | 0.14 | 0.15 | 0.16 | 0.24 |
| | 0.8 | 0.10 | 0.11 | 0.12 | 0.13 | 0.14 | 0.15 | 0.16 | 0.24 |
| C _D R | 0.0, 0.8 | 0.11 | 0.12 | 0.13 | 0.14 | 0.15 | 0.16 | 0.17 | 0.24 |
| | 0.8 | 0.11 | 0.12 | 0.13 | 0.14 | 0.15 | 0.16 | 0.17 | 0.24 |
| C _D P | 0.0, 0.8 | 0.12 | 0.13 | 0.14 | 0.15 | 0.16 | 0.17 | 0.18 | 0.24 |
| | 0.8 | 0.12 | 0.13 | 0.14 | 0.15 | 0.16 | 0.17 | 0.18 | 0.24 |
| C _D Q | 0.0, 0.8 | 0.13 | 0.14 | 0.15 | 0.16 | 0.17 | 0.18 | 0.19 | 0.24 |
| | 0.8 | 0.13 | 0.14 | 0.15 | 0.16 | 0.17 | 0.18 | 0.19 | 0.24 |
| C _D R | 0.0, 0.8 | 0.14 | 0.15 | 0.16 | 0.17 | 0.18 | 0.19 | 0.20 | 0.24 |
| | 0.8 | 0.14 | 0.15 | 0.16 | 0.17 | 0.18 | 0.19 | 0.20 | 0.24 |
| C _D P | 0.0, 0.8 | 0.15 | 0.16 | 0.17 | 0.18 | 0.19 | 0.20 | 0.21 | 0.24 |
| | 0.8 | 0.15 | 0.16 | 0.17 | 0.18 | 0.19 | 0.20 | 0.21 | 0.24 |
| C _D Q | 0.0, 0.8 | 0.16 | 0.17 | 0.18 | 0.19 | 0.20 | 0.21 | 0.22 | 0.24 |
| | 0.8 | 0.16 | 0.17 | 0.18 | 0.19 | 0.20 | 0.21 | 0.22 | 0.24 |
| C _D R | 0.0, 0.8 | 0.17 | 0.18 | 0.19 | 0.20 | 0.21 | 0.22 | 0.23 | 0.24 |
| | 0.8 | 0.17 | 0.18 | 0.19 | 0.20 | 0.21 | 0.22 | 0.23 | 0.24 |
| C _D P | 0.0, 0.8 | 0.18 | 0.19 | 0.20 | 0.21 | 0.22 | 0.23 | 0.24 | 0.24 |
| | 0.8 | 0.18 | 0.19 | 0.20 | 0.21 | 0.22 | 0.23 | 0.24 | 0.24 |
| C _D Q | 0.0, 0.8 | 0.19 | 0.20 | 0.21 | 0.22 | 0.23 | 0.24 | 0.25 | 0.24 |
| | 0.8 | 0.19 | 0.20 | 0.21 | 0.22 | 0.23 | 0.24 | 0.25 | 0.24 |
| C _D R | 0.0, 0.8 | 0.20 | 0.21 | 0.22 | 0.23 | 0.24 | 0.25 | 0.26 | 0.24 |
| | 0.8 | 0.20 | 0.21 | 0.22 | 0.23 | 0.24 | 0.25 | 0.26 | 0.24 |
| C _D P | 0.0, 0.8 | 0.21 | 0.22 | 0.23 | 0.24 | 0.25 | 0.26 | 0.27 | 0.24 |
| | 0.8 | 0.21 | 0.22 | 0.23 | 0.24 | 0.25 | 0.26 | 0.27 | 0.24 |
| C _D Q | 0.0, 0.8 | 0.22 | 0.23 | 0.24 | 0.25 | 0.26 | 0.27 | 0.28 | 0.24 |
| | 0.8 | 0.22 | 0.23 | 0.24 | 0.25 | 0.26 | 0.27 | 0.28 | 0.24 |
| C _D R | 0.0, 0.8 | 0.23 | 0.24 | 0.25 | 0.26 | 0.27 | 0.28 | 0.29 | 0.24 |
| | 0.8 | 0.23 | 0.24 | 0.25 | 0.26 | 0.27 | 0.28 | 0.29 | 0.24 |
| C _D P | 0.0, 0.8 | 0.24 | 0.25 | 0.26 | 0.27 | 0.28 | 0.29 | 0.30 | 0.24 |
| | 0.8 | 0.24 | 0.25 | 0.26 | 0.27 | 0.28 | 0.29 | 0.30 | 0.24 |
| C _D Q | 0.0, 0.8 | 0.25 | 0.26 | 0.27 | 0.28 | 0.29 | 0.30 | 0.31 | 0.24 |
| | 0.8 | 0.25 | 0.26 | 0.27 | 0.28 | 0.29 | 0.30 | 0.31 | 0.24 |
| C _D R | 0.0, 0.8 | 0.26 | 0.27 | 0.28 | 0.29 | 0.30 | 0.31 | 0.32 | 0.24 |
| | 0.8 | 0.26 | 0.27 | 0.28 | 0.29 | 0.30 | 0.31 | 0.32 | 0.24 |
| C _D P | 0.0, 0.8 | 0.27 | 0.28 | 0.29 | 0.30 | 0.31 | 0.32 | 0.33 | 0.24 |
| | 0.8 | 0.27 | 0.28 | 0.29 | 0.30 | 0.31 | 0.32 | 0.33 | 0.24 |
| C _D Q | 0.0, 0.8 | 0.28 | 0.29 | 0.30 | 0.31 | 0.32 | 0.33 | 0.34 | 0.24 |
| | 0.8 | 0.28 | 0.29 | 0.30 | 0.31 | 0.32 | 0.33 | 0.34 | 0.24 |
| C _D R | 0.0, 0.8 | 0.29 | 0.30 | 0.31 | 0.32 | 0.33 | 0.34 | 0.35 | 0.24 |
| | 0.8 | 0.29 | 0.30 | 0.31 | 0.32 | 0.33 | 0.34 | 0.35 | 0.24 |
| C _D P | 0.0, 0.8 | 0.30 | 0.31 | 0.32 | 0.33 | 0.34 | 0.35 | 0.36 | 0.24 |
| | 0.8 | 0.30 | 0.31 | 0.32 | 0.33 | 0.34 | 0.35 | 0.36 | 0.24 |
| C _D Q | 0.0, 0.8 | 0.31 | 0.32 | 0.33 | 0.34 | 0.35 | 0.36 | 0.37 | 0.24 |
| | 0.8 | 0.31 | 0.32 | 0.33 | 0.34 | 0.35 | 0.36 | 0.37 | 0.24 |
| C _D R | 0.0, 0.8 | 0.32 | 0.33 | 0.34 | 0.35 | 0.36 | 0.37 | 0.38 | 0.24 |
| | 0.8 | 0.32 | 0.33 | 0.34 | 0.35 | 0.36 | 0.37 | 0.38 | 0.24 |
| C _D P | 0.0, 0.8 | 0.33 | 0.34 | 0.35 | 0.36 | 0.37 | 0.38 | 0.39 | 0.24 |
| | 0.8 | 0.33 | 0.34 | 0.35 | 0.36 | 0.37 | 0.38 | 0.39 | 0.24 |
| C _D Q | 0.0, 0.8 | 0.34 | 0.35 | 0.36 | 0.37 | 0.38 | 0.39 | 0.40 | 0.24 |
| | 0.8 | 0.34 | 0.35 | 0.36 | 0.37 | 0.38 | 0.39 | 0.40 | 0.24 |
| C _D R | 0.0, 0.8 | 0.35 | 0.36 | 0.37 | 0.38 | 0.39 | 0.40 | 0.41 | 0.24 |
| | 0.8 | 0.35 | 0.36 | 0.37 | 0.38 | 0.39 | 0.40 | 0.41 | 0.24 |
| C _D P | 0.0, 0.8 | 0.36 | 0.37 | 0.38 | 0.39 | 0.40 | 0.41 | 0.42 | 0.24 |
| | 0.8 | 0.36 | 0.37 | 0.38 | 0.39 | 0.40 | 0.41 | 0.42 | 0.24 |
| C _D Q | 0.0, 0.8 | 0.37 | 0.38 | 0.39 | 0.40 | 0.41 | 0.42 | 0.43 | 0.24 |
| | 0.8 | 0.37 | 0.38 | 0.39 | 0.40 | 0.41 | 0.42 | 0.43 | 0.24 |
| C _D R | 0.0, 0.8 | 0.38 | 0.39 | 0.40 | 0.41 | 0.42 | 0.43 | 0.44 | 0.24 |
| | 0.8 | 0.38 | 0.39 | 0.40 | 0.41 | 0.42 | 0.43 | 0.44 | 0.24 |
| C _D P | 0.0, 0.8 | 0.39 | 0.40 | 0.41 | 0.42 | 0.43 | 0.44 | 0.45 | 0.24 |
| | 0.8 | 0.39 | 0.40 | 0.41 | 0.42 | 0.43 | 0.44 | 0.45 | 0.24 |
| C _D Q | 0.0, 0.8 | 0.40 | 0.41 | 0.42 | 0.43 | 0.44 | 0.45 | 0.46 | 0.24 |
| | 0.8 | 0.40 | 0.41 | 0.42 | 0.43 | 0.44 | 0.45 | 0.46 | 0.24 |
| C _D R | 0.0, 0.8 | 0.41 | 0.42 | 0.43 | 0.44 | 0.45 | 0.46 | 0.47 | 0.24 |
| | 0.8 | 0.41 | 0.42 | 0.43 | 0.44 | 0.45 | 0.46 | 0.47 | 0.24 |
| C _D P | 0.0, 0.8 | 0.42 | 0.43 | 0.44 | 0.45 | 0.46 | 0.47 | 0.48 | 0.24 |
| | 0.8 | 0.42 | 0.43 | 0.44 | 0.45 | 0.46 | 0.47 | 0.48 | 0.24 |
| C _D Q | 0.0, 0.8 | 0.43 | 0.44 | 0.45 | 0.46 | 0.47 | 0.48 | 0.49 | 0.24 |
| | 0.8 | 0.43 | 0.44 | 0.45 | 0.46 | 0.47 | 0.48 | 0.49 | 0.24 |
| C _D R | 0.0, 0.8 | 0.44 | 0.45 | 0.46 | 0.47 | 0.48 | 0.49 | 0.50 | 0.24 |
| | 0.8 | 0.44 | 0.45 | 0.46 | 0.47 | 0.48 | 0.49 | 0.50 | 0.24 |
| C _D P | 0.0, 0.8 | 0.45 | 0.46 | 0.47 | 0.48 | 0.49 | 0.50 | 0.51 | 0.24 |
| | 0.8 | 0.45 | 0.46 | 0.47 | 0.48 | 0.49 | 0.50 | 0.51 | 0.24 |
| C _D Q | 0.0, 0.8 | 0.46 | 0.47 | 0.48 | 0.49 | 0.50 | 0.51 | 0.52 | 0.24 |
| | 0.8 | 0.46 | 0.47 | 0.48 | 0.49 | 0.50 | 0.51 | 0.52 | 0.24 |
| C _D R | 0.0, 0.8 | 0.47 | 0.48 | 0.49 | 0.50 | 0.51 | 0.52 | 0.53 | 0.24 |
| | 0.8 | 0.47 | 0.48 | 0.49 | 0.50 | 0.51 | 0.52 | 0.53 | 0.24 |
| C _D P | 0.0, 0.8 | 0.48 | 0.49 | 0.50 | 0.51 | 0.52 | 0.53 | 0.54 | 0.24 |
| | 0.8 | 0.48 | 0.49 | 0.50 | 0.51 | 0.52 | 0.53 | 0.54 | 0.24 |
| C _D Q | 0.0, 0.8 | 0.49 | 0.50 | 0.51 | 0.52 | 0.53 | 0.54 | 0.55 | 0.24 |
| | 0.8 | 0.49 | 0.50 | 0.51 | 0.52 | 0.53 | 0.54 | 0.55 | 0.24 |
| C _D R | 0.0, 0.8 | 0.50 | 0.51 | 0.52 | 0.53 | 0.54 | 0.55 | 0.56 | 0.24 |
| | 0.8 | 0.50 | 0.51 | 0.52 | 0.53 | 0.54 | 0.55 | 0.56 | 0.24 |
| C _D P | 0.0, 0.8 | 0.51 | 0.52 | 0.53 | 0.54 | 0.55 | 0.56 | 0.57 | 0.24 |
| | 0.8 | 0.51 | 0.52 | 0.53 | 0.54 | 0.55 | 0.56 | 0.57 | 0.24 |
| C _D Q</ | | | | | | | | | |

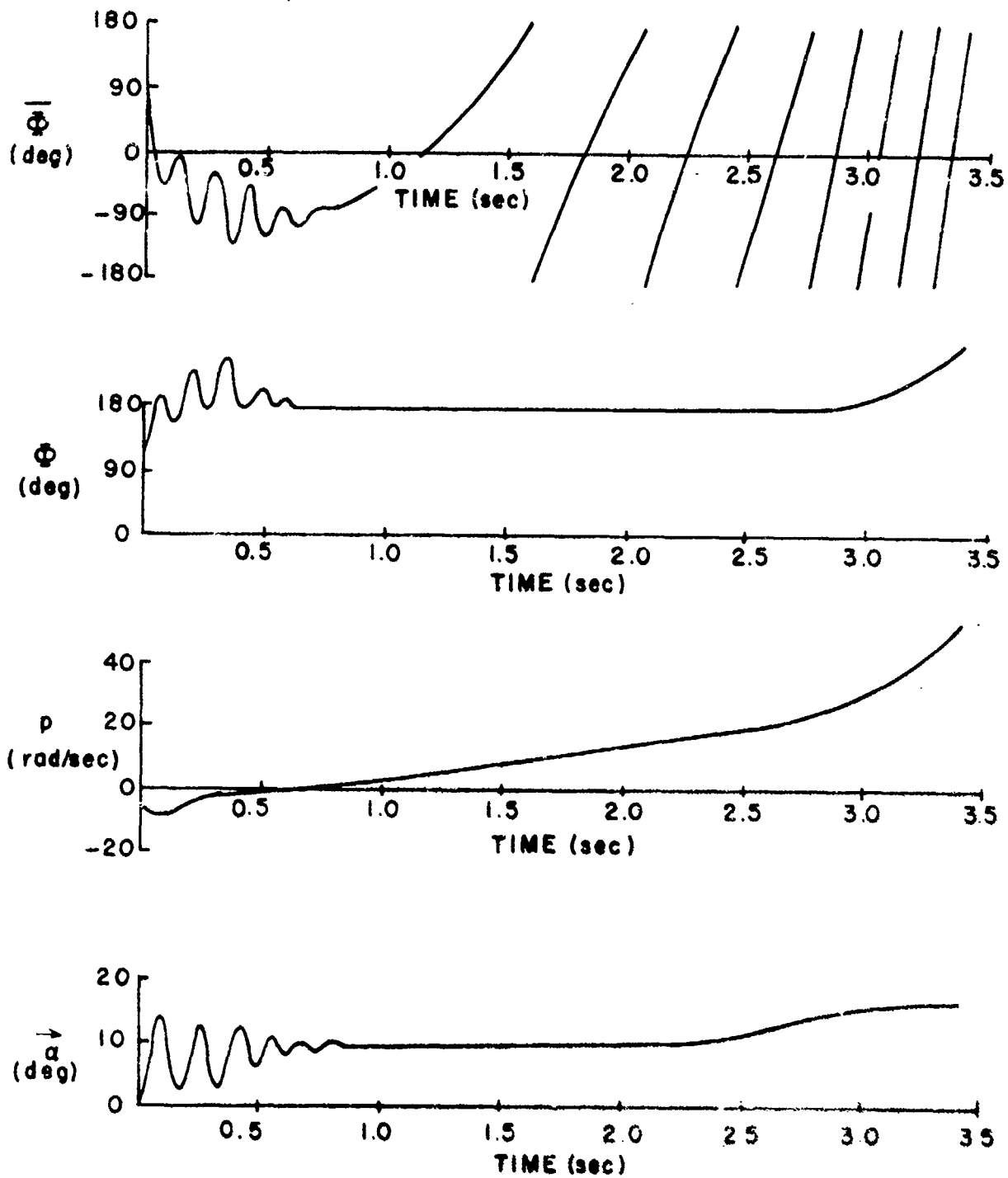


Figure 31. Motion Histories for Basic Roll-Through-Zero Doublet

bomblet the maximum induced roll moment due to cg lateral offset is about 60 percent of that due to the intentional fin cant.

The variables used to describe the motion are the angle of attack plane orientation, $\bar{\phi}$, the aerodynamic roll angle, ϕ , the roll rate, p , and the total angle of attack, $\bar{\alpha}$.

Examination of the motion histories shows that about 0.5 second are required for the bomblet to attain zero roll rate and for the roll angle to stabilize at the trim orientation. The initial motion is well-behaved, with the angle of attack plane remaining in a single quadrant for about one second of flight such that large dispersion can occur.

During the initial phase of flight and until about three seconds after release the aerodynamic roll angle remains stable at $\phi = \pi$, even though the total aerodynamic induced roll torque has an unstable, or positive, gradient with respect to the aerodynamic roll angle. The stable motion behavior can be explained by the side moment, which at the trim angle of attack has a maximum value an order of magnitude larger than the maximum induced roll moment. At trim the gradient of the side moment is such that the coning motion tends to stabilize the trim orientation.⁵

After about three seconds of flight the nature of the motion changes due to the increasing roll rate, which is approaching the bomblet pitch-roll resonance frequency. This results in the familiar trim phase shift and trim amplification, both of which effects are easily seen in the motion data.

The necessity for suitably restricting the cg lateral offset of the roll-through-zero bomblet must be emphasized. Because the aerodynamic roll angle under trim conditions is invariant with respect to the incidence plane, random orientation of the cg lateral offset will produce roll torques which are both random in magnitude and direction, with attendant large variations in roll torque between bomblets. These roll torque variations could, for even a moderately large cg offset, exceed the intentional fin cant roll torque, and result in rapid roll rate build-up to values exceeding the pitch resonance frequency.

D. DISPERSION PREDICTION

As with the S-Curve bomblet, the intent of the present effort has been to provide realistic impact dispersion simulations, using the Monte Carlo method. To provide for comparison of the S-Curve and roll-through-zero

⁵ This fact was proven by reversal of the roll moment and side moment gradients. With a stable roll moment and unstable side moment, the motion became violently unstable with no tendency for trim.

bomblet performance, the standard subsonic event condition was utilized as the basis for the dispersion simulations.

The physical characteristics of the 2-inch-diameter roll-through-zero bomblet have been previously described. For the dispersion simulations, the mean fin cant angle was assumed to be 0.100 degree with a standard deviation or error of 0.0816 degree. The standard deviation of cg offset was taken to be 0.0016 inch. Because of the large fin incidence employed for trim, no other lateral misalignments were considered.

The computed impact pattern for the roll-through-zero bomblet is shown in Figure 32. The pattern is of approximately circular shape with a diameter of about 650 feet. The standard deviations of range and cross-range dispersion are summarized in Table VIII, along with the comparative data for the S-Curve bomblet.

| Bomblet Type | Mean Range X (Feet) | Mean Cross-Range Y (Feet) | Standard Deviation Range σ_X (Feet) | Standard Deviation Cross-Range σ_Y (Feet) |
|-------------------|---------------------------|---------------------------------|---|---|
| Roll-Through Zero | 1805 | -28 | 133 | 159 |
| S Curve | 1899 | -26 | 246 | 185 |

Comparison with S-Curve Bomblet The roll-through-zero bomblet configuration considered in this investigation has effective dispersion, but the area coverage is not quite as large as that achieved by the S-Curve type bomblet. The primary reason for the smaller area coverage of the roll-through-zero bomblet is the lower value of trimmed lift. Although both types of bomblets have been designed for a nominal trim angle of attack of about 10 degrees, the lift curve slope of the present roll-through-zero bomblet is appreciably reduced by the fin negative lift force required for trim. At Mach number 0.5 and at 10 degrees angle of attack, the roll-through-zero bomblet has a lift coefficient of 0.45, compared to a lift coefficient of 0.58 for the S-Curve bomblet. With allowance for the lift coefficient, the dispersion of the roll-through-zero and S-Curve bomblets is comparable. It is significant that the trimmed lift coefficient for the roll-through-zero bomblet can be increased to a value of 0.58 at 10 degrees angle of attack by increasing the fin exposed semi-span from 0.078 to 0.140 radians.

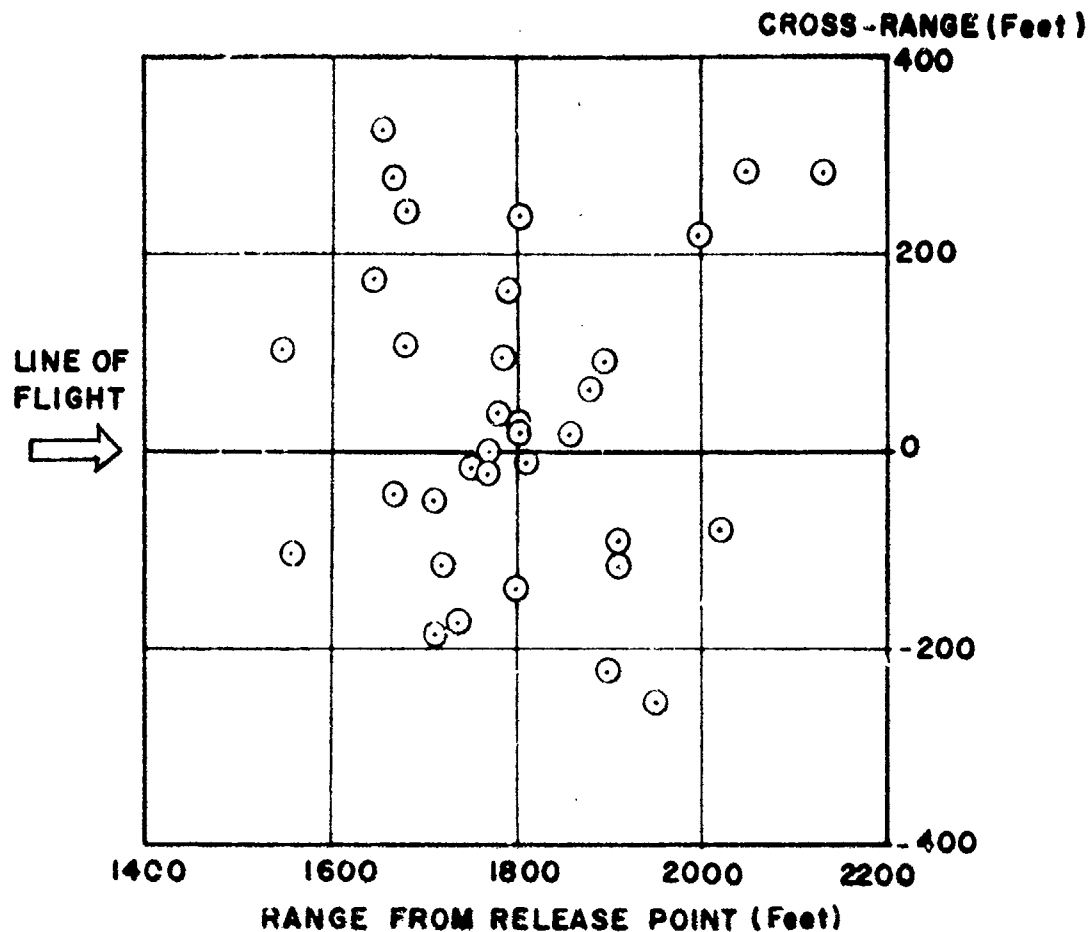


Figure 32. Monte Carlo Impact Pattern Prediction for Basic Roll-Through-Zero Bomblet - High-Subsonic Event Condition

Comparison with Theory A simplified theoretical prediction of the roll-through-zero bomblet dispersion can be obtained using equation (2) in conjunction with the dispersion approximations

$$r = \frac{h}{\sin \gamma} \Delta Y \quad (3)$$

$$R = \frac{h}{\sin^2 \gamma} \Delta Y \quad (4)$$

where r and R represent the cross-range dispersion and range dispersion, respectively, at ground impact. In the theoretical calculations, it is assumed that the roll torque coefficient, C_{L_0} , is due only to the mean fin cant angle. The induced roll torques are not included because they are random. Table IX compares the standard deviation values of range and cross-range dispersion, as obtained from the Monte Carlo simulations, with the theoretical predictions for r and R .

TABLE IX. COMPARISON OF THEORETICAL AND MONTE CARLO
DISPERSION PREDICTIONS FOR ROLL-THROUGH-ZERO
BOMBLET

| | Cross-Range Dispersion (Feet) | Range Dispersion (Feet) |
|--|-------------------------------------|-------------------------------|
| Monte Carlo; σ_x and σ_y | 159 | 133 |
| Theoretical; r and R | 540 | 764 |

The reason for the poor agreement between the theoretical and Monte Carlo predictions is believed to be due primarily to the fact that the induced roll torques are not included in the theoretical prediction.

SECTION IV

DEVELOPMENT OF MONTE CARLO METHOD FOR DISPERSION PREDICTION

A. GENERAL

The Monte Carlo technique is a procedure by which one can obtain approximate evaluations of mathematical relationships which involve one or more probability distribution functions.

The Monte Carlo technique consists of simulating an experiment to determine some probabilistic property of a population of events by the use of random sampling applied to the components of the events. In the present application of this mathematical definition, the experiment is the deployment of a bomblet cluster, the events are the bomblet trajectories, a probabilistic property of the events is the impact pattern, and the random sampling is applied to those variables which affect the bomblet trajectories, namely, the initial motion parameters and the bomblet configurational asymmetries. We could also include atmospheric or flow disturbances along the trajectories.

The application of the Monte Carlo technique to the flight period immediately after dispenser opening is extremely difficult because during this period multi-component flow conditions and very large bomblet-bomblet and bomblet-dispenser interference effects exist, and these have to be describable in probabilistic terms for the trajectories to be simulated. However, after a brief interval time, break-up of the bomblet cluster usually occurs, such that some of the bomblets are free of interference effects. If the probable flight conditions at cluster break-out are established, then the bomblet trajectories can be initiated at the time of break-out, and the trajectory computations are greatly simplified.

B. MONTE CARLO TRAJECTORY PROGRAM

Using the cluster break-out concept, a Monte Carlo trajectory program was developed. This program provides for the sequential calculation of a pre-set number of 6-DOF trajectories and corresponding impact points, using statistical input for the cluster break-out conditions and configurational asymmetries. To provide the required generality in the equations of motion, a number of modifications and additions were made to the Extended Capability Magnus Rotor and Ballistic Body 6-DOF Trajectory Program (Reference 3), and a new subroutine MONCAR was incorporated to provide statistical input data to the 6-DOF trajectory program. A complete description of the new Monte Carlo trajectory program is provided in Reference 16.

Initial Motion Parameters The Monte Carlo trajectory program is structured such that the bomblet 6-DOF motion prediction commences at cluster break-out. The general assumptions which are used to establish the conditions at cluster break-out are as follows:

1. Each bomblet has a time of cluster break-out, t_{b_0} , defined by an unspecified probability distribution.
2. Prior to cluster break-out, the leading edge of the cluster decelerates uniformly and follows a straight flight path, coincident with the dispenser flight path at event.
3. The cluster is radially symmetric with respect to bomblet position and velocity.
4. Cluster break-out begins from the cluster leading edge and on the cluster axis of rotational symmetry.

Figure 33 shows, schematically, the variables which control the bomblet initial position, velocity, and pitch attitude at cluster break-out. The probabilistic initial motion parameters and their probability distributions for specified event conditions, are given below.

| <u>Variable</u> | <u>Description</u> | <u>Probability Distribution</u> |
|-----------------|---|---------------------------------|
| t_{b_0} | Cluster break-out time | Arbitrary |
| V_R | Radial velocity at break-out | Arbitrary |
| ψ_R | Velocity orientation at break-out | Uniformly random |
| α | Angle of attack at cluster break-out | Arbitrary |
| $\bar{\psi}$ | Angle of attack plane orientation at cluster break-out | Uniformly random |
| $\dot{\alpha}$ | Pitch rate in $\bar{\alpha}$ plane at cluster break-out | Arbitrary |
| $\dot{\psi}$ | Yaw rate at cluster break-out | Arbitrary |
| $\dot{\rho}$ | Roll rate at cluster break-out | Arbitrary |
| ρ | Roll orientation of body axes at cluster break-out. | Uniformly random |

From these quantities, the event conditions and the specified cluster deceleration, the initial conditions required for the basic 6-DOF trajectory program are determined.

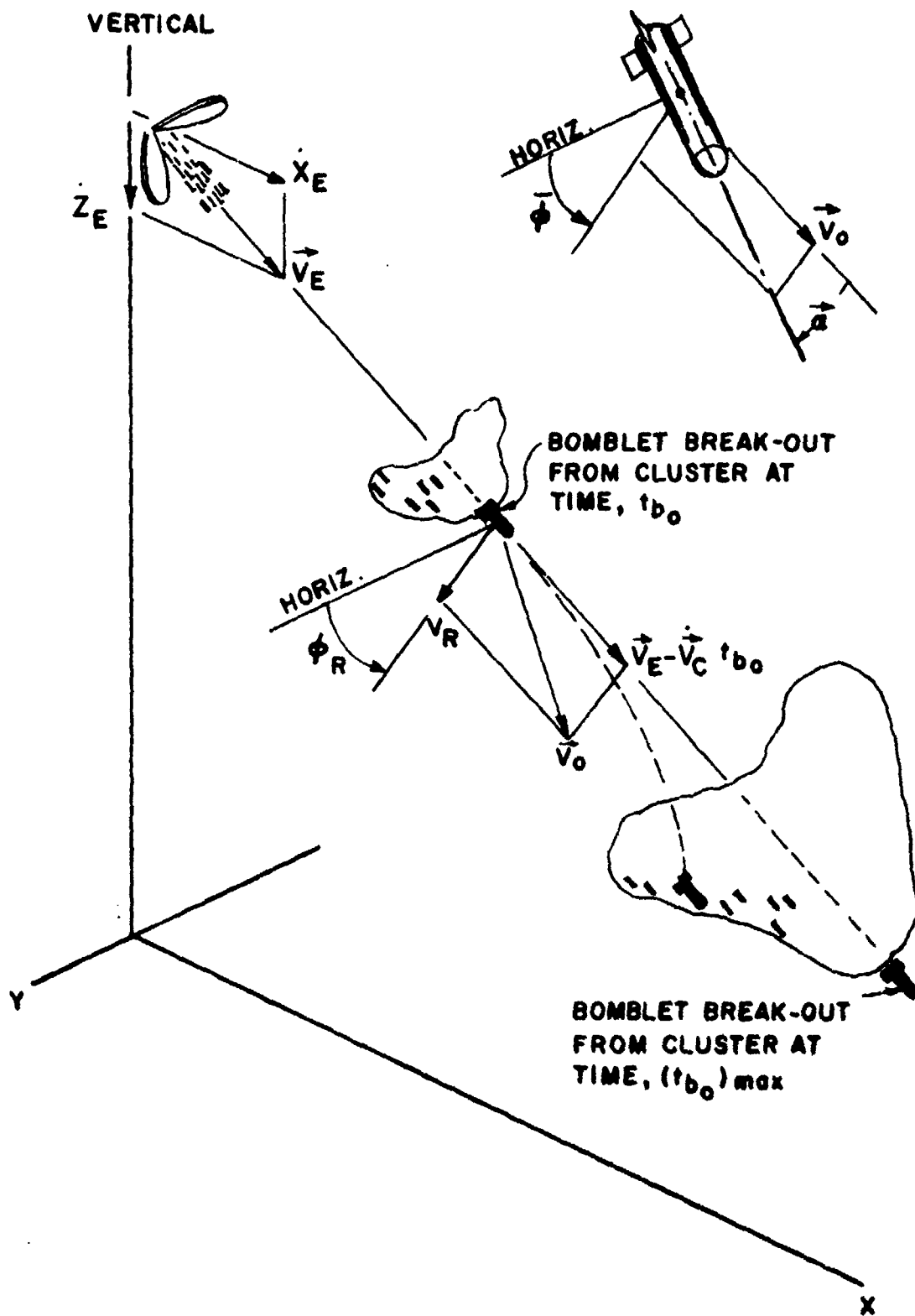


Figure 33. Schematic of Bomblet Cluster Break-Up and Definition of Initial Motion Perturbations

Configurational Asymmetries The Monte Carlo subroutines and 6-DOF equations of motion have been formulated in such a manner that the following geometric and inertial asymmetries can be input in probabilistic form.

| <u>Symbol</u> | <u>Description</u> | <u>Probability Distribution</u> |
|------------------------|------------------------------|---------------------------------|
| δ_{CANT} | Fin cant | Normal |
| δ_{LAT} | Lateral misalignment | Normal |
| Δy | Lateral cg offset | Normal |
| Δx | Axial cg offset | Normal |
| Δm | Mass | Normal |
| ΔI_x | Axial moment of inertia | Normal |
| ΔI | Transverse moment of inertia | Normal |
| ΔI_{xy} | Product of inertia | Normal |

Complete generality in angular orientation of the asymmetries is assumed by introducing the following probabilistic angles.⁶

| <u>Symbol</u> | <u>Description</u> | <u>Probability Distribution</u> |
|---------------|--|---------------------------------|
| ψ | Roll orientation of aerodynamic surfaces | Uniform |
| ϕ | Roll orientation of aerodynamic misalignment | Uniform |

Aerodynamic Asymmetries Aerodynamic asymmetry coefficients C_{y0} , C_{z0} , C_{m0} , and C_{p0} , can also be introduced directly into the Monte Carlo simulation but, in most instances, fin cant asymmetry and lateral misalignment adequately describe both the geometric and aerodynamic asymmetries. However, for some configurations it is also necessary to account for flow asymmetries which cannot be related to fin cant or lateral misalignment. Such flow asymmetries can be triggered, for instance, by almost undetectable nose roughness, and can result in so-called pseudo magnus forces and moments as well as induced roll moments. Provision has been made in the Monte Carlo trajectory program for such phenomena.

Probability Distribution Functions The Monte Carlo computer program provides for three types of probability distribution functions.

⁶ The dynamic unbalance, ΔI_{xy} , is restricted to the same plane as the static unbalance, Δy .

1. Uniformly random
2. Normal distribution
3. Arbitrary distribution function

All of the probabilistic variables are determined from a random number subroutine RANF.

The uniformly random variables are determined directly by multiplication of RANF and an appropriate constant.

The normal distribution is obtained from the specified mean value of the variable and normal deviates. The normal deviates are obtained using the Gaussian approximation

$$\text{GAUSS} = -6 \pm \sum_{i=1}^{i=12} \text{RANF}(X_i) \quad (5)$$

The arbitrary distribution functions are provided by tables where the arguments are the cumulative frequency normalized 0 to 1.0 and the ordinates are the probable values of the variable.

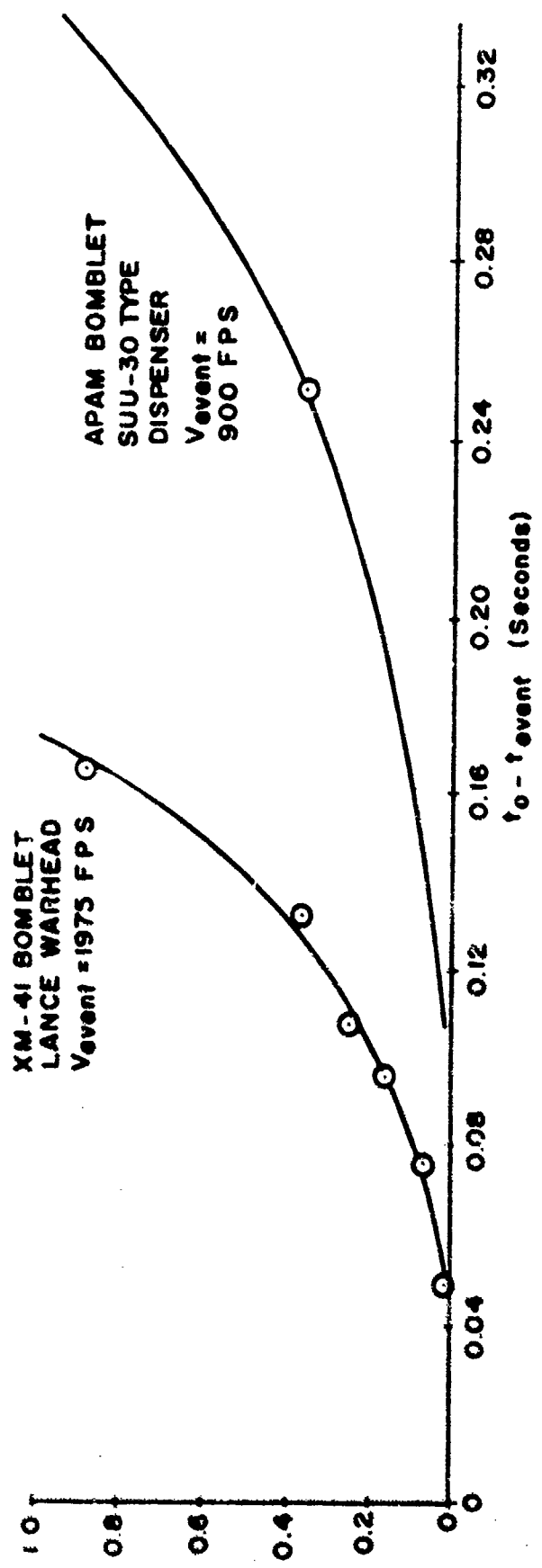
C. STATISTICAL ANALYSIS OF CLUSTER BREAK-UP

To obtain the probability distribution functions for the motion parameters at cluster break-out, it was necessary to examine experimental cluster break-up data. Photographic data from sled tests of a Lance missile bomb-let warhead with approximately 1600 XM-41 bomblets were analyzed to determine cluster leading edge velocity and lateral and longitudinal dispersal as a function of time.

Cluster Break-Out Time Figure 34 illustrates the cumulative frequency distribution as a function of time of those bomblets which have attained separation from the dense central cluster (separation is defined as a density of bomblets of 35 units per square yard or less in a sectional view of the cluster, or about 10 diameters bomblet-bomblet separation), for a warhead event velocity of 1975 fps. A similar statistical variation, adjusted to the available data for a subsonic APAM bomblet cluster, is also presented in Figure 34.

Cluster Deceleration Figure 35 illustrates the longitudinal deceleration of the cluster leading edge as a function of event velocity, based on two separate sled tests of the Lance warhead. For each of the tests, the deceleration was found to be nearly constant during the cluster break-up period. When plotted as a function of velocity the results show that the

CUMULATIVE FRACTION
OF BOMBLETS IN
FREE-FLIGHT



**XM-41 BOMBLET
LANCE WARHEAD**
V_{event} = 1975 FPS

**APAM BOMBLET
SUU-30 TYPE
DISPENSER**
V_{event} =
900 FPS

Figure 14. Experimental Cumulative Frequency Distribution for Cluster Break-Out Time

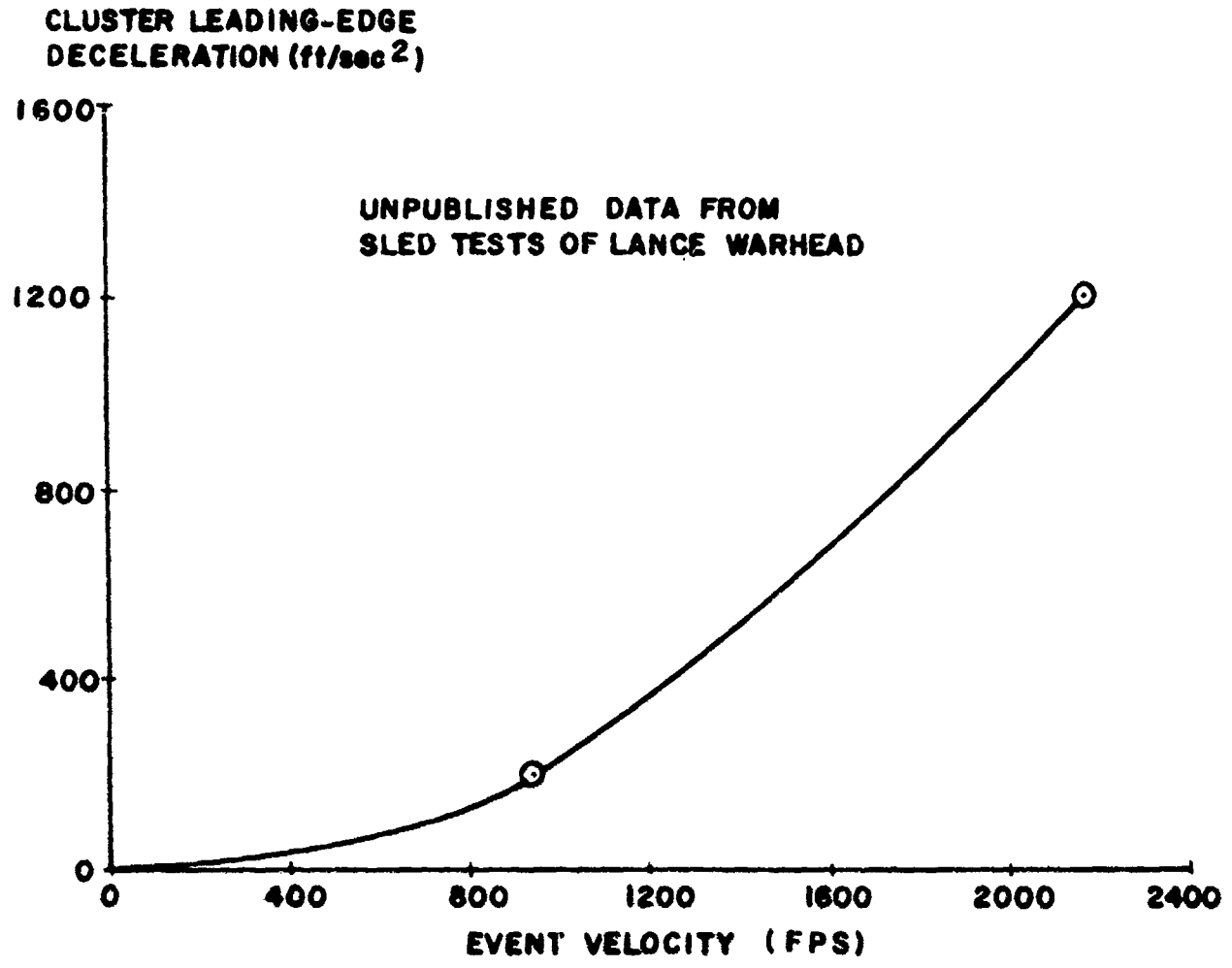


Figure 35. Experimental Data for Bomblet-Cluster Deceleration

cluster deceleration is very nearly proportional to the square of the event velocity.

Radial Velocity The lateral expansion of bomblet clusters has been investigated both from experimental data and theoretical considerations as a means of determining the bomblet radial velocity statistics.

The Lance missile sled test data indicate maximum aerodynamic-induced lateral cluster-spread velocities of the order of 130 fps for an event velocity of 2175 fps. The frequency distribution is approximately parabolic with respect to a zero mean.

Ground impact pattern data for a non-selfdispersing cluster munition (Reference 22) were also analyzed as a means of obtaining the initial radial velocity perturbations. Theoretical dispersion patterns were computed as a function of the initial radial velocity and matched to the observed cross-range impact dispersion to obtain an estimate of the actual radial velocity.⁷ In a similar manner, the difference between the predicted and actual along-range dispersion was used to obtain an estimate of the cluster break-up time.

The above determinations of the induced lateral velocity are compared in Figure 36 with measurements for APAM bomblet clusters (Reference 23). There is seen to be very good agreement in the two sources of subsonic data.

A theoretical prediction has been made of the lateral velocity imparted to a bomblet initially at the leading edge of the cluster. The detailed development of the theory is shown in Appendix I. The theory shows that the radial velocity, V_R , is a linear function of the event velocity in accordance with the following formula:

$$V_R = V_E \left[0.39 \frac{g \rho R}{(W/C_D S)_B} \right]^{1/2} \quad (6)$$

where

V_E = event velocity

g = acceleration due to gravity

ρ = air density

⁷ It is noteworthy that the standard deviation of radial velocity does not correspond to the standard deviation of cross range because the initial cross-range velocity is proportional to the sine of ϕ_R . Assuming that V_R is normally distributed, the standard deviation of radial velocity corresponds to an 89% cumulative frequency for the cross range.

R = cluster core radius

$(W/C_D S)_B$ = bomblet ballistic coefficient.

If the cluster core diameter is taken to be about four times the dispenser diameter, the theoretical V_R is in nearly exact agreement with the experimental data of Figure 36. The importance of the above result is that it shows that the spread velocity is dependent upon both the size of the cluster and the bomblet ballistic coefficient.

Effect of Spinning Dispenser All of the previous data and analyses of lateral spreading are based on small or negligible dispenser spin rates. For spinning dispensers, an additional lateral velocity component will be generated, which will combine with the aerodynamic induced velocity, and the maximum lateral velocity will be given by

$$(V_R)_{TOTAL} = \left[(V_R)_{AERO}^2 + (r\omega)^2 \right]^{1/2} \quad (7)$$

where

ω = dispenser angular velocity

r = maximum radial displacement of bomblets from dispenser axis of rotation

Angle of Attack and Angular Velocity at Cluster Break-Out The initial angle of attack and angular velocity at cluster break-up cannot be generalized, and depend largely upon the bomblet configuration. For small, low-fineness-ratio bodies without stabilizing fins it has been shown that the initial attitude will tend to be uniformly random. Qualitative inspection of Rockeye and APAM bomblet motions during cluster break-up reveals that the maximum angle of attack seldom exceeds about 45 degrees. If the pitching moment coefficient is known as a function of angle of attack, it is possible to relate the maximum angle of attack and the pitch rate at zero angle of attack. It is then reasonable to assume that the pitch rate at zero angle of attack follows a normal distribution.

Using this procedure and assuming that the maximum angle of attack (two sigma) is 45 degrees, the corresponding pitch rate for the S-Curve and roll-through-zero bomblets is about 70 radians/second for an event velocity of 900 fps.

D. STATISTICAL ANALYSIS OF CONFIGURATIONAL ASYMMETRIES

Fin Cant Error The effective fin cant asymmetry for a multi-finned configuration can be computed from alignment and accuracy measurements on individual fins, or extracted from observations of the spin behavior of a representative quantity of test configurations. The resulting effective

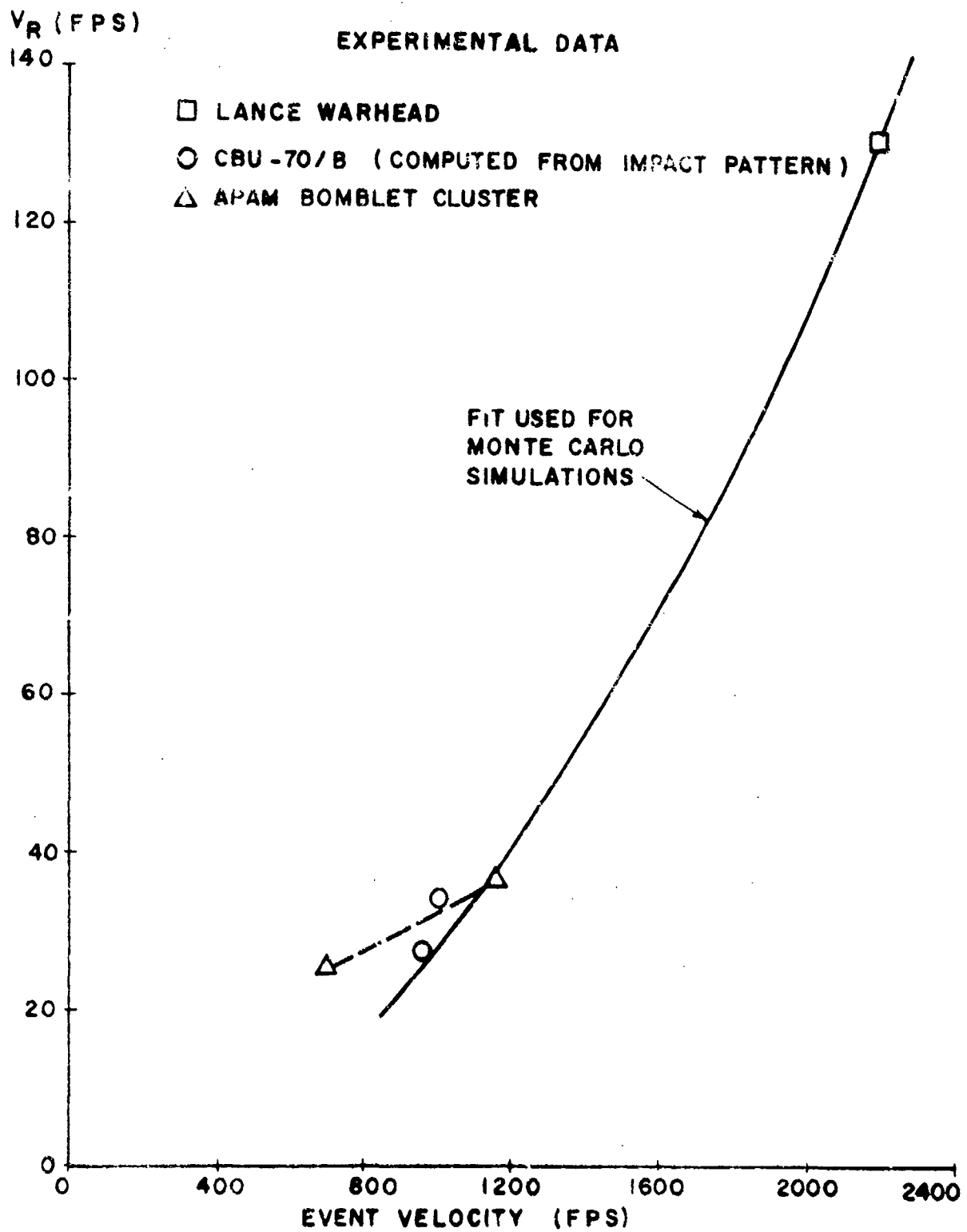


Figure 36. Experimental Data for Bomblet-Cluster Spread Velocity

fin cant statistics must be in a form compatible with the Monte Carlo trajectory program, which means that the statistical variation of the total fin roll torque is required. The total torque, in turn, is assumed to be proportional to an equal deflection of all the fins, and this deflection is defined as the effective fin cant.

By the method of super position, the total rolling moment due to separate deflection of n fins can be expressed as

$$C_{l_T} = C_{l_{TOTAL}} = \frac{C_{l_\delta}}{n} \sum_{i=1}^{i=n} \delta_i = C_{l_\delta} \delta_e \quad (8)$$

where C_{l_δ} is the effective roll torque coefficient due to fin cant, corresponding to simultaneous deflection of all n fins and δ_e is the effective fin cant deflection. Letting the variance of angular deflection of each fin equal σ_F^2 , then the standard deviation of C_{l_T} is

$$\text{std dev } C_{l_T} = \frac{C_{l_\delta}}{n} \left[\sum_{i=1}^{i=n} \sigma_{F_i}^2 \right]^{1/2} \quad (9)$$

If the variance of all fins is identical,

$$\text{std dev } C_{l_T} = \frac{C_{l_\delta}}{n} \left[n \sigma_F^2 \right]^{1/2} = \frac{C_{l_\delta} \sigma_F}{n} = C_{l_\delta} (\delta_e)_\sigma \quad (10)$$

$$\text{or } (\delta_e)_\sigma = \sigma_F / \sqrt{n}$$

Thus, the effective fin cant angular error is neither the standard deviation of error for a single fin nor an average of the fin cant deviations of several fins, but rather the standard deviation of one fin divided by the square root of the total number of fins.

To obtain representative values for σ_F , fin cant misalignment data for 81mm mortar shells, 2.75-inch FFAR rockets, Rockeye bomblets, and Australian S-Curve test bomblets were obtained from References 24⁸, 25, and 26. Single fin misalignments for these configurations have been

⁸ The data of Reference 24 show that fin misalignments closely follow a normal distribution.

determined to be, respectively, 0.22 degree, 0.24 to 0.29 degree, 0.2 degree, and 0.08 to 0.2 degree. When a range of values is indicated, more than one type of configuration was inspected. On the basis of these results, a single fin alignment accuracy of 0.2 degree appears to be very reasonable for Monte Carlo simulations.

For a six fin S-Curve or roll-through-zero configuration the effective fin cant misalignment is 0.0816 degree.

Lateral Misalignment Lateral misalignment results primarily from two sources, (1) the angular accuracy of the fins with respect to the body at their point of attachment, and (2) the alignment of the fin assembly with the remainder of the body. These two types of misalignment tend to be statistically independent. Lateral misalignment results in transverse body-fixed forces and moments, in contrast to fin cant, which results in pure roll torque. If we define the angle δ as the average misalignment of a planar pair of fins, it is easily shown that the standard deviation of effective δ for the pair of fins is⁹

$$\text{std dev } (\delta)_{\text{eff}} = \frac{\sigma_F}{\sqrt{2}}, \text{ planar pair} \quad (11)$$

For multiple fins the forces generated by $(\delta)_{\text{eff}}$ are not colinear, and thus the effective δ must be based on the random deflection of several pairs of fins.¹⁰ This is similar to the random walk problem and leads to

$$\text{std dev } [(\delta)_{\text{eff}}]_{m \text{ pairs}} = \sqrt{\frac{m}{2}} \sigma_F, \text{ } m \text{ pairs} \quad (12)$$

The total lateral misalignment is the RSS of $(\delta)_{\text{eff}}$ and the fin assembly-body misalignment, ϵ ,

$$\text{std dev } (\delta_{\text{TOTAL}}) = \left[(\text{std dev } \delta_{\text{eff}})^2 + (\text{std dev } \epsilon)^2 \right]^{1/2} \quad (13)$$

The plane of the lateral misalignment can obviously have any orientation and is thus uniformly random.

⁹ The definition of δ for lateral misalignment is consistent with the evaluation of C_{N_δ} for a planar pair of fins.

¹⁰ Fin-fin interference effects are neglected here.

To obtain numerical values for the effective lateral misalignment only the misalignment ϵ need be considered since it has previously been shown that a good estimate for σ_F is 0.2 degree. On the basis of data from References 25 and 26 a reasonable value for ϵ is also 0.2 degree. Thus the standard deviation of total lateral misalignment is estimated to be 0.32 degree for S-Curve and roll-through-zero bomblets with six fins.

Static and Dynamic Unbalance The static unbalance of bombs, rockets, and projectiles depends greatly upon their design, manufacturing and loading. Static and dynamic balance data for ordnance are extremely limited and available for only a few configurations. A very comprehensive statistical analysis of the M437, 175mm projectile is presented in Reference 27. This, together with some unpublished data on mortar shells, was the extent of the available data. For artillery projectiles the standard deviation of static unbalance is of the order $\Delta y/d = 0.0004$, and the dynamic unbalance (inclination of principal axis) is of the order of 0.001 degree. In contrast, the standard deviation of static unbalance of mortar shells is reported to be as large as $\Delta y/d = 0.0050$.

Because of apparent large variations in static unbalance between various types of ordnance, a single value for the standard deviation of Δy , applicable to all S-Curve and roll-through-zero bomblets, was not considered appropriate. Consequently, in the Monte Carlo simulations the static unbalance parameter is varied parametrically from zero to as much as 0.04 inches.

SECTION V

DEVELOPMENT OF DYNAMIC WIND TUNNEL MODEL SUPPORT SYSTEM

A. SYSTEM DESCRIPTION

The dynamic wind tunnel model system provides for testing of quasi-axisymmetric model configurations under simulated coning motion conditions at constant angle of attack, either in steady or variable coning rate modes. Simultaneously, the model can be free to roll about its longitudinal axis or locked-in at a specific roll orientation. The system does not employ a force balance; instead, the aerodynamic moments are derived from analysis of the coning and rolling angular rate data.

Design details of the dynamic model support system are presented in Figures 37 and 38. The principal structural member is the rotating sting, which is supported by low friction bearings. The offset portion of the sting can be laterally adjusted by means of a boring head adapter. Provision is also made for attachment of static and dynamic balance weights to the shaft at two stations. The sting is connected to a Gast type-4 AM air motor with an output of 0.8 HP at 1000 rpm with 100 psi supply pressure. The sting and air motor are connected through an electric clutch, which provides for complete decoupling of the air motor when free rotation of the sting is required. The clutch and air motor can also be used for braking and stopping the sting rotation.

The model is attached to the sting through a second bearing assembly which allows the model to rotate freely with respect to the sting (Figure 38). Alternately, provision is made for locking the model at fixed orientations with respect to the sting. When locked to the sting the model undergoes forced lunar motion.

The test system incorporates a series of stings to permit testing at different angles of attack. At present, 15-, 30-, and 45-degree stings are available. For calibration purposes, a special zero-offset sting is provided. The zero-offset sting contributes negligible aerodynamic damping, but does not allow the model to roll about its own axis. A precision angular rate recording device is provided to measure the sting rotational rate. Model roll behavior must be recorded optically at present.

A photograph of the test system installed in the Air Force Armament Laboratory subsonic wind tunnel is shown in Figure 39. In the photograph the special calibration sting is installed.

- Legend:
- 1 Airmotor
 - 2 Magnetic Clutch
 - 3 Timing Disk
 - 4 Balance Weights
 - 5 Boring Head Adapter
 - 6 Rotating Sting

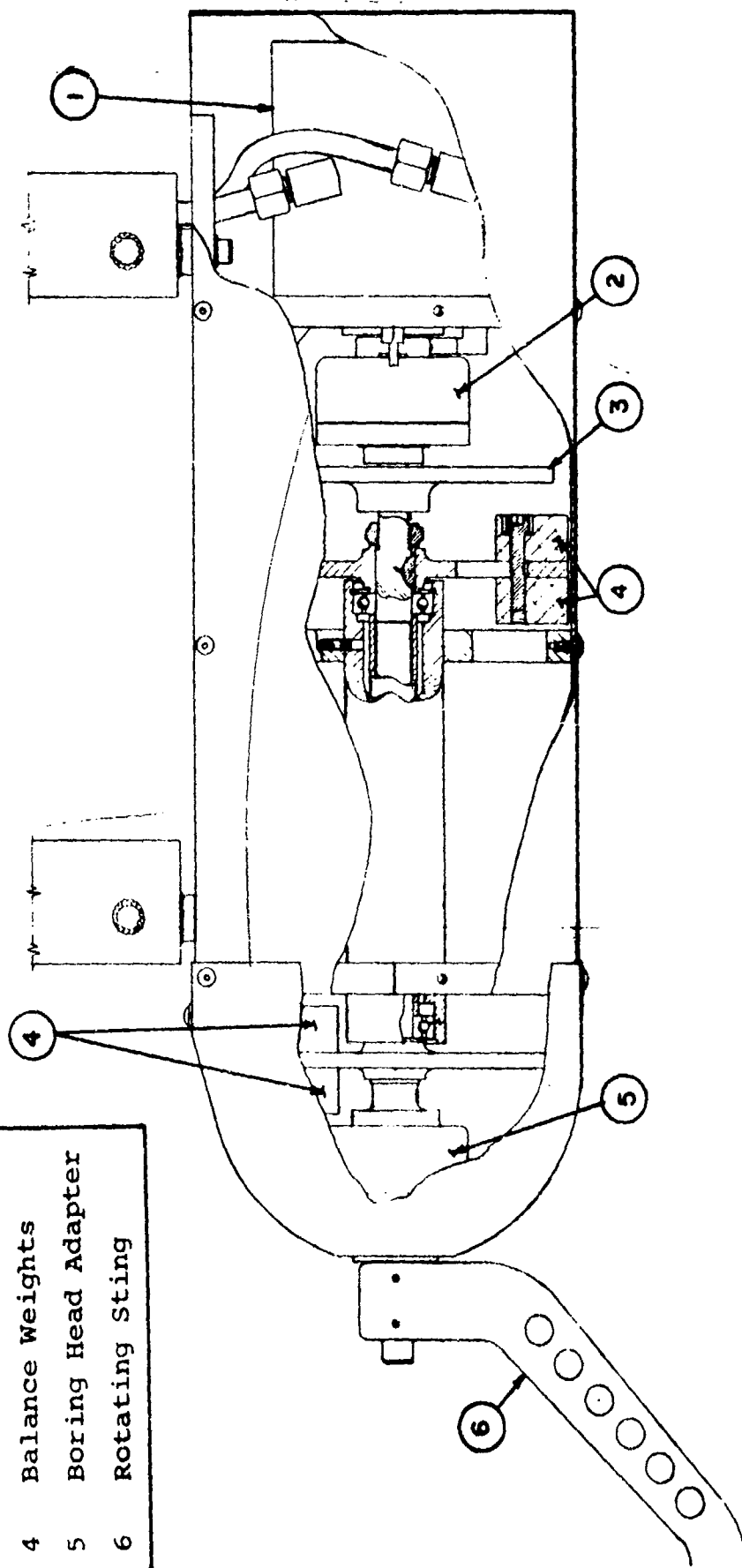


Figure 37. Dynamic-Wind-Tunnel-Model Support System -
Design of Rotating Sting

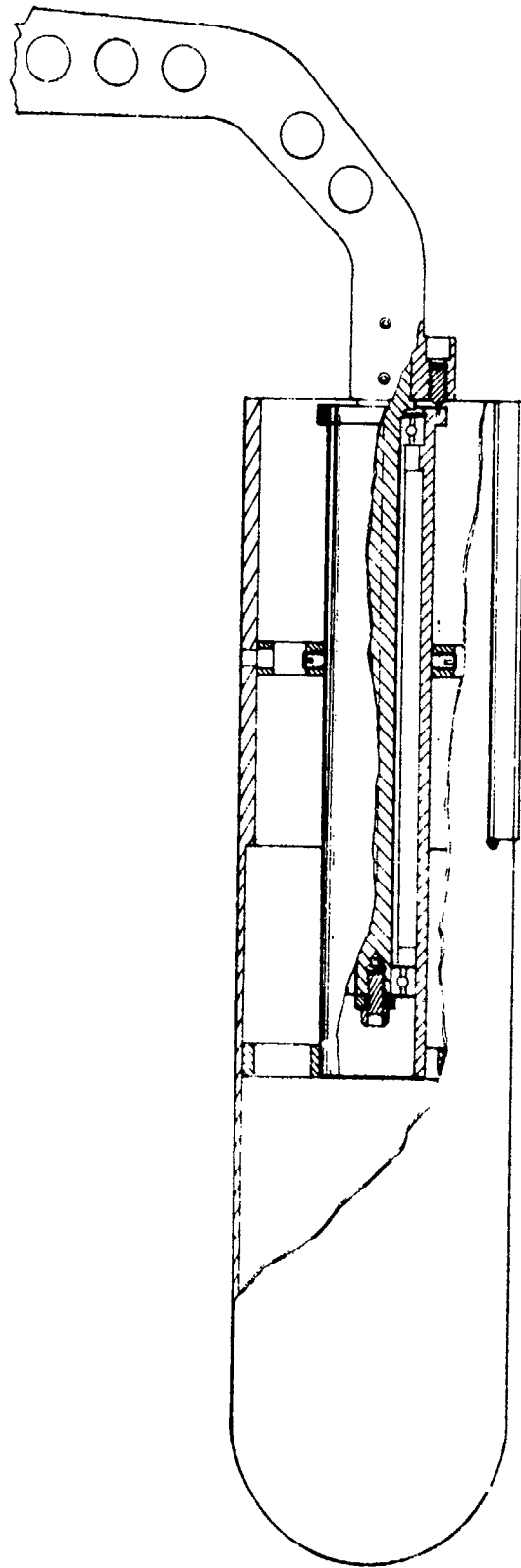


Figure 38. Dynamic-Wind-Tunnel-Model Support System -
Design of Model-Sting Attachment



Figure 39. Dynamic Wind Tunnel Model Support System

B. SYSTEM OPERATION

The test system has two basic modes of operation. In the first mode, the model is driven by the air motor to a pre-determined coning rate, and then disengaged such that the subsequent motion can be recorded. Normally, this will be a deceleration mode. The second mode of operation does not require the drive motor, and the coning is initiated by the inherent autorotational tendencies of the model. The autorotation can be produced by the magnus moment resulting from model axial spin (model spin achieved by fin cant) or by the aerodynamic side moment. Aerodynamic side moments can be produced by asymmetric roll orientation with respect to the angle of attack plane, or by other aerodynamic asymmetries.

To preclude autorotational moments from model-sting misalignment, the boring head is adjusted so that the sting rotational axis and the model axis of symmetry intersect to the required accuracy.

C. SYSTEM UTILIZATION

The primary purpose of the test system is the measurement of the model damping for circular-type motions. In accordance with the theory of Reference 28, it can be anticipated that the damping coefficient for coning motion will differ from that for planar pitching motion at finite angles of attack. To date, few definitive experiments have been conducted to determine the difference between the circular and planar motion damping coefficients, and no data have been published for subsonic conditions. The circular motion damping is of particular interest with respect to the S-Curve type bomblet, since this configuration experiences almost pure coning motion in free-flight.

The test system can be utilized to measure magnus and side moments, both from the transient and steady-state autorotational coning motions.

Both static and dynamic roll lock-in tests can be accomplished. Static roll lock-in tests are accomplished with model locked to the sting at specific roll orientations, and at those orientations the coning and side moment characteristics are determined. Dynamic roll lock-in tests are accomplished for those models which have inherent aerodynamic roll lock-in due to body-fin interference effects. The tendency for the lock-in to be stable under a wide range of coning rates and fin cant angles can be investigated.

The test system also provides an expedient means for determining model roll speed-up and roll slow-down at large angles of attack and the effect of coning motion on this type of dynamic behavior.

Procedure for Determination of Model Circular Motion Damping

The circular motion damping is determined from time histories of the coning rate decay, in a manner analogous to the determination of the roll damping coefficient in single degree-of-freedom spin decay experiments. Two separate tares may be required; one for the sting bearing friction torque, and a second for the offset sting. This latter tare is determined by the use of the calibration sting. The second tare is not required if the model is to always be in lunar circular motion, but in general, the circular motion damping should be determined for various model roll rates, which requires the offset sting.

Using the nomenclature shown in the test schematic, Figure 40, the equations of motion for each model-sting assembly can be expressed as:

$$I_x \dot{\Omega} - T_{\Omega} \Omega - T_O = 0 \quad (14)$$

where

$$T_{\Omega} = (T_{\Omega})_a + (T_{\Omega})_v$$

$$T_O = (T_O)_a + (T_O)_v$$

and subscript a) denotes aerodynamic torque on model
v) denotes viscous (or bearing) torque.

The quantity I_x is the total moment of inertia of the model and rotating sting assembly, taken about the axis of sting rotation.

The solution of equation (14), assuming constant coefficient is:

$$\Omega = -\frac{T_O}{T_{\Omega}} + \left(\Omega_0 + \frac{T_O}{T_{\Omega}} \right) \exp \left[\frac{T_{\Omega}}{I_x} (t - t_0) \right] \quad (15)$$

To obtain the aerodynamic torques, the system is first operated with the model and offset-sting section removed such that $(T_{\Omega})_v$ and $(T_O)_v$ can be evaluated. Then the complete model-sting system is operated and (T_{Ω}) and (T_O) are obtained, from which $(T_{\Omega})_a$ and $(T_O)_a$ are readily determined. To obtain T_{Ω} and T_O from equation (15), a least-squares differential-correction fitting technique is employed, as described in Reference 29. The possible nonlinear dependence of T_{Ω} upon Ω can be ascertained by piecewise fitting the Ω history.

When the model is operated with the offset sting, the torques $(T_{\Omega})_a$ and $(T_O)_a$ include a small but significant contribution from the sting. By replacing the offset sting with the calibration sting (which has negligible aerodynamic torque) the aerodynamic torque contribution of the offset sting is readily determined. Subtracting the offset sting torque from $(T_{\Omega})_a$ and $(T_O)_a$ we obtain $(T_{\Omega})_{a, \text{MODEL}}$ and $(T_O)_{a, \text{MODEL}}$.

FOR LUNAR MOTION

$$p = \Omega \cos \alpha$$

$$r = \Omega \sin \alpha$$

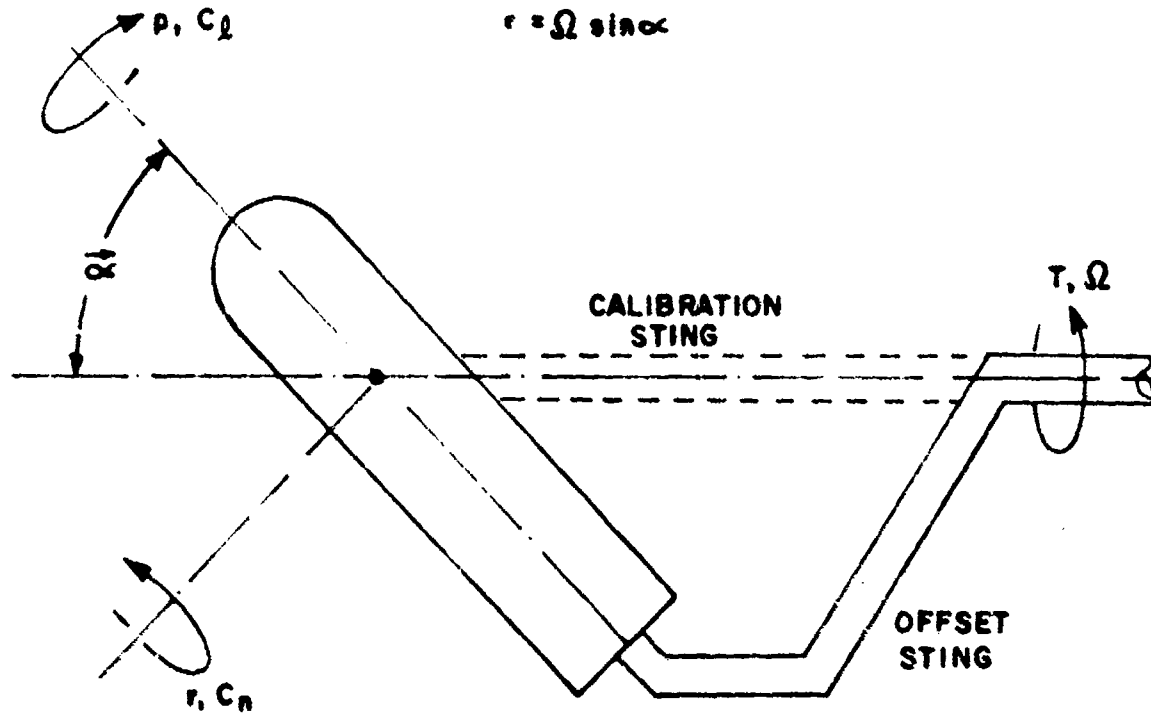


Figure 40. Schematic of Dynamic-Wind-Tunnel-Model Support System - Axes and Angular Rate Definitions

The aerodynamic torques $(T_{\Omega})_{a, \text{MODEL}}$ and $(T_o)_{a, \text{MODEL}}$ are equated to the model spin damping and yaw damping coefficients by the following relationships:

for lunar motion (model not free to roll)

$$\frac{(T_{\Omega})_{a, \text{MODEL}}}{1/2 \rho v^2 S d} = C_{n_r} \Omega \sin^2 \alpha + C_{\ell_p} \Omega \cos^2 \alpha \quad (16a)$$

$$\frac{(T_o)_{a, \text{MODEL}}}{1/2 \rho v^2 S d} = C_{n_o} \sin \alpha + C_{\ell_o} \cos \alpha \quad (16b)$$

for model free to roll

$$\frac{(T_{\Omega})_{a, \text{MODEL}}}{1/2 \rho v^2 S d} = C_{n_r} \Omega \sin^2 \alpha \quad (16c)$$

$$\frac{(T_o)_{a, \text{MODEL}}}{1/2 \rho v^2 S d} = C_{n_o} \quad (16d)$$

The coefficients C_{ℓ_o} and C_{n_o} are due only to asymmetries in the model and flow and should be quite small. The Coefficient C_{ℓ_p} will usually be evaluated from separate tests and is generally small compared to C_{n_r} . Present estimates at $\alpha = 15$ degrees give $C_{n_r} = -25.0$ and $C_{\ell_p} = -0.4$.

By use of equations (16a) or (16c) C_{n_r} can be evaluated for various values of angle of attack and Ω . These data can then be used to determine possible nonlinearities with respect to either variable.

APPENDIX I

THEORETICAL CONING MOTION ANALYSIS WITH ROLL DEPENDENT SIDE MOMENT

The fundamental equations describing the coning motion of S-Curve type bomblets are developed in Appendix II of Reference 1. Considered here is the effect of a roll dependent side moment on the stability of a zero coning solution.

The basic equations of coning motion for the S-Curve bomblet, as originally written, do not include the effect of the aerodynamic roll angle, ϕ . Furthermore, the non-rotating axes system which is utilized does not readily permit the inclusion of body-fixed aerodynamic moments. However, for the special case of zero spin, the effect of the rotation of the angle of attack plane (variable $\tilde{\phi}$) and the aerodynamic roll angle (ϕ) are related simply by

$$\tilde{\phi} = -\phi \quad (1-1)$$

The special coning solution may now be written, using the notation of Reference 1, as

$$I \alpha_T \ddot{\tilde{\phi}} = \left[\frac{I g \alpha_T \sin \gamma}{V} - \frac{I C_N \rho S V}{2m} + \frac{C_{n_r} \rho S d^2 V \alpha_T}{4} \right] \tilde{\phi} \quad (1-2)$$

$$\frac{C_{n_r} g \rho S d^2 \cos \gamma \sin \tilde{\phi}}{4} - \frac{C_{SM}(\tilde{\phi}) \rho V^2 S d}{2} = 0$$

Inspection of the order of magnitude of the last two terms reveals that for a six-fin bomblet a steady-state solution of equation (1-2) with $\ddot{\tilde{\phi}} = 0$ requires that $\tilde{\phi} = 0, \pm/6, \pm/3, \dots$ such that $C_{SM}(\tilde{\phi})$ is small. Figure 1-1 illustrates a typical variation of C_{SM} with $\tilde{\phi}$ for the basic S-Curve configurations. If the zero coning solution corresponds to $\tilde{\phi} > 0$ and $C_{n_r} < 0$, then $C_{SM}(\tilde{\phi})$ must be positive and vice versa.

To determine which, if any, of the steady-state zero coning solutions are stable solutions, the nature of the characteristic differential equation for the small perturbation $\delta \tilde{\phi}$ is examined. This requires that the term containing $C_{SM}(\tilde{\phi})$ be made a function of $\delta \tilde{\phi}$. This can be accomplished by considering the slope of C_{SM} versus $\tilde{\phi}$. Thus, equation (1-2) can be re-written

PRECEDING PAGE BLANK-NOT FILMED

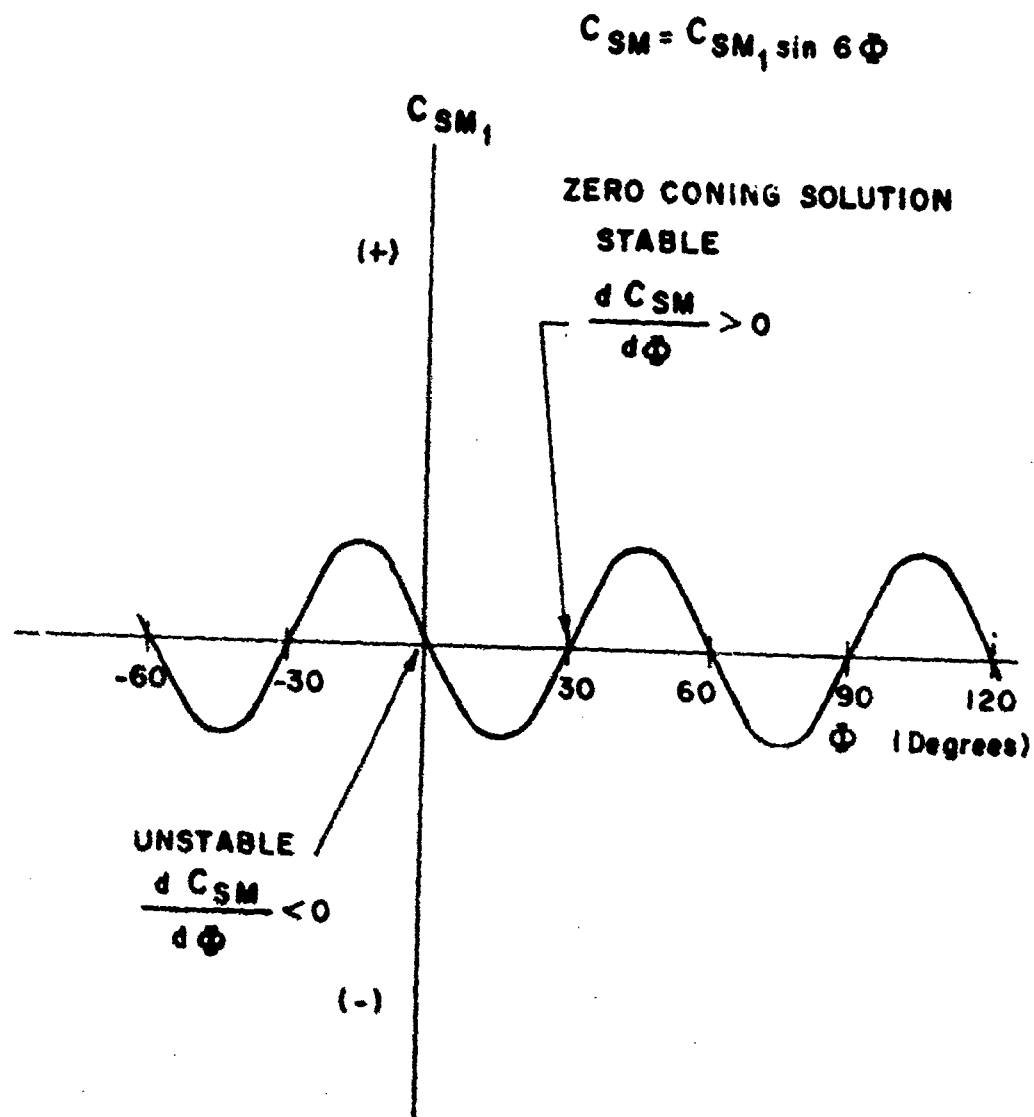


Figure 1-1. Variation of Side Moment Coefficient with Φ for Basic S-Curve Bomblet Configuration.

$$I_{a_T} \ddot{\Delta\phi} - \{ \} \dot{\Delta\phi} - \frac{C_{n_r} g \rho S d^2 \cos \gamma}{4} (\sin \bar{\phi}_0 + \Delta\phi) + \frac{d C_{SM}}{d \phi} \frac{1}{2} \rho V^2 S d \Delta\phi = 0 \quad (I-3)$$

For a stable solution, one of the requirements is that the coefficient of $\Delta\phi$ be positive. Again, inspecting the order of magnitude of the two terms which represent the coefficients of $\Delta\phi$, it is found that the $d C_{SM}/d \phi$ term is much larger than the term containing C_{n_r} . Therefore, a stable motion occurs only where $d C_{SM}/d \phi$ has a positive slope. Referring to the plot of C_{SM} versus ϕ it is clear that $\phi = 0$ is an unstable condition, and that the bomblet must roll approximately $\phi = \pm 30$ degrees to where C_{SM} is small and has a positive slope.

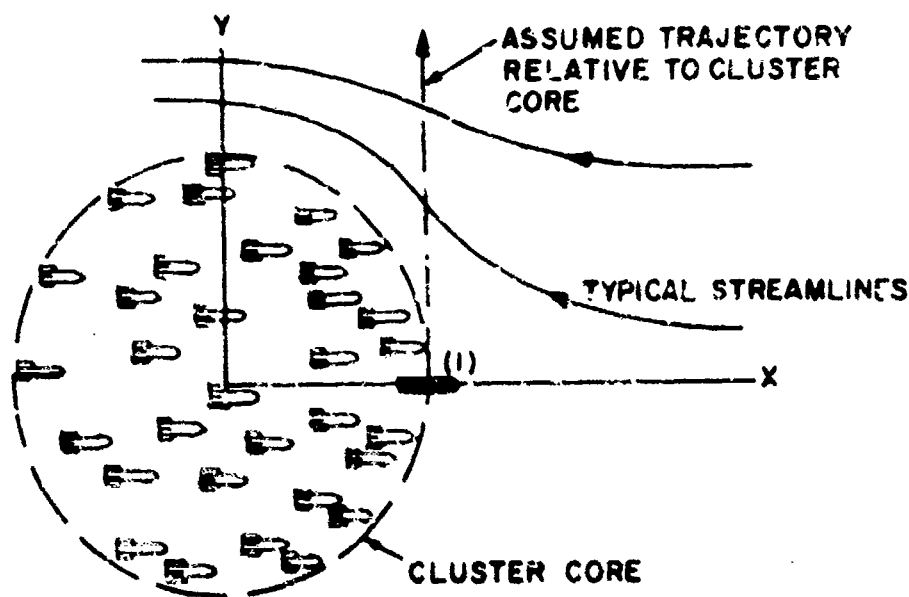
The corollary to the above is that a change in sign of the side moment coefficient, C_{SM1} , should make the bomblet motion stable at $\phi = \phi = 0$. This stability hypothesis has been confirmed by actual 6-DOF motion simulations with the sign of the side moment coefficient, C_{SM1} , purposely changed.

APPENDIX II

THEORETICAL PREDICTION OF CLUSTER SPREAD VELOCITY

A theoretical estimate of the maximum cluster spread velocity is made, by considering the motion of a single bomblet initially at the leading edge of the cluster. The forces acting on the bomblet are computed from the potential flow about a solid body assumed to represent the core of the cluster. This model is predicated upon observation of actual bomblet clusters, where it appears that the spreading is taking place primarily at the leading edge of the cluster.

As a first approach at a solution, consider a core of spherical shape with a diameter closely related to that of the dispenser. The physical model of the problem is like that sketched below.

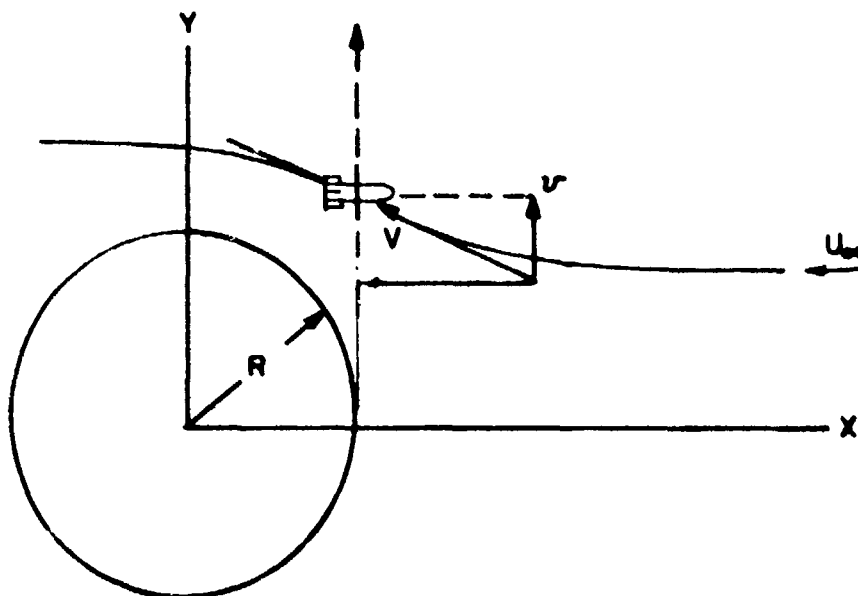


The aerodynamic forces acting on the bomblet (1) along the indicated lateral trajectory can now be evaluated, starting from an initial point slightly offset from the dividing streamline and extending laterally until near uniform flow is encountered. The selection of this particular trajectory is equivalent to the assumption that the bomblet and the cluster have the same deceleration.

The computation of the flow direction and magnitude at each point along this trajectory is easily accomplished using a known potential flow solution. (for example, pp 39, "Aerodynamics of Wings and Bodies, Ashley and Landahl, Addison-Wesley Press).

Since the direction and magnitude of the flow at each point along the radial trajectory is known, the aerodynamic lateral force can also be computed at each point. To begin, consider only the bomblet drag force, and its component in the lateral direction, F_y . The force, F_y , when integrated as a function of the radial deflection, represents the work done on the bomblet, and it can be equated to the radial kinetic energy of the bomblet. This in turn can be evaluated in terms of the radial velocity.

Defining the parameters in accordance with the sketch below, the radial velocity can be derived as follows:



The work done by the drag force can be expressed as

$$\text{Work} = \int_0^Y F_y dY \quad (11-1)$$

which can be re-written as

$$\text{Work} = \int_0^Y \left(\frac{\rho}{2} C_D S v^2 \left(\frac{v}{V} \right) \right) dY$$

Introducing the new variable Y/R , and relating the velocities to U_∞

$$\text{Work} = \frac{\rho}{2} C_D S U_\infty^2 R \int_0^{Y/R} \left[\frac{vV}{U_\infty^2} \right] d \left[\frac{Y}{R} \right] \quad (11-2)$$

Using the potential flow solution for a sphere at $X/R = 1.0$, the quantity $\frac{vV}{U_\infty^2}$ has been evaluated and is plotted in Figure II-1 as a function of Y/R . It is seen that most of the work done on the bomblet occurs with $Y/R < 3.0$. A very good approximation of the total work is achieved by integrating to $Y/R = 5.0$.

By equating the work done on the bomblet to its radial kinetic energy, a relationship for the radial velocity is obtained in the form

$$\frac{1}{2} m_B V_R^2 = (\rho/2) C_D S U_\infty^2 R \int_0^{Y/R} \left[\frac{vV}{U_\infty^2} \right] d \left[\frac{Y}{R} \right] \quad (\text{II-3})$$

$$\text{or } \frac{V_R}{U_\infty} = \left(\frac{g \rho R}{(W/C_D S)_B} \int_0^{Y/R} \left[\frac{vV}{U_\infty} \right]^2 d \left[\frac{Y}{R} \right] \right)^{\frac{1}{2}}$$

The integral can be evaluated from Figure II-1 and has a value of approximately 0.39. Therefore approximately

$$\frac{V_R}{U_\infty} \approx \left[0.39 \frac{g \rho R}{(W/C_D S)_B} \right]^{1/2} \quad (\text{II-4})$$

where

R Cluster core radius

$(W/C_D S)_B$ bomblet ballistic coefficient.

Thus, the radial velocity imparted to a bomblet displaced from the leading edge of the cluster is

- 1) Directly proportional to the cluster (event) velocity.
- 2) Proportional to the square-root of the cluster size.
- 3) Inversely proportional to the square-root of the bomblet ballistic coefficient.

Equation (II-4) was evaluated for both CBU-70/B and APAM clusters, assuming that R was the same as the dispenser radius. For the CBU-70/B the radial velocity is determined to be

$$V_R = 0.018 U_\infty$$

and for APAM

$$V_R = 0.013 U_\infty$$

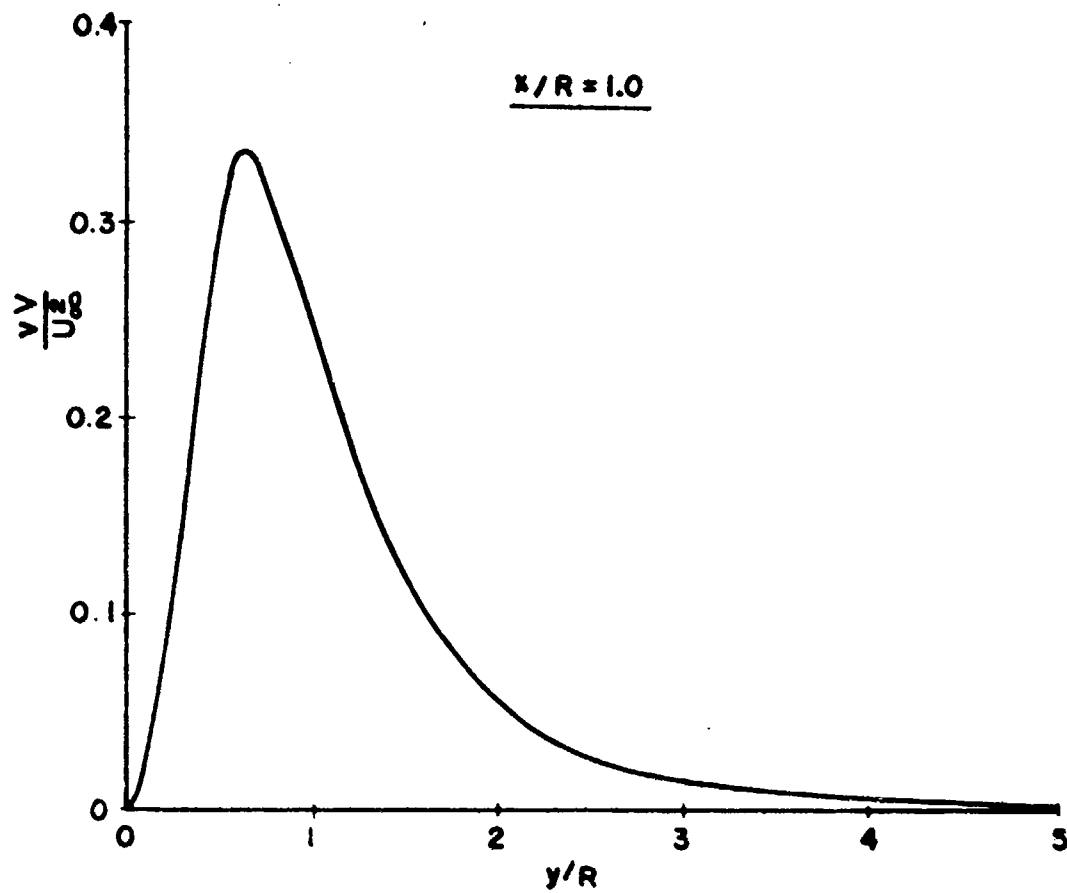


Figure II-1. Lateral Force Parameter for Bomblet Separating from Cluster

Test data (Figure 33) indicate a value of $V_R/U_\infty = 0.03$ at $U_\infty = 900$ feet/second. Thus the method appears to give a correct order of magnitude prediction, although the predicted radial velocity is somewhat low. This may be due to selecting R as the dispenser radius; possibly the cluster can expand to larger size and still behave as a quasi-solid core.

The above theory confirms the findings of Reference 19 that the spread velocity is a linear function of the event velocity. The theoretical dependence of the radial velocity on the bomblet ballistic coefficient is a new result. It will be of future interest to see if this can be confirmed by test data.

REFERENCES

1. Brunk, James E., Alpha Research, Inc., "Aerodynamic Dispersion Techniques," Air Force Armament Laboratory Report No. AFATL-TR-70-123, November 1970.
2. Brunk, James E., Alpha Research, Inc., "Flight Dynamics and Dispersion Characteristics of S-Curve and Roll-Through-Zero Bomblets," Air Force Armament Laboratory Report No. AFATL-TR-72-181, September 1972.
3. Brunk, James E., Alpha Research, Inc., "User's Manual: Extended Capability Magnus Rotor and Ballistic Body 6-DOF Trajectory Program," Air Force Armament Laboratory Report No. AFATL-TR-70-40, May 1970, AD 877 852.
4. Brunk, James E., Alpha Research, Inc., "Amended User's Manual: Extended Capability Magnus Rotor and Ballistic Body 6-DOF Trajectory Program," Report No. 71-2, 26 March 1971.
5. Shadow, T. O., "Wind Tunnel Investigation of the Transonic Static Stability Characteristics of Three Bomblet Munition Models Used in the Evaluation of Aerodynamic Dispersion Techniques," Arnold Engineering Development Center Report No. AEDC-TR-70-233, September 1970.
6. Schlegel, Capt. Mark O., "Wing Tunnel Tests of Modified BLU-87/B Fragmentation Bombs," Air Force Armament Laboratory Report No. AFATL-TR-72-132, July 1972.
7. Hayes, W. C., Jr. and W. P. Henderson, "Some Effects of Nose Bluntness and Fineness Ratio on the Static Longitudinal Aerodynamic Characteristics of Bodies of Revolution at Subsonic Speeds," NASA Report No. TN D-650, February 1961.
8. Anderson, C. F., "Static and Dynamic Stability Characteristics of Several Short Blunt Cylindrical Bomblet Models at Mach Numbers from 0.4 to 1.3," Arnold Engineering Development Center Report No. AEDC-TR-71-110, May 1971, AD 883 805L.
9. Uselton, Bob, Jack Carman and Tom Shadow, "Dynamic Stability Characteristics of Axisymmetric Bomblet Munition Models at Mach Numbers 0.3 Through 1.2," Arnold Engineering Development Center Report No. AEDC-TR-70-270, December 1970.

REFERENCES (Continued)

10. Carman, J. B., B. L. Uselton, and G. E. Burt, "Roll-Damping, Static Stability, and Damping-in-Pitch Characteristics of Axisymmetric Bomblet Munition Models at Supersonic Mach Numbers," Arnold Engineering Development Center Report No. AEDC-TR-71-88, April 1971, AD 882 636L.
11. Shadow, T. O., "Transonic Roll-Damping and Magnus Characteristics of Three Bomblet Munition Models Used in the Evaluation of Aerodynamic Dispersion Techniques," Arnold Engineering Development Center Report No. AEDC-TR-71-33, March 1971.
12. Shadow, T. O., "Transonic Static Stability Characteristics of Bomblet Munition Models Used in the Evaluation of the Zero-Coning Aerodynamic Dispersal Technique," Arnold Engineering Development Center Report No. AEDC-TR-71-247, November 1971.
13. Shadow, T. O. and G. R. Gomillion, "Transonic Aerodynamic Characteristics of Bomblet Munition Models Used in the Evaluation of the Roll-Through-Zero Aerodynamic Dispersion Technique," Arnold Engineering Development Center Report No. AEDC-TR-72-106, July 1972.
14. Fletcher, C. A. J., "Wind Tunnel Tests on An Axisymmetric, Lifting Bomblet with Body Mounted, Rectangular Fins," Australian Defence Scientific Service, Weapons Research Establishment, Salisbury, S. Australia, Report No. HSA 141, December 1968, AD 855 048.
15. Hunter, J. S., "Some Aspects of the Flight Dynamics of S-Curve Bomblets," Weapons Research Establishment, Salisbury, S. Australia. Paper presented at the Ninth Meeting of TCCP Panel 0-7, Defense Research Establishment, Valcartier, Canada.
16. Brunk, James E., "6-DOF Monte Carlo Trajectory Program," Alpha Research Report No. 72-9089-10, 29 September 1972.
17. Robinson, M. L., "Wind Tunnel Tests of the Static Aerodynamic Characteristics of Non-Slender Bomb Shapes at Subsonic Speeds," Weapons Research Establishment, Salisbury, S. Australia Technical Note HSA 184, September 1970, AD 863 951.

REFERENCES (Continued)

18. Gomillion, G. R., "Wind Tunnel Investigation of the Transonic Static Stability Characteristics of a Bluff Body Shape with Various After-body-Stabilizer Configurations," Arnold Engineering Development Center Report No. AEDC-TR-72-68, May 1972, AD 894 198.
19. Okauchi, K., "APAM Bomblet Aeroballistics Program," Naval Weapons Center Report No. NWC TP-5129, June 1971, AD 516 826L, (Confidential).
20. Pitts, William C., Jack N. Nielsen, and George E. Kaattari, "Lift and Center of Pressure of Wing-Body-Tail Combinations at Subsonic, Transonic, and Supersonic Speeds," NACA Report 1307, 1957.
21. DeJonge, Clark, "The Effect of Low Aspect Ratio Rectangular and Delta Cruciform Fins on the Stability of Bodies of Revolution with Tangent Ogives at Small Angles of Attack Through a Mach Number Range of 0 to 3.5," U. S. Army Ordnance Missile Command, Redstone Arsenal, Alabama, Report No. RF-TR-62-1, 23 May 1962.
22. Mengelson, Capt. William G., "Supplementary Ballistic Data Test of the CBU-70/B," Armament Development and Test Center Report No. ADTC-TR-71-152, December 1971, AD 891 295L.
23. Koff, Irwin, "Cluster Bomb MK20 Mod 2 (Rockeye II) Development, Test, and Evaluation," Naval Weapons Center Report No. NWC-TP-4798, December 1970, AD 516 688 (Confidential).
24. Kahn, Stanley D., "Blade Straightness Study of the M149 Fin for the 81 mm M374 Mortar Projectile," Picatinny Arsenal Technical Report 3758, December 1966.
25. Dolgonas, G. and Krayenbuhl, H. A., "2.75-In. Folding Fin Aircraft Rocket," Aerojet-General Corp. Report No. AFRDL-TR-69-90, Vol. II, Appendix A, April 1969, AD 501 433 (Confidential).
26. Hunter, J. S., "Flight Performance of Self-Dispersing Fin Stabilized Cylindrical Bomblets," Weapons Research Establishment, Salisbury, S. Australia, Technical Note HSA 151, May 1969, (Confidential).
27. Hudgins, Henry E., Jr., "The Statistical Properties and Correlations of Dimensional Variations and Inertial Properties of 175 MM, M437, Projectiles," Picatinny Arsenal, Dover, N. J. Technical Report No. 4309, March 1972.

REFERENCES (Concluded)

28. Tobak, Murray, Lewis B. Schiff and Victor Peterson.
"Aerodynamics of Bodies of Revolution in Nonplanar Motion."
AIAA Paper No. 68-20, AIAA 6th Aerospace Services Meeting,
January 22-24, 1968.
29. Brunk, James E. , "Aerodynamic Dispersion Techniques - Contract
Status Report No. 17 for Contract No. F08635-71-C-0089," July 1972.

INITIAL DISTRIBUTION

| | |
|-----------------------|----|
| AUL (AF L-LSE-70-239) | 1 |
| DDC | 2 |
| ASD (ENYS) | 1 |
| PACAF (1GY) | 1 |
| ALPHA RSCH, INC | 3 |
| CDCLO/ADTC/DO | 1 |
| DL | 1 |
| DLOSL | 2 |
| DLDL | 15 |

UNCLASSIFIED

Security Classification

DOCUMENT CONTROL DATA - R & D

(Security Classification of title, body of abstract and indexing annotation must be entered when the overall report is classified)

| | | | |
|--|---|---|--|
| 1. ORIGINATING ACTIVITY (Corporate author) Alpha Research, Inc. 55 Hitchcock Way, Suite 103 Santa Barbara, Calif. 93105 | | 2a. REPORT SECURITY CLASSIFICATION UNCLASSIFIED | |
| | | 2b. GROUP | |
| 3. REPORT TITLE MONTE CARLO ANALYSIS OF S-CURVE AND ROLL-THROUGH-ZERO BOMBLET DISPERSION CHARACTERISTICS | | | |
| 4. DESCRIPTIVE NOTES (Type of report and inclusive dates) Final Report - 4 February 1971 through 15 November 1972 | | | |
| 5. AUTHOR(S) (First name, middle initial, last name) James E. Brunk | | | |
| 6. REPORT DATE January 1973 | 7a. TOTAL NO. OF PAGES 109 | 7b. NO. OF REFS 29 | |
| 8a. CONTRACT OR GRANT NO. F08635-71-C-0089 | 9a. ORIGINATOR'S REPORT NUMBER(S) | | |
| 8b. PROJECT NO. 2547 | 9b. OTHER REPORT NO(S) (Any other numbers that may be assigned this report) AFATL-TR-73-15 | | |
| 10. DISTRIBUTION STATEMENT Distribution limited to U. S. Government agencies only; this report documents test and evaluation; distribution limitation applied January 1973. Other requests for this document must be referred to the Air Force Armament Laboratory (GPO), Eglin Air Force Base, Florida 32542. | | | |
| 11. SUPPLEMENTARY NOTES Available in DDC | | 12. SPONSORING MILITARY ACTIVITY Air Force Armament Laboratory Air Force Systems Command Eglin Air Force Base, Florida 32542 | |
| 13. ABSTRACT The flight dynamics and dispersion characteristics of candidate S-Curve and roll-through-zero bomblets are evaluated by use of the Monte Carlo method. Detailed analyses of bomblet-cluster breakup and bomblet configurational and aerodynamic asymmetries are used to establish the statistical input data required for the Monte Carlo analyses. Improved aerodynamic data packages for both the S-Curve and roll-through-zero bomblets are provided, and results of additional wind tunnel tests are discussed. Monte Carlo simulations show that for realistic flight environments both the S-Curve and roll-through-zero bomblets can achieve large and uniform impact patterns. For a representative dispenser HOB of 2000 feet, opening velocity of 900 fps, and 45 degrees flight path angle, impact pattern widths of 800 and 600 feet are computed for the S-Curve and roll-through-zero type bomblets, respectively. The effects of transonic and supersonic delivery, large static mass unbalance, nose-roughness asymmetry, and intentional fin cant on the S-Curve bomblet flight characteristics and dispersion are investigated in detail. Flight test dispersion data for the S-Curve bomblet, as obtained from air-gun launched models, is compared with results from analytical simulations. A dynamic wind tunnel model support system, designed for testing the S-Curve bomblet, is described. | | | |

Best Available Copy

UNCLASSIFIED

Security Classification

14

KEY WORDS

LINK A

LINK B

LINK C

ROLE

WT

ROLE

WT

ROLE

WT

S-Curve Bomblet

Roll-Through-Zero Bomblet

Monte Carlo Analysis

Impact Patterns

Flight Dynamics

Dispersion

Cluster Break-Up

Configurational and Aerodynamics

Asymmetries

Six-Degrees-of-Freedom Trajectory

Aerodynamic Characteristics

Aerodynamic Configurations

Bomblets

Cluster Dispensers

Cluster Warheads

Mathematical Models

UNCLASSIFIED

Security Classification